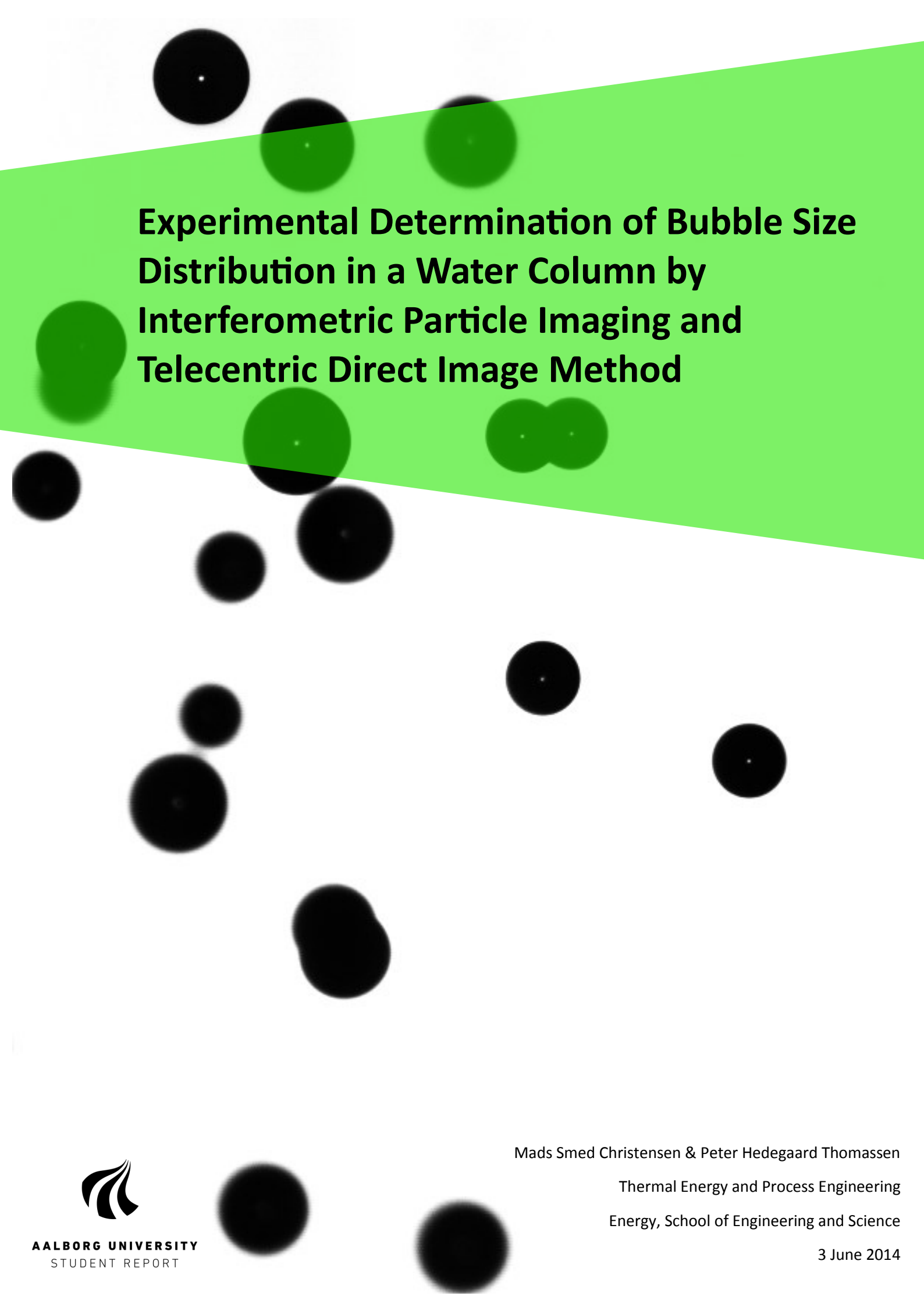

Experimental Determination of Bubble Size Distribution in a Water Column by Interferometric Particle Imaging and Telecentric Direct Image Method

Mads Smed Christensen & Peter Hedegaard Thomassen

Thermal Energy and Process Engineering

Energy, School of Engineering and Science

3 June 2014

AALBORG UNIVERSITY
STUDENT REPORT

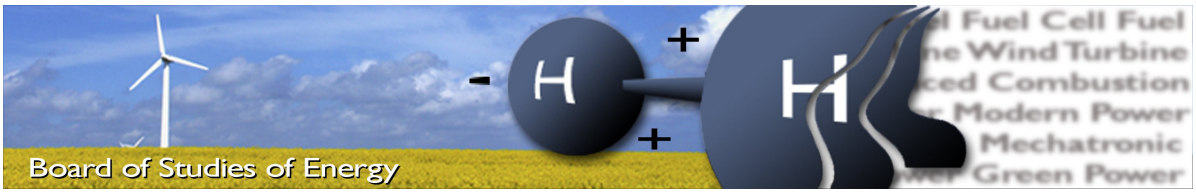

Title:	Experimental Determination of Bubble Size Distribution in a Water Column by Interferometric Particle Imaging and Telecentric Direct Image Method
Semester theme:	Master Thesis
Semester:	4^{th} M.Sc.
Project period:	03.02.14 to 03.06.14
ECTS:	30
Supervisor:	Henrik Sørensen
Project group:	TEPE4-1005

Mads Smed Christensen

Peter Hedegaard Thomassen

Synopsis:

The increasing application of computational modeling for two-phase flow analysis increases the demand for more accurate measurement techniques. An accurate in-line monitoring system is developed for estimating the size of rising bubbles in stagnant water. Telecentric Direct Image Method (TDIM) is applied as an inexpensive and easier implementing alternative to the complex and costly Interferometric Particle Imaging (IPI). A system from Dantec Dynamics is utilised for IPI measurements. It shows an unexpected bimodal bubble distribution for two bubble sizes with mean diameters of 189.31 μm and 669.34 μm, and a total mean diameter of 323.59 μm with a standard deviation of 230.5 μm. TDIM utilises the principle of shadow imaging, the advantage of telecentric optics and digital image processing. The mean diameter becomes 436.13 μm with a standard deviation of 78.36 μm. In this connection TDIM turns out more reliable than IPI, for which further measurements are necessary due to incorrect settings in the optical setup.

Copies:	4
Pages, total:	107
Appendices:	A-H
Supplements:	CD

By signing this document, each member of the group confirms that all participated in the project work and thereby all members are collectively liable for the content of the report.

Summary

Computational Fluid Dynamics is becoming more frequently applied for two-phase flow analysis, but are lacking when it comes to details of particle characteristics inside the flow. The limitations increases as the flows become highly dense and unsteady. It increases the demand for more accurate measurement techniques.

It is desired to develop an accurate monitoring system for estimating the size distribution of rising bubbles in stagnant water. Despite from being accurate the system must be affordable and easy to implement. Telecentric Direct Image Method (TDIM) is applied as an inexpensive and simple measurement technique. For verification Interferometric Particle Imaging (IPI) is applied as a highly accurate, but complex and costly method.

TDIM uses a white LED for background light and the advantage of telecentric optics. The images are pre-processed by background removal and by grey scale modification. Further digital image processing is performed in NI Vision, where Prewitt edge detection is found most feasible for edge detection of the bubbles. Therefrom a global threshold is chosen to sort out defocused bubbles. The mean diameter is 436.13 μm with a standard deviation of 78.36 μm which is consistent with the expected result.

IPI is performed by a system from Dantec Dynamics. It utilises a laser sheet which is scattered through the bubbles. The interference of the scattered light is analysed in the supplied software to determine the individual bubble diameters. The result is an unexpected bimodal bubble size distribution consisting of two distinct categories. One of many bubbles with a mean diameter of 189.31 μm and one of fewer bubbles with a mean of 669.34 μm. The total mean is 323.59 μm with a standard deviation of 230.5 μm.

The two methods are compared and validated. First of the measured regions are investigated, with the wider Region of Interest (ROI) for IPI and the narrower Field of View (FOV) for TDIM. Both turns out to cover the highest frequency range of generated bubbles with some bubbles missed out by FOV. TDIM is applied on round 50 μm polyamid particles. The mean becomes 58.5 μm with a standard deviation of 11.5 μm, which verifies its reliability. The associated feature of Particle Tracking Velocimetry is applied to verify the reliability of IPI. There is no tendency of two bubble size categories. The failed result of IPI is due to misleading information concerning the setup from the manual provided by Dantec Dynamics.

Further IPI measurements are necessary to be conducted with a new observation angle. Consequently, it should be possible to state the reliability of IPI in relation to TDIM. Despite, TDIM turns out to be a more reliable and more straightforward approach.

Preface

This report *Experimental Determination of Bubble Size Distribution in a Water Column by Interferometric Particle Imaging and Telecentric Direct Image Method* is a master thesis, written by Peter Hedegaard Thomassen and Mads Smed Christensen, 4^{th} semester M.Sc. students at the School of Engineering of Science at Aalborg University.

The project has been in cooperation with Tetra Pak Scanima A/S, who manufactures high-shear mixing solutions. The authors would like to thank the company and Hans Henrik Mortensen for being a source of inspiration and for the information which they gave us and for the time they spend. Additionally, a huge thanks to the supervisor Henrik Sørensen for great guidance.

Reading Instructions

All the references are listed in the end of the report. The Harvard Method is used for references, where the source will be written as [Author, Year] in the text. If the reference is placed before the full stop in a sentence, the reference is stated for only this sentence. If the reference is placed after the full stop, the reference is stated for the whole text piece.

Page numbers in the references are referred to as [p. 4] for a single page and [pp. 4-10] for a page interval.

Figures, tables and equations are numbered in accordance to the chapter number or appendix character. This means that the first figure in Appendix B is numbered B.1 and the next figure numbered B.2. The explanatory text to these will be attached to the given figure or table in a caption.

Nomenclature

Symbol	Description	Unit
a	Separation spacing	m
	Acceleration	m/s^2
A	Lens to the front of the water column	m
	Area	m^2
	Distance from camera to front of bubble column	m
B	Front to back side of the column	m
	Distance from front of bubble column to diffuser plate	m
C	Back side of water column to front of LED lamp	m
	Coefficient	-
	Distance from diffuser plate to halogen lamp	m
d	Diameter	m
D	Diameter	m
	Working Distance	m
	Distortion	%
E	Position of FOV and LED lamp	m
Eo	Eötvös number	-
f	f-stop number	-
F	Frequency	Hz
	Cannula from internal wall	m
	Force	N
FL	Focal length	m
g	Gravitational acceleration	m/s^2
G	Inner bottom to cannula opening	m
H	Heywood circularity factor	-
	Water column above cannula	m
I	Image	-
	Internal height of column	-
	Current	A
J	Internal width of column	m
K	Thickness of wall	m
L	Cannula from internal wall	m
m	Relative refractive index	-
Mo	Morton number	-
n	Number	-

Continued on next page

Continued from previous page

Symbol	Description	
	Refractive index	-
N	Number of fringes	-
p	Pressure	bar
	Parameter	-
P	Perimeter	m
	Power	J
q	Parameter	-
r	Percentage relation	%
	Radius	m
R	Electric resistance	Ω
Re	Reynolds number	-
S	Slite	-
$s.d.$	Standard deviation	m
T	Temperature	°C
t	Time	s
U	Velocity in x-direction	m/s
	Voltage	V
v	Velocity	m/s
V	Volume	m^3
	Velocity in y-direction	m/s
x	Direction, distance	m
X	Focal distance of laser	m
	x-direction in measurement volume	m
y	Direction	m
Y	y-direction in measurement volume	m
z	Direction, direction	m
	Standard deviation of the mean	-
Z	Distance to the particle from the receiving aperture	m
	z-direction in measurement volume	m

α	Angular aperture of the optic	°
	Area under normal curve	-
δ	Confidence interval	m
ϵ	Error	m
κ	Geometrical factor	m
λ	Wave length	m
	Viscosity ratio	-
μ	Dynamic viscosity	kg/m·s
	True mean value	m
ρ	Density	kg/m^3
σ	Fringes spacing	m

Continued on next page

Continued from previous page

Symbol	Description	
	Surface tension	N/m
θ	Angle	$^\circ$
ϕ	Scattering angle	$^\circ$
φ	Angular fringe	$^\circ$

Prescript

Δ	Difference

Subscript

a	Air
	Aperture
b	Bubble
	Big
B	Background
	Buoyancy
c	Continuous
	Critical
C	Contrast enhancement
d	Dispersed
D	Drag
F	Foreground
i	Incident
	Individual
l	Minimum standoff distance
m	Medium
max	Maximum
min	Minimum
N	Noise
O	Original
obs	Observation
p	Particle
$plexi$	Plexiglass
r	Reflecting
	Lens to camera sensor
s	Small
sca	Scattering
S	Stretched
t	Time
	Terminal
$threshold$	Threshold
x	x-direction

Continued on next page

Continued from previous page

Symbol	Description
y	y-direction
w	Water
W	Weight

Superscript	
$-$	Mean

Abbreviations	
CCD	Charged Coupled Device
CFD	Computational Fluid Dynamics
CMOS	Complementary Metal Oxide Semiconductor
DAQ	Data Acquisition
DIM	Direct Image Method
DLT	Direct Linear Transform
DOF	Depth Of Field
FFT	Fast Fourier Transform
FMPS	FlowMap Particle Sizer
FOV	Field Of View
fps	Frames per second
FP	Focal Plan
GS	Grey Scale
ILIDS	Interferometric Laser Imaging for Droplet Sizing
IMF	Imaging Model Fit
IPI	Interferometric Particle Imaging
LED	Light Emitting Diode
LMT	Lorenz-Mie Theory
LUT	Luminance Increment Threshold
MR	Magnification Rate
MSI	Mie Scattering Imaging
NI	National Instruments
PDA	Phase Doppler Anemometry
PIV	Particle Image Velocimetry
PTV	Particle Tracking Velocimetry
Q	Quality
ROI	Region Of Interest
TDIM	Telecentric Direct Image Method
WD	Working Distance
YAG	Yttrium Aluminium Garnet

Contents

Summary v

Chapter 1 Introduction 1
1.1 Relevance of Multiphase Flow Measurements . . . 1
1.2 Tetra Pak Scanima . . . 2
1.3 Previous Work . . . 2
1.4 Candidates for Measurement Method . . . 3
1.4.1 Phase Doppler Anemometry . . . 3
1.4.2 Interferometric Particle Imaging . . . 4
1.4.3 Shadow Sizing . . . 4
1.5 Improved DIM . . . 6
1.5.1 Camera . . . 6
1.5.2 Lens . . . 6
1.5.3 Light . . . 7
1.6 Verification Method . . . 7

Chapter 2 Problem Statement 9

Chapter 3 Interferometric Particle Imaging for Bubble Measurement 11
3.1 Introduction . . . 11
3.2 Bubble Diameter based on Light Scattering . . . 12
3.2.1 Working Principle . . . 12
3.2.2 Light Scattering . . . 13
3.2.3 Derivation of Optical Relation . . . 15
3.3 Settings of Optical Setup . . . 19
3.4 IPI Image Processing in FMPS . . . 21
3.4.1 Particle Detection . . . 22
3.4.2 Size Measurement - Camera B . . . 23
3.4.3 Validation . . . 23
3.4.4 Velocity Measurement - Camera A . . . 23
3.5 Results of IPI . . . 24
3.5.1 Data Selection and Processing . . . 24
3.5.2 Bubble Size . . . 25
3.5.3 Volume Size . . . 25

Chapter 4 Telecentric Direct Image Method for Bubble Measurement 27
4.1 Settings of Optical Setup . . . 27
4.2 Image Acquisition and Settings . . . 28

4.3 Digital Image Processing . . . 29
4.3.1 Image Components . . . 29
4.3.2 Image Pre-processing . . . 30
4.3.3 Image Processing . . . 34
4.4 Results . . . 38
4.4.1 Data Selection and Processing . . . 38
4.4.2 Bubble Size . . . 39
4.4.3 Volume Size . . . 41

Chapter 5 Comparison & Validation **43**
5.1 Comparison of IPI and TDIM results . . . 43
5.2 Investigation of ROI and FOV . . . 44
5.3 Validation of TDIM . . . 46
5.4 Validation of IPI . . . 48
5.4.1 Location of Bubble Groups . . . 48
5.4.2 Velocity Distribution . . . 49
5.4.3 Circularity of Bubbles . . . 51
5.5 Trouble Shooting with Dantec Dynamics . . . 51
5.6 Pros and Cons of IPI and TDIM . . . 52

Chapter 6 Conclusion **55**

Appendix A Vertical Bubble Flow **57**
A.1 Characteristics of Bubbles . . . 57
A.2 Regions and Hydrodynamic Forces of Rising Bubbles . . . 59
A.2.1 Dominated Regions . . . 59
A.2.2 Hydrodynamic Forces . . . 59
A.3 Reynolds Number Effects and Terminal Velocity . . . 60
A.3.1 Drag Coefficient of Viscous Spheres . . . 60
A.3.2 Terminal Velocity . . . 63

Appendix B Design & Test of Experimental Setup for Rising Bubbles **65**
B.1 Plexiglass Column . . . 65
B.2 Bubble Generation . . . 66
B.3 Pressure Measurement . . . 67
B.4 Test of Experimental Setup . . . 68
B.4.1 Calibration . . . 70
B.4.2 Image Processing . . . 71
B.4.3 Size Distribution . . . 71

Appendix C IPI Software Settings **73**
C.1 General . . . 73
C.2 Optical Setup . . . 74
C.2.1 Influence of Refraction . . . 74
C.2.1.1 Angle Calculation . . . 75
C.2.1.2 Distance Calculation . . . 76
C.3 Calibration . . . 77

C.4 Laser Setup . . . 77
C.5 Filter . . . 77
C.6 Window Setup . . . 78
C.7 ROI/Validation . . . 78
C.8 Velocity Setup . . . 79
C.9 Chosen Settings for FMPS . . . 80

Appendix D Calibration for IPI & TDIM **81**
D.1 Calibration in FlowMap Particle Sizer . . . 81
D.1.1 Contrast of Calibration Images . . . 81
D.1.2 Imaging Model Fit . . . 82
D.1.3 Dewarping Image . . . 83
D.2 Calibration in NI Vision Builder . . . 83

Appendix E Working Principles of Laser used for IPI **85**
E.1 Cavity . . . 85
E.2 Q-switch . . . 86
E.3 Double-cavity Laser . . . 86
E.4 Synchronisation . . . 87
E.5 Data for Nd:YAG Laser . . . 87
E.6 Light Sheet Thickness Adjustment . . . 89

Appendix F Required Sample Size for IPI & TDIM **91**
F.1 Sample Size Processing . . . 91
F.2 Required Sample Size for IPI . . . 92
F.2.1 Measurement Stability for IPI . . . 93
F.3 Required Sample Size for TDIM . . . 94
F.3.1 Measurement Stability for TDIM . . . 94

Appendix G TDIM Principles & Equipment **97**
G.1 Telecentricity . . . 97
G.2 Telecentric Lens . . . 98
G.3 Light . . . 100
G.4 Camera . . . 101

Appendix H CD Content **103**

Bibliography **105**

1 Introduction

The following will address to the considerations made before the project statement is specified. First of, the relevance of technical measurements of multiphase flow are considered. One company which finds that field very interesting is Tetra Pak Scanima, since several benefits can be acquired from such technical measurements, especially regarding estimation of air in food products. Prior experiences are included into the considerations for choosing relevant measurements methods.

1.1 Relevance of Multiphase Flow Measurements

Multiphase flows have become very important in fields such as energy, environmental, power and processing engineering. For two-phase flows it can be used in connection with combustion of pulverised coal particles or fuel droplets, spray drying and industrial emissions for pollutant control. Other fields also find usefulness for two-phase flow, such as agricultural spraying with focus on aerosol formation or the medicine industry regarding drug delivery through inhalers [Tayali and Bates, 1990]. Characterisation of the particle or gas phase inside a fluid is difficult since it is associated with high complexity and randomness. For that reason, the determination of multiple particle parameters through measurement techniques has become very desirable. [Chen et al., 2013]

Today Computational Fluid Dynamics (CFD) is used in a great extent within the field of multiphase flow analysis due to the enhancement of computational power and comprehensive models. It is beneficial when considering a steady and proper dispersed two-phase flow. However, when detailed information of particle characteristics such as size and velocity this is only partial available. Additionally, when dealing with an unsteady and highly dense flow many unsolved problems still occur. [Coghe and Cossali, 2011]

Consequently, the need has increased for comparing theoretical data with data acquired through experiments. The most desired variables in this context are the velocity, size and concentration for which several industries can benefit from knowing. [Tayali and Bates, 1990]

1.2 Tetra Pak Scanima

Tetra Pak Scanima produces high shear mixing machines such as the Tetra Almix batch vacuum mixer shown in Figure 1.1. Their mixers are utilised for many different purposes e.g. food processing. Considering this aspect, the goal is to completely mix all the ingredients while still keeping the air content at a low level. Additionally, there are certain standards for the present air bubbles with regards to the size distribution and total volume present in the final products. The air enters the batch mixer along with the sub products of powder consistency. In order to remove the air, vacuum is generated during the mixing process, making the bubbles rise to the surface for removal. Nevertheless, the final mixed product will still have present micro bubbles and additional larger bubbles if the mixing and vacuum generation are not performed properly.

Figure 1.1: Batch vacuum mixer from Tetra Pak Scanima. [Mortensen, 2013]

Tetra Pak Scanima has an interest in an in-line monitoring system which can perform a quantification of undissolved air inside a liquid product. It will increase product quality by making sure the air content is low in the final product, where a high content will decrease shelf life due to a high concentration of oxygen. The interest is assisted by other advantages from such a system. By a continuous analysis of the bubbles, warnings of potential incipient faults on the batch mixer can be given. It concerns leakages which can be detected by any inconsistency with prior sample statistics of bubble parameters. Regarding energy consumption then the mixing process can be brought to rest as soon the air content satisfies the given standards.

1.3 Previous Work

The project is in cooperation with Tetra Pak Scanima and is a continuation of the study described in the paper *Bubble Detection using Digital Image Processing*. The objective of that study was to achieve images of highlighted bubbles usable for size determination by digital image processing. The images are taken of a gel containing static bubbles for which different types of light settings are tested and the images treated through digital image processing. Various techniques are used for calculating the bubble volume which is prolate

ellipsoidal and not spherical in shape. Additionally, an edge detection tool is developed using fuzzy divergence as an alternative to Prewitt edge detection. It turns out that fuzzy edge detection highlights the details of the edges to a greater extent than Prewitt edge detection. The work is desired to be applied on an experimental setup with a continuous dispersed flow of bubbles with a characteristic spherical shape to perform the analysis of a bubble size distribution. To verify its reliability a comparison is necessary in relation to an already accepted measurement method. [Christensen and Thomassen, 2013]

1.4 Candidates for Measurement Method

Depending on which parameter is desirable either the velocity, size or concentration, different kinds of measurements methods can be utilised. In the case of an in-line monitoring system for bubble analysis all three parameters will be desirable. In the following, different measurement systems are outlined where considerations are made for which of those will be the most feasible for estimating the bubble size distribution. Since bubbles are the dispersed phase in the flow, the considered methods must be able measure particle characteristics on transparent particles.

1.4.1 Phase Doppler Anemometry

Phase Doppler Anemometry (PDA) measures all three parameters for spherical particles such as droplets and bubbles, which are dispersed in a gaseous or liquid flow. The working principle is shown in Figure 1.2 and is based on light scattering interferometry.

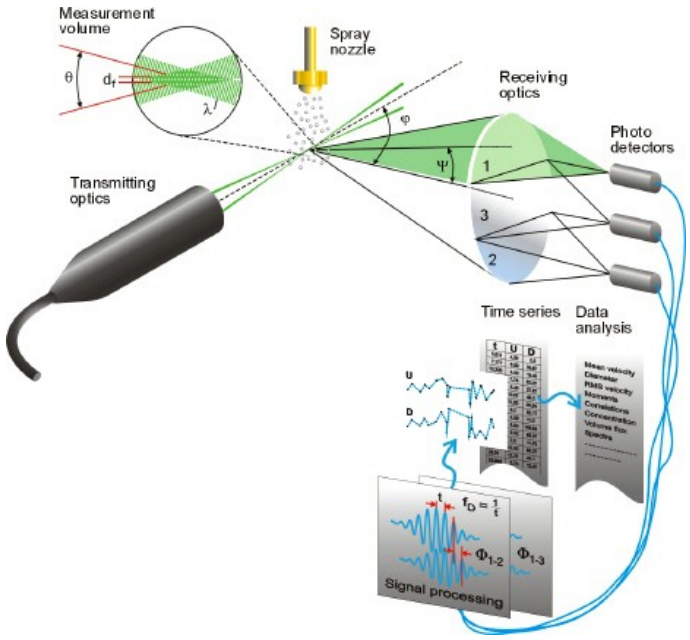

Figure 1.2: PDA principle. [Dantec Dynamics, 2014b]

The particles move through a small sample volume where two focused laser beams interact. Each particle will scatter the light from the laser beams and generate an optical interference pattern. The scattered light is then projected onto multiple detectors with the help of receiving optics. A doppler burst is generated from each detector based on the

optical signal, which has a frequency proportional with the velocity of the particle. The particle diameter is determined from the phase shift between doppler signals received by the detectors. The drawback for this method arises in the small sample volume where only one particle is measured at the time. In combination, there is no distribution in relation to the position in the flow. [Dantec Dynamics, 2014b] The laser components in the setup places PDA in the class of expensive methods for particle characterisation.

1.4.2 Interferometric Particle Imaging

Interferometric Particle Imaging (IPI) is a method utilising laser with light sheet optics and a double camera along with additional software, see Figure 1.3. It measures size and velocity of transparent spherical particles like drops or air bubbles. The principle is that the two cameras are pointed against the same area in the light sheet whereof both field of views are calibrated and perfectly coincided. When the particles enter the laser sheet they reflect and refract light in the form of two glare points. By moving the image plane away from the focal plane, the two glare points will overlap and show the interference pattern of the light from which the fringe spacing can be used to estimate the particle size. The light sheet is double pulsed and used to register velocity. [Dantec Dynamics, 2014a]

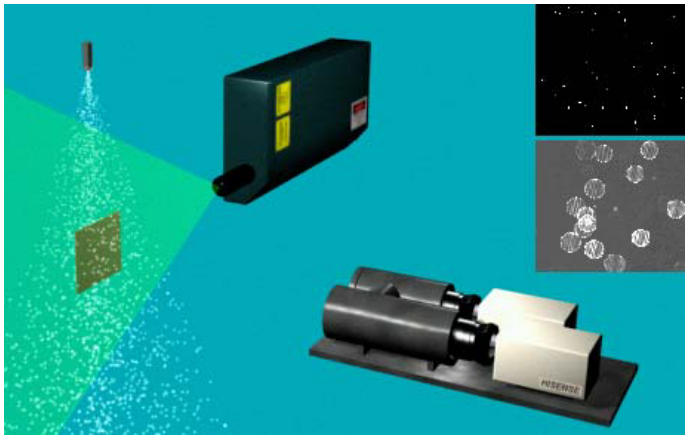

Figure 1.3: IPI principle. [Dantec Dynamics, 2014a]

Like PDA, the drawback of considering spherical particles is valid as well for IPI. Additional drawbacks arise in the limitation of regions of high particle concentration as a result of overlapping and additional effects of multiple scattering [Coghe and Cossali, 2011]. As for PDA, the setup requires two lasers which strongly affect the price of the setup.

1.4.3 Shadow Sizing

Shadow Sizing, referred to as Direct Image Method (DIM), measures size, velocity and shape of the particles. The particles can be either liquid droplets, solids or bubbles and as long as the contour is well defined any particle shape will do. The setup is simple and consists of a light source, a camera and software for image acquisition and subsequent digital image processing, see Figure 1.4. The camera acquires the shadows of the particles which is exposed to edge detection algorithm to estimate the particle shape. A particle

tracking algorithm can be used between to images taken with a small time interval, in order to estimate the velocity. [Dantec Dynamics, 2014c]

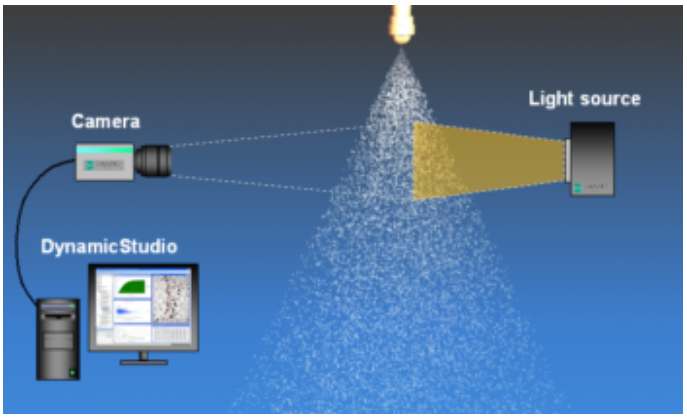

Figure 1.4: Shadow Sizing principle. [Dantec Dynamics, 2014c]

DIM has first become suitable for particle sizing as CCD cameras with high resolution and fast image processing have become available. The technique is suitable for estimation of particle size for larger particles located in dilute systems. The drawbacks of DIM arise in how the size of the observation volume is defined and a compromise has to be made between the field of view and the resolution of the camera. [Damaschke et al., 2005] A strong benefit in comparison to the setup of PDA and IPI is the price. DIM does not require any laser with advanced operating system placing the price as minimum 25.000 DKK.

Based on experience from the previous work with DIM, it was considered as a method of high potential. Still there was room for improvements concerning the applied diffuse backlight which complicated the idea of an universal digital image processing. With regards to the volume, the use of a single camera highlighted the need for present spherical bubbles for performing a reliable size distribution.

1.5 Improved DIM

To improve the bubbles edges and avoiding time consuming computations, ways of optimising the DIM are undertaken. One very promising improvement for DIM is to equip it with a telecentric lens and directed lighting known as telecentric lighting, see Figure 1.5. It shows the principle of how a telecentric lens in conjunction with directed lighting can improve DIM.

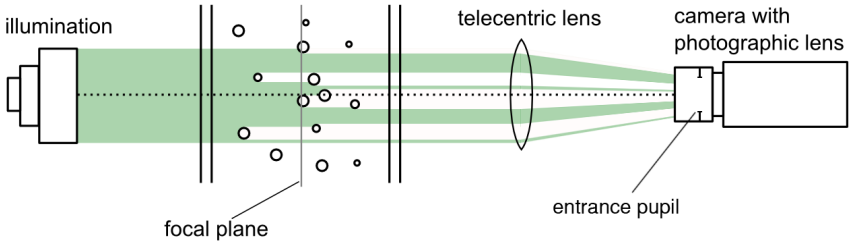

Figure 1.5: Illustration of improved DIM with a telecentric lens. [Mischler et al., 2010]

It will enhance the edges of the bubbles to a greater extent compared to an ordinary lens and a diffuse light source, making it easier to perform digital image processing on the acquired images. Thereto comes the choice of a camera with specifications best feasible for bubble size estimation.

1.5.1 Camera

A camera with a Charged Coupled Device (CCD) image sensor is desirable for image acquisition, since it has a very low noise [Hornberg, 2006,p. 378]. Regarding whether the camera must be colour or monochrome the choice is based on edge enhancement. A colour camera utilises a colour filter array in front of each pixel of a monochrome sensor, typically a Bayer filter. It makes each pixel measure the intensity in either a red, green or blue range dependent on which is placed in front of each pixel. To obtain similar resolution as for the original camera resolution demosaicing is performed, where interpolation is made between the two colour values which are missing for each pixel. The problem arises in that colours are created by the three colours separated in physically different locations, which leads to lower resolution compared to a monochromatic camera. Regarding edges, then a colour camera will generate colour aliasing and consequently a lower spatial resolution. In addition, the bubbles do not have any colour information which is particularly useful. [fluidimaging.com, 2014]

The desired shutter is a global and not rolling type. The global shutter exposures all the pixels simultaneously, from the exposure time begins to it ends, making it suitable when dealing with fast moving objects. Unlike the rolling shutter, which acts as a series of exposures row after row, such that the exposure time does not start and end simultaneously. It will create distortion on fast moving objects. [Basler, 2014b]

1.5.2 Lens

The benefits of a telecentric lens to a regular lens are many when considering the field of particle size estimation. It especially concerns the size of the volume of measurement.

A telecentric lens gives a reliable measurement volume equal to Field of View (FOV) times the telecentric depth where only a single calibration is necessary in the centre of the volume. Unlike a regular lens, where additional calibrations are necessary to achieve a similar measurements volume due to the presence of magnification and perspective angle error.

1.5.3 Light

Beside the benefit of not decreasing the diameter of curved transparent edges, the telecentric light also requires lower light intensity in comparison to a diffuse lighting. By having telecentric lighting a lower exposure time can be set for the camera, since it will take longer time for the diffuse lighting to saturate the image plan. It is beneficial when dealing with fast moving objects.

1.6 Verification Method

By making sure the results of the improved DIM are reliable, an acknowledged experiment must be conducted for reference and confirmation of the reliability. IPI is considered as a highly accurate size measurement method and can be used as a reference for DIM. An IPI setup is available at the Institute of Energy at Aalborg University which is another reason for choosing IPI above PDA, since both methods seems to be equally reliable. Additionally, IPI makes measurements within a bigger sample volume for which a lower number of samples are necessary to obtain a bubble size distribution. It must be kept in mind that the sampling strongly depends on the velocity of the particles where a low velocity will increase the sampling time for IPI, since the same bubble may not be sampled twice. Still, IPI has the advantage of giving an instantaneous image of the distribution between the bubbles.

Problem Statement 2

The interest within the field of multiphase flow measurements has grown in conjunction with the increased usage of theoretical data, which is lacking when it comes to detailed information regarding different particle characteristics inside the flow. Many companies have a great interest for such data. Among them is Tetra Pak Scanima, who sees the usefulness in connection with access to performance data of their batch mixers regarding the air bubble size distribution in the product. By utilising two-phase flow measurement techniques instead of theoretical data, it will pave the way for an in-line monitoring system for the content of dissolved air in the product leaving their batch mixers. In such context, the measurements have to be accurate but also affordable and easy to implement. With regards to these requirements the Direct Image Method (DIM) seems as a suitable candidate for such a system. Nevertheless, previous work has shown room for improvement which can be obtained by applying a telecentric lens. Additional types of measurement methods exist capable of estimating the content of dissolved air but are expensive and more difficult to implement.

How to develop an accurate in-line monitoring system based on the Direct Image Method in conjunction with a telecentric lens, capable of estimating the air bubble distribution in a two-phase flow represented by a column of stagnant water with rising bubbles? Additionally, can the accuracy of this system be verified through Interferometric Particle Imaging?

The objective of the report is to provide a basis for a system to estimate the size distribution of rising bubbles in a water column based on multiphase flow analysis and image based measurements. Interferometric Particle Imaging (IPI) is applied as a highly accurate, slow and costly method for particle size determination, which in this context is used for validation purposes. A DIM system in conjunction with a telecentric lens is applied as an inexpensive alternative to the IPI system. The acquired images for the Telecentric Direct Image Method (TDIM) are analysed by digital image processing. Both methods are applied on the preliminary studied setup described in Design & Test of Experimental Setup for Rising Bubbles - Appendix B.

Interferometric Particle Imaging for Bubble Measurement 3

The chapter will start out covering the theory and concept of the measurement technique Interferometric Particle Imaging (IPI), which is based on light scattering through bubbles. Thereto is made a derivation of the optical relation in order to estimate the bubble diameter from interference of light scattered from the bubbles. Different settings regarding the setup will be discussed, since these settings have a high influence on the quality of the acquired images of the rising bubbles. The IPI image processing is explained by how two image frames work together and which kind of processes are used in order to perform particle detection, size and velocity measurements. At last a review is made of the results for the bubble size distribution.

3.1 Introduction

IPI is a technique to measure transparent particles. It can estimate the current size and the individual locations of a large number of particles in a two-phase flow restricted by the measured control volume. Combined with Particle Tracking Velocimetry (PTV) the velocities of the particles can be obtained as well. The two methods are combined and utilised with the system Flow Manager with the extension of IPI, consisting of a software package FlowMap Particle Sizer (FMPS), two CCD cameras, a Nd:YAG laser and a Dantec Flowmapper processor. [Dantec Dynamics, 2014a]

One downside of the IPI method is that it only gives one diameter and thereby assumes perfect spherical bubbles. Furthermore the particles must be transparent, which fortunately is not a problem for an air bubble. As outlined in Vertical Bubble Flow - Appendix A, the bubbles obtain a spherical shape when the Eötvös number is low as a result of a small bubble diameter. Thereby the assumption of spherically particles is considered valid.

3.2 Bubble Diameter based on Light Scattering

The first to introduce the basic technique of IPI was König et al. [1986]. In the literature the technique has a variety of different names, such as Mie Scattering Imaging (MSI) and Interferometric Laser Imaging for Droplet Sizing (ILIDS) but here it will be referred to as IPI. [Dehaeck and van Beeck, 2008]

The way light is scattered by two phases in a flow is based on the relative refractive index. The relative refractive index, m, is defined as the relation between the index of refraction of the particle, n_p, and the surrounding medium, n_m, ($m = n_p/n_m$), where m can be above or below unity. For the case of bubble flow in water, the refractive index of air will be used for particles, n_a, while the refractive index of water will be used for medium, n_w. The relative refractive index will become less than unity, $m < 1$. The relevant relations for finding the bubble diameter is given by Maeda et al. [2000b] partly in article [Maeda et al., 2000b] and [Maeda et al., 2000a]. However, the derivation of the relations for this technique is not given, but Semidetnov and Tropea [2003] has taken the task to derive the relation and outline the limits of validity.

3.2.1 Working Principle

IPI is based on light scattered from the bubble when it is illuminated. The illumination source is a laser, which in this case forms a sheet vertically through the bubble column. See Design and Test of Experimental Setup for Rising Bubbles - Appendix B for further information above the bubble column. The intensity of the scattered light can be found by Lorenz-Mie Theory (LMT) [Albrecht et al., 2003,pp. 96]. This theory is not elaborated further, but results in a figure used to argue for an observation angle. When observing the laser sheet from a specific observation angle, glare points from the bubbles appear. In Figure 3.1 is shown how two glare points from a bubble in the laser sheet are detected by the camera sensor. The glare points are only visible, when the focus plan is located at the laser sheet.

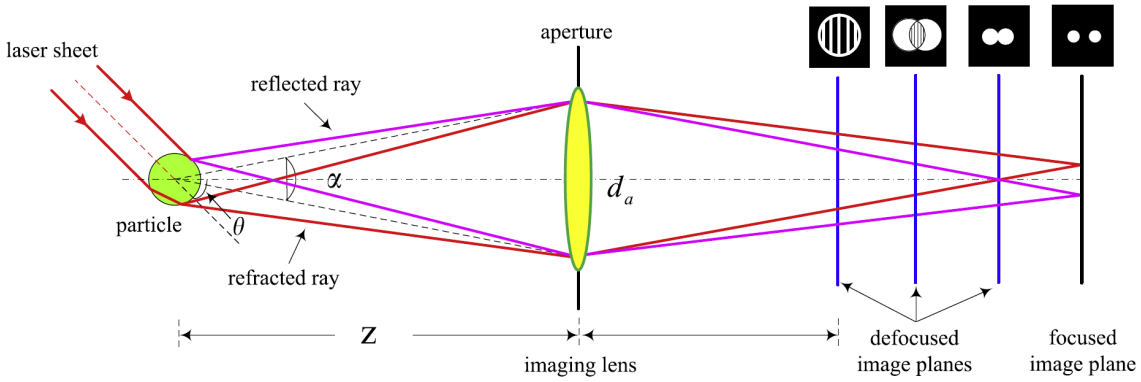

Figure 3.1: Defocusing of the image plane from the laser sheet makes the interference fringes from the glare points visible. Four images at different image planes are shown in the upper right corner. [Qieni et al., 2013] - modified

If the focus plan of the camera is not at the bubble in the laser sheet, interference fringes from the glare points are observed instead. In Figure 3.1 the focus plan is moved further

away from the focused image plane. At a certain point the glare points make a complete overlap, which gives the interference pattern. Figure 3.1 shows the path of the light rays starting from the laser sheet through the bubble and further to the lens of the camera and in the end to the CCD sensor in the camera.

The interference pattern in the defocused plane depends on the relative refractive index, m, the bubble diameter, d_b, and the observation angle, ϕ, of the camera relative to the laser sheet. To obtain a good signal to noise ratio of the fringes in the interference pattern a high contrast is important. Dantec Dynamics [2003] recommends the relative refractive index, m, to be below 0.8 or above 1.2 for obtaining good contrast. With air bubbles in water $m = 0.75$, from which the recommendation is considered as fulfilled.

3.2.2 Light Scattering

In Figure 3.2 LMT calculations are applied to a bubble with a diameter of 100 μm and a relative refractive index of 0.75, illuminated by a laser sheet with a wavelength of $\lambda =$ 520 nm [Shiliang, 2005,p. 13]. The polarisation of the laser sheet is applied parallel to the orientation of the laser sheet. Figure 3.2 shows the light intensity as a function of the scattering angle. An angle of 0° corresponds to a normal direction with respect to the direction of the applied laser sheet.

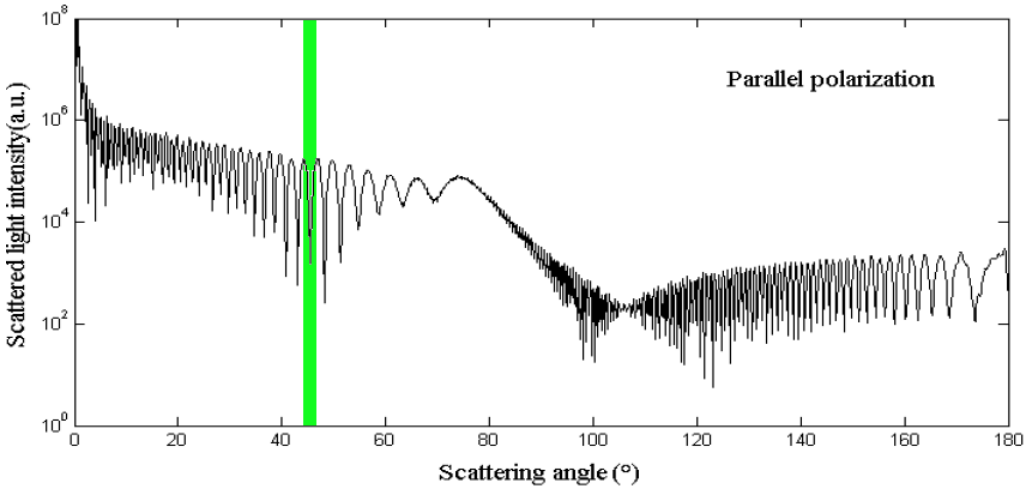

Figure 3.2: Intensity of light scattered of an air bubble in water as function of the scattering angle. The line indicates how the light intensity changes a function of the scattering angle. [Shiliang, 2005,p. 13] - modified

The wide change of the scattered light intensity is due to interference between the reflected, refracted and diffracted light from the bubble. A high contrast is obtained where a high change of the intensity occurs. For the scenario given in Figure 3.2, a high contrast can be obtained at approximately an angle of 45°. The scattered light pattern is independent of the light intensity of the applied laser sheet. This means that the interference pattern detected by the camera is also independent of the applied laser intensity, which is an advantage of the IPI method. However, to capture useful images for further processing the applied laser intensity should be adjusted with respect to the shutter time and aperture size of the lens. [Shiliang, 2005]

The LMT scattering can be decomposed into modes of different light scattering orders by applying Debye Series [Albrecht et al., 2003]. Figure 3.3 shows the decomposing of the scattered light in Figure 3.2 [Shiliang, 2005,p. 21]. The scattered light are decomposed into three modes: Reflection including diffraction, 1^{st} order refraction and higher order refractions. Referring to Figure 3.1 the reflected and diffracted light are scattered of the surface of the bubble. The 1^{st} order refraction passes through the bubble surface and leave it again. The higher order refractions are not shown in the figure but will be indicated as light being reflected multiple times inside the bubble, before refraction through the surface.

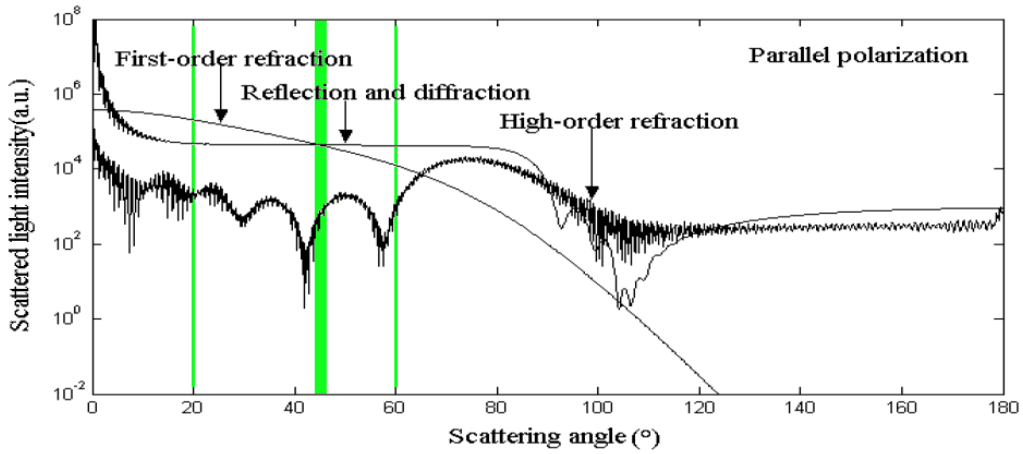

Figure 3.3: Three modes of scattered light intensity from an air bubble in water as function of the scattering angle. [Shiliang, 2005,p. 21] - modified

From Figure 3.3 it can be seen that the reflection and 1^{st} order refraction are dominating in the range 20° to 60°. The two modes are visible seen as glare points at the bubble surface, see Figure 3.1. They are of equal intensity at around 45°, which corresponds to the highest contrast in Figure 3.2. For that reason it is recommended to set the observation angle of the camera equal to the scattering angle at which the intensity of the reflected and 1^{st} order refracted light is at the same level.

3.2.3 Derivation of Optical Relation

The distance in between the two glare points can be found from the frequency of the fringe in the interference pattern. The background for the derivation of this relation is Young's interference experiment, see Figure 3.4. At Young's interference experiment a coherent and monochromatic light source is pointed at two parallel slits. The light emerging from the slits deviates and forms two curved wave fronts. Two types of interference are created between the waves after the slits; constructive and destructive. By placing a viewing screen behind the slits, the interference is made visible. Constructive interference of two light rays is seen as the fringes, whereas the destructive interference between two light rays is seen as dark bands. [Jewett and Serway, 2008,pp. 1051-1053]

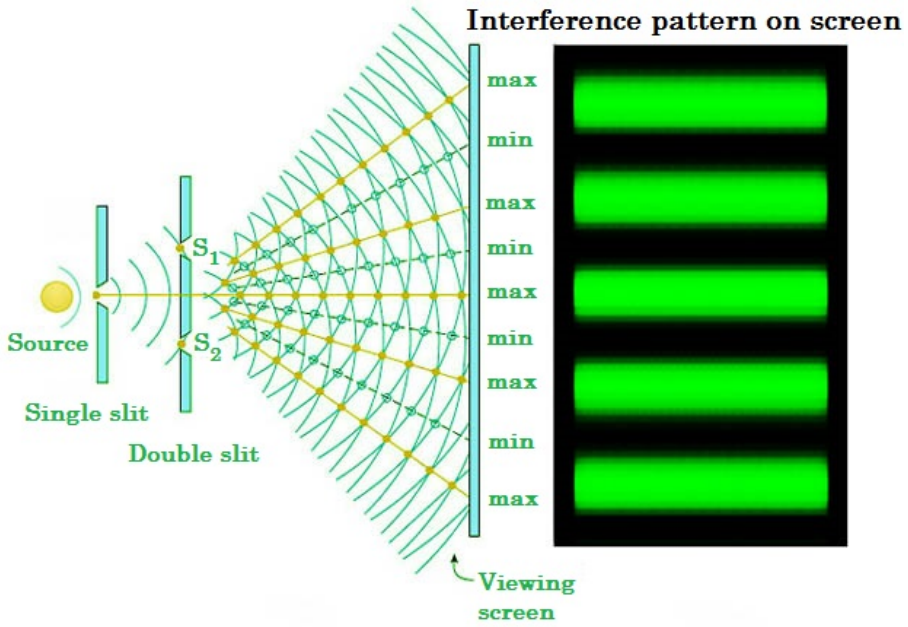

Figure 3.4: Young's double slit experiment. [h2physics, 2014] - modified

Instead of the light emitted from the two slits, the two glare points from the bubble surface are used. A linear relation between the numbers of fringes, N, and the bubble diameter, d_b, can be derived. The derivation is based on a transparent spherical particle and the distance between the reflective and 1^{st} order refractive scattering. In Figure 3.5 the optical path of the two rays, reflected and refracted, giving the observed glare points, are shown. The detector is the sensor at the camera.

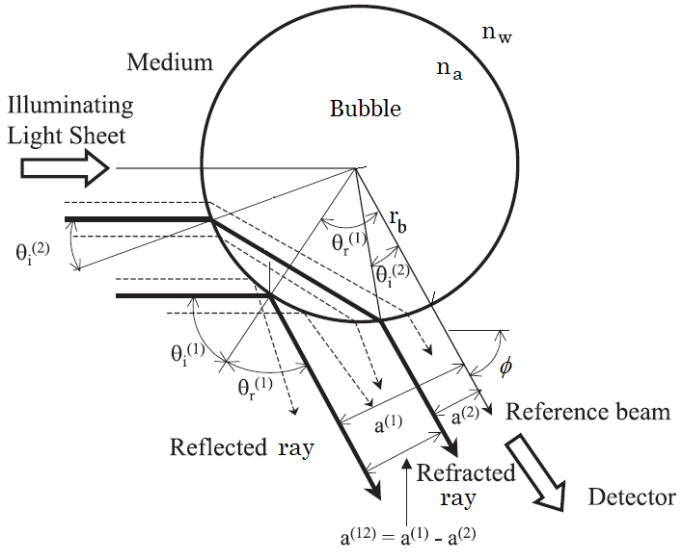

Figure 3.5: The ray path of the reflected and 1^{st} order refracted rays giving the observed glare points. [Semidetnov and Tropea, 2003] - modified

The derivation of the relations are documented by Semidetnov and Tropea [2003]. The main points from this derivation are outlined in the following to give an understanding of the relation between the spacing of the fringes and the particle diameter. Semidetnov and Tropea [2003] shows two approaches for derivation of the relations. The first finds the difference in the path length of the scattering orders through the particle. The second sees the two glare points as two light sources and uses the analogy from Young's fringe experiment.

From Young's fringe experiment the spacing between the fringes, σ, at the sensor is given by Equation 3.1.

$$\sigma = \frac{\lambda}{n_w} \frac{Z}{a^{(12)}} \quad [-] \tag{3.1}$$

Where:
σ is the spacing between the fringes [μm]
λ is the wave length of the laser beam in vacuum [nm]
n_w is the refractive index of the medium, water [-]
Z is the distance to the particle from the receiving aperture, see Figure 3.1 [mm]
$a^{(12)}$ is the glare point separation spacing, see Figure 3.5 [μm]

The distance between the two rays, $a^{(12)}$, can be found as a function of the bubble diameter, d_b. To find the distance, each ray displacement relative to a hypothetical reference beam is found. The path of the reference beam goes through the centre of the bubble, see Figure 3.5. Then the difference is given as the displacement in between the two rays. The displacement of the reflected ray, $a^{(1)}$, is given in Equation 3.2 and the displacement of refracted ray, $a^{(2)}$, is shown in Equation 3.3.

$$a^{(1)} = r_b sin\left(\theta_r^{(1)}\right) \quad [\mu m] \tag{3.2}$$
$$= r_b cos\left(\frac{\phi}{2}\right) \quad [\mu m]$$

$$a^{(2)} = r_b sin\left(\theta_i^{(2)}\right) \quad [\mu m] \tag{3.3}$$
$$= r_b \frac{m sin(\phi/2)}{\sqrt{1 + m^2 - 2m cos(\phi/2)}} \quad [\mu m]$$

Where:
r_b is the radius of the bubble [μm]
$\theta_r^{(1)}$ is the reflecting angle [°]
ϕ is the scattering angle [°]
$\theta_i^{(2)}$ is the incident angle [°]
m is the relative refractive index $= n_a/n_w$ [-]

The distance between the two rays, $a^{(12)}$, is found by Equation 3.4.

$$a^{(12)} = a^{(1)} - a^{(2)} \quad [\mu m] \tag{3.4}$$
$$= r_b \left(cos\left(\frac{\phi}{2}\right) - \frac{m sin(\phi/2)}{\sqrt{1 + m^2 - 2m cos(\phi/2)}} \right) \quad [\mu m]$$

The angular spacing between the fringes, $\Delta\varphi$, is related to the spacing between the fringes as shown in Equation 3.5. The expression for the angular spacing is derived through Equation 3.5 to 3.7, by use of Equation 3.1 and 3.4.

$$\Delta\varphi = \frac{\sigma}{Z} \quad [°] \tag{3.5}$$

$\Downarrow$ Equation 3.1

$$= \frac{\lambda}{n_w} \frac{1}{a^{(12)}} \quad [°] \tag{3.6}$$

$\Downarrow$ Equation 3.4, where $r_b = d_b/2$

$$\Delta\varphi = \frac{2\lambda}{d_b n_w} \left(cos\left(\frac{\phi}{2}\right) - \frac{m sin(\phi/2)}{\sqrt{1 + m^2 - 2m cos(\phi/2)}} \right)^{-1} \quad [°] \tag{3.7}$$

Where:
$\Delta\varphi$ is the angular fringe spacing [°]

The maximum observation angle for this optical approach, is given by $2cos^{-1}(m)$ and is for air bubbles in water equal to 82.8° [Semidetnov and Tropea, 2003].

The number of fringes in the interference pattern, N, can be found by the relation between the angular aperture of the optic, α, and the angular fringe spacing, $\Delta\varphi$, as shown in Equation 3.8. The angular aperture, α, is given in Equation 3.9 and shown in Figure 3.1.

$$N = \frac{\alpha}{\Delta\varphi} \quad [-] \tag{3.8}$$

$$\alpha = 2tan^{-1}\left(\frac{d_a}{2Z}\right) \quad [^\circ] \tag{3.9}$$

Where:
α is the angular aperture of the optic [°]
d_a is the aperture diameter [mm]

Equation 3.8 can be derived to be a linear relation between the number of fringes, N, and the bubble diameter, d_b. Equation 3.10 shows the relation where κ is a geometrical factor containing the parameters. κ is given in Equation 3.11.

$$d_b = N\kappa \quad [\mu\text{m}] \tag{3.10}$$

$$\kappa = \frac{\lambda}{tan^{-1}\left(d_a/2Z\right) n_w}\left(cos\left(\frac{\phi}{2}\right) - \frac{msin(\phi/2)}{\sqrt{1+m^2-2mcos(\phi/2)}}\right)^{-1} \quad [\mu\text{m}] \tag{3.11}$$

Where:
N is the number of fringes [−]
κ is a geometric factor [μm]
d_b is the bubble diameter [μm]

The constant, κ, consists of a list of different constants and settings in the experimental setup. Some of them are locked, while others are adjustable. The wavelength of the laser, the relative refractive index and the diameter of the optic aperture are locked. The two setup parameters, distance Z and the scattering angle, ϕ, are the ones to be adjusted.

A limit bubble size range can be found from the limitations of IPI. A minimum bubble diameter, d_{min}, is given by Equation 3.12. This corresponds to a single fringe in the interference image. [Dantec Dynamics, 2003]

$$d_{min} = \frac{1}{\kappa} \quad [\mu\text{m}] \tag{3.12}$$

The maximum size of a bubble, d_{max} is given in Equation 3.13. A minimum of two pixels to define a fringe in the image is used for the Nyquist criteria. [Dantec Dynamics, 2003]

$$d_{max} = \frac{n_x}{2\kappa\Delta x}\left[1 - z_r\left(\frac{1}{f} - \frac{1}{z_l}\right)\right] \quad [\mu\text{m}] \tag{3.13}$$

Where:
n_x is the number of pixels in the x-direction [−]
Δx is the dimension of the camera sensor in the x-direction [mm]
z_r is the distance from the lens to the camera sensor [mm]
f is the focal length [mm]
z_l is the minimum standoff distance [mm]

3.3 Settings of Optical Setup

The adjustable settings for the optical setup are shown in Figure 3.6. In Figure 3.6a is shown a top view sketch of the optical setup with the Nd:YAG laser shooting into the water column such that the two cameras can take images of the bubbles inside the laser sheet. A side view is shown in Figure 3.6b showing the bubbles rising into the laser sheet and FOV. The two cameras are mounted in a double camera mount, which apply the same FOV to the cameras. Various settings are indicated in Figure 3.6 which all have been selected from a theoretical and experimental approach. The initial settings are based on the theoretical approach but adjustments on the optical setup turn out to give more promising results.

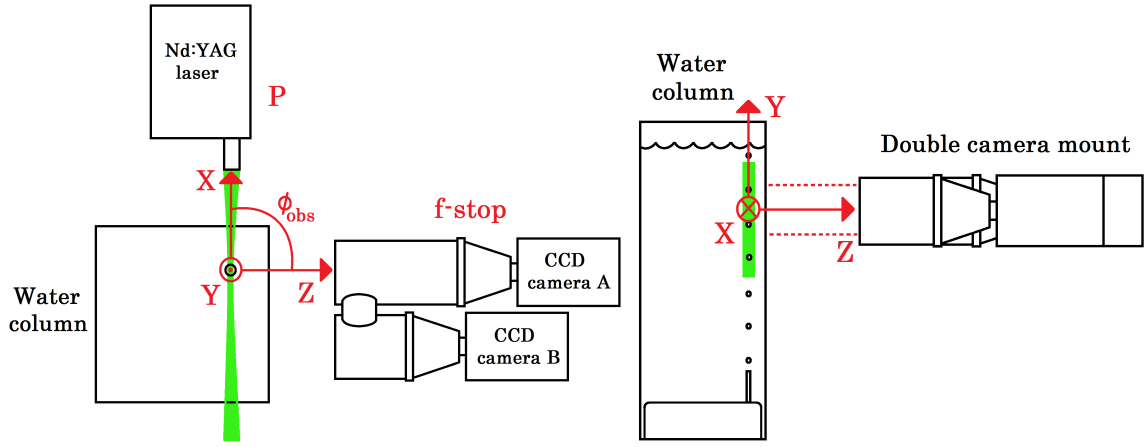

(a) Top view. (b) Side view.

Figure 3.6: Indicated parameters for the optical setup viewed from the top and side.

Table 3.1 shows the applied settings along with the settings for the Nd:YAG laser. The settings for the laser are explained in Working Principles of Laser used for IPI - Appendix E.

Focal distance of laser, X	400	mm
Observation angle, ϕ_{obs}	35	°
Distance from camera lens to laser sheet, Z	298.4	mm
f-stop number	f/2.8	-
Pulse width	10	ns
Max number of pulses	2	-
Repetition rate	8 or 125	Hz or ms
Flash/laser power, P	120	mJ
Pulse interval	10,000	μs
Light pulses per recording	2	-
Time between bursts	1,000	ms
Number of recordings per burst	1	-
Number of bursts	2,000	-

Table 3.1: Settings for the optical setup indicated in Figure 3.6 and the Nd:YAG laser.

The following will address to how the different optical settings have been determined and subsequently adjusted.

Focal Distance of Laser, X

A laser sheet is set vertical parallel to surface of the bubble column. The spatial resolution in the depth of field (DOF) can be optimised by generating a thin light sheet of high intensity. Based on Working Principles of Laser used for IPI - Appendix E the adjuster on the opening of the laser is set to fit a focal distance of 300 mm with the Nd:YAG located 300 mm away from the rising bubbles. According to the light sheet thickness as function of the distance from the laser in Figure E.7 a thickness of 0.6 mm should be given. However, the bubble column refracts the laser and increases the focal distance. In this manner adjustments are made making the waist being located at the rising bubbles by placing the Nd:YAG laser at a focal distance X of 400 mm.

Observation Angle ϕ_{obs}

According to the Figures 3.2 and 3.3 displaying the light scattering, an angle at 45° should be the optimum. However Dantec Dynamics [2003] recommend to use the theoretical found angle as a guidance, and fine tune the angle by trial and error to optimise the contrast in the interference pattern. When adjusting the angle, the refraction of light through the plexiglass column should be taken into account. Section C.2.1 in IPI Software Settings - Appendix C gives the relation between the angle inside the plexiglass column and outside. To have an scattering angle of 45° inside, the observation angle outside should be 19.4°. The observed interference pattern at an angle of 20° was not found feasible for IPI processing. Different angles were tested. An angle observation of $\phi_{obs} = 35°$ was found to give the best contrast in the interference pattern. This angle correspond to an scattering angle of 52.07°.

Distance Z

The distance Z from the camera lens to the laser sheet is not considered to be a straight line. Due to an off-axis angle below 90°, Z will vary across the FOV. The distance can be calculated based on the distance from the centre of the lens to the centre of the FOV in the laser sheet. The distance is characterised as the distance at which the refracted light from the bubbles travel. Based on the observation angle of 35°, the distance Z can be calculated for which the light travels from the water to the air medium. In Section C.2.1.2 in IPI Software Settings - Appendix C distance Z is visualised and found to 298.4 mm.

f-stop

The f-stop number is set to f/2.8 for reducing the need of a high flash/laser power, P, while still achieving fringes useable for further processing.

Adjustments of Double Camera Mount

The double camera mount contains two lenses which are supposed to be looking at the same FOV. This is achieved by the use of an incorporated mirror which must be adjusted so both cameras are looking at the same FOV while the lenses are in focus at the same focal point. When camera B is defocused, the focus plan is moved backwards and thereby the working distance is changed. It can be viewed in the image where there will be a shift in the x-direction due to the off-angle and scattering. Additionally, the double camera mount is flipped 180° to not interact with the laser beam.

3.4 IPI Image Processing in FMPS

Two cameras are utilised for the image acquirement, one focused relative to the laser sheet (camera A) and one defocused (camera B) relative to the laser sheet. Each camera grabs a frame for each pulse interval from the laser. Thereby each measurement contains 4 images; frame A1, frame A2, frame B1 and frame B2. Referring to both frame A1 and A2 as image A and likewise for frame B1 and B2 as image B. Image A is used for particle detection and velocity measurements, while image B is used for size measurements and validation purposes. The complete IPI image processing which is performed in FlowMap Particle Sizer (FMPS) is shown in Figure 3.7. IPI Software Settings - Appendix C state the chosen settings for FMPS.

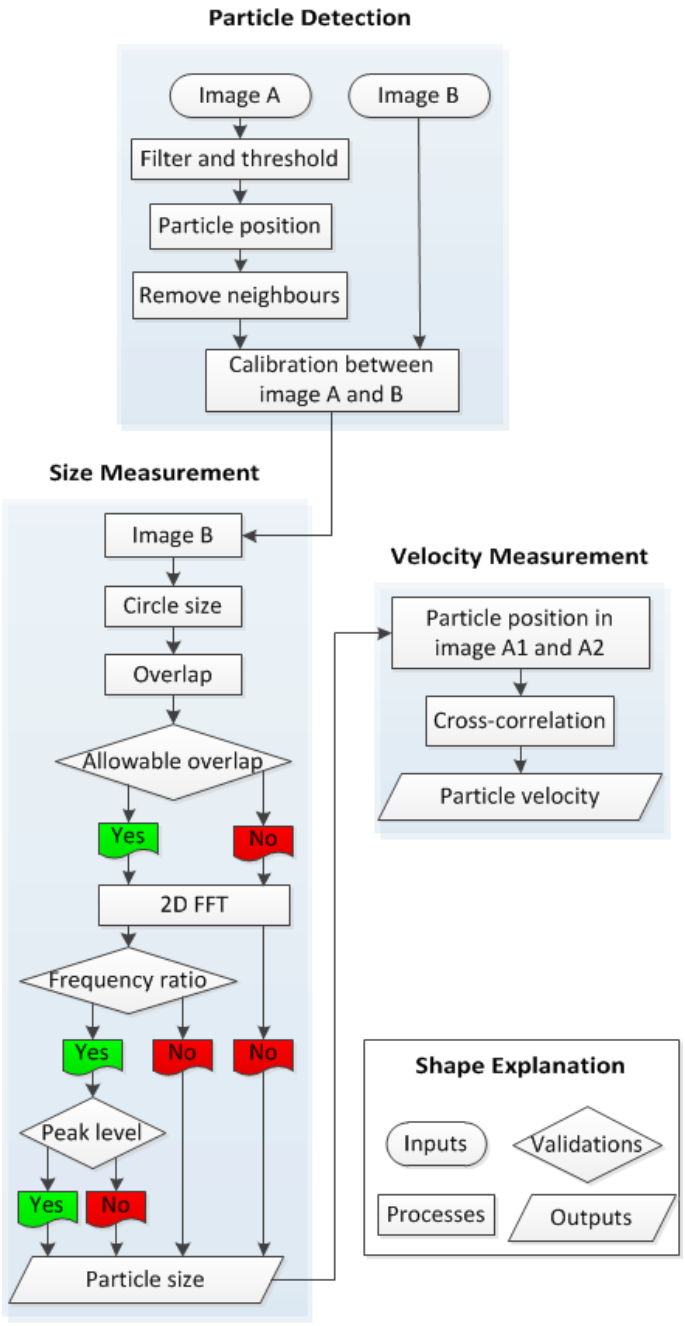

Figure 3.7: IPI image processing including Particle Detection, Size Measurement and Velocity Measurement.

3.4.1 Particle Detection

First the particles, in this case glare points, need to be detected in image A. The acquired image will contain noise which is reduced by applying a filter. In addition, threshold is applied given in percentage of the resolution of the camera to remove background noise. The particle position is then identified. A last step is added to remove neighbouring particles located a few pixels from one another. It will help improving the upcoming overall validation, especially for regions of high concentration of glare points. Calibration is applied to calculate the transformation of the particle coordinates from image A to image B. A further outline is given in Calibration for IPI & TDIM - Appendix D. [Dantec

Dynamics, 2003,pp. 2.6-2.8]

3.4.2 Size Measurement - Camera B

The circle size around the defocused glare points in image B is found from pre-processed masks for circle detection, which are cross-correlated with the interrogation area. The overlap of the circles is then determined, where overlapped regions between the circles are masked out whereof the remaining area is calculated. For the remaining area, 2D FFT is applied where the peak (fringes) locations are detected by 2D gaussian interpolation. The size information can then be calculated. [Dantec Dynamics, 2003,pp. 2.8-2.9]

3.4.3 Validation

The validation in Figure 3.7 will affect the post-processing and decide if a particle is accepted (Yes) or neglected (No). The first validation criteria is the allowable overlap of the circles in Image B. Setting the value to 70 % will cause that any circle with more than 70 % of its area overlapped will not be accepted. [Dantec Dynamics, 2003,p. 2.9]

The frequency ratio criteria uses the fringe frequency in the x-direction, (F_x), and the fringe frequency in the y-direction, (F_y). With a fringe orientation given as in Figure 3.1, fringes in the x-direction will have small frequency peaks in the y-direction. It will result in a high frequency ratio, (F_x/F_y), an indication of good fringe definitions. Unlike a low frequency ratio, which is an indication of poor or no fringe definitions. [Dantec Dynamics, 2003,p. 2.10]

The last validation criteria is the peak level which is based on the height of the maximum peak frequency determined. A percentage is set to indicate how high the other peaks are allowed to be in relation to the highest peak. If the other peaks are low compared to the highest peak it is an indication of fringes of high contrast and low present noise. [Dantec Dynamics, 2003,p. 2.10]

3.4.4 Velocity Measurement - Camera A

The velocity measurement is based on frame A1 and A2. Particle Tracking Velocimetry (PTV) is applied in the FMPS software to calculate the best fit between frame A1 and A2 which are separated in time. It uses the displacement in the X and Y direction and consequently calculates the velocity. [Dantec Dynamics, 2003,p. 2.10] An illustration of the PTV principle is shown in Figure 3.8 which originally is based on Particle Image Velocimetry.

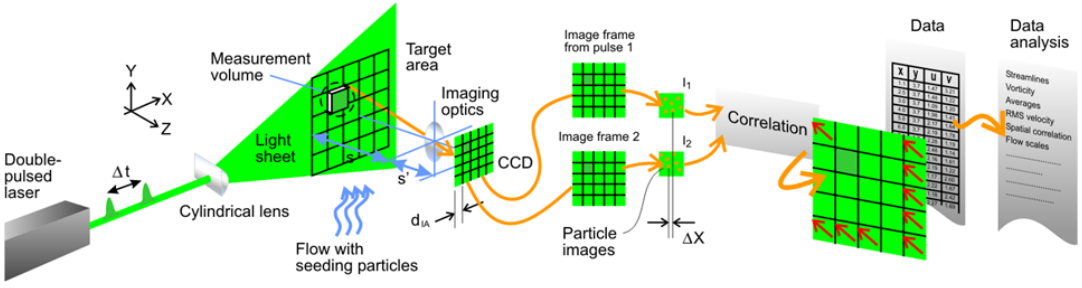

Figure 3.8: Visualised principle of PTV from Dantec Dynamics. [Andersen, 2014]

The light-sheet is pulsed to produce a stroboscopic effect which freezes the movement of particles. This is synchronised with the camera, making the particle positions being registered on frame 1 due to pulse 1 and the same goes for frame 2 and pulse 2. The acquired images are divided into interrogation areas, where frame 1 and frame 2 are correlated in order to generate an average particle displacement vector. Dividing by the time between the two frames, Δt, the result will be raw velocity vector maps. [Dantec Dynamics, 2000a,p. 4.2]

3.5 Results of IPI

The settings regarding pressure, number of samples etc. during the data acquisition for the IPI experiment are given in Table 3.2. Both the initial pressure and end pressure are listed, to show that the applied pressure air is not completely stable during the data acquisition. The temperature, T remains stable during the sample time.

$p_{t=0s}$	$p_{t=1999s}$	T_{water}	# images	Sample time
0.127 bar	0.120 bar	23.8°C	2000	33:19 min

Table 3.2: Settings during the data acquisition for the IPI experiment.

3.5.1 Data Selection and Processing

The data given by FMPS includes the position, size and velocity of the detected and validated bubbles, which are considered reliable based on the tests of settings in IPI Software Settings - Appendix C. Frame A1 and A2 are used for the position, frame B1 and B2 for the size, while the velocity is based on the displacement between frame A1 and A2 as shown in Figure 3.7.

The velocity is only available if the same bubble is being detected and validated in both frame A1 and A2. These bubbles are applied for further processing.

Regarding whether frame B1 or B2 is used for further processing should not matter in this case, since the bubble size should not change from one frame to the other. Still, both frames should not be utilised since it will make the same bubble size appear twice in the bubble size distribution. Thereof only the bubble size given from frame B1 is applied for further processing.

In the processing only those bubbles in a range varying from 0 to 1200 μm are used, based on the diameter range given by FMPS. FMPS utilises Equation 3.12 and 3.13 for calculating d_{min} and d_{max}, which are given in IPI Software Settings - Appendix C Table C.1. This is done even though bubbles are detected and validated at a diameter far beyond 1200 μm. These bubbles are however detected as being a single bubble, but consist of two bubbles placed behind one another, which affects the fringe pattern and consequently the calculated bubble diameter.

The distributions in the following figures will consist of 120 bins with each representing a diameter range of 10 μm. Each bar representing a bin is based on its centre value. Meaning that an interval range between 0 and 10 μm will use a diameter of 5 μm.

3.5.2 Bubble Size

Figure 3.9 shows the bubble diameter distribution obtained with the settings given in Table 3.2. Equation 3.14 shows how different types of diameters can be calculated. $D10$ is the mean diameter and $D32$ is the Sauter mean diameter, which has the same volume to surface area ratio as the entire bubble sample.

$$D_{pq} = \left(\frac{\sum_{i=1}^{N} d_i^p}{\sum_{i=1}^{N} d_i^q} \right)^{1/(p-q)} \quad [\mu\text{m}] \tag{3.14}$$

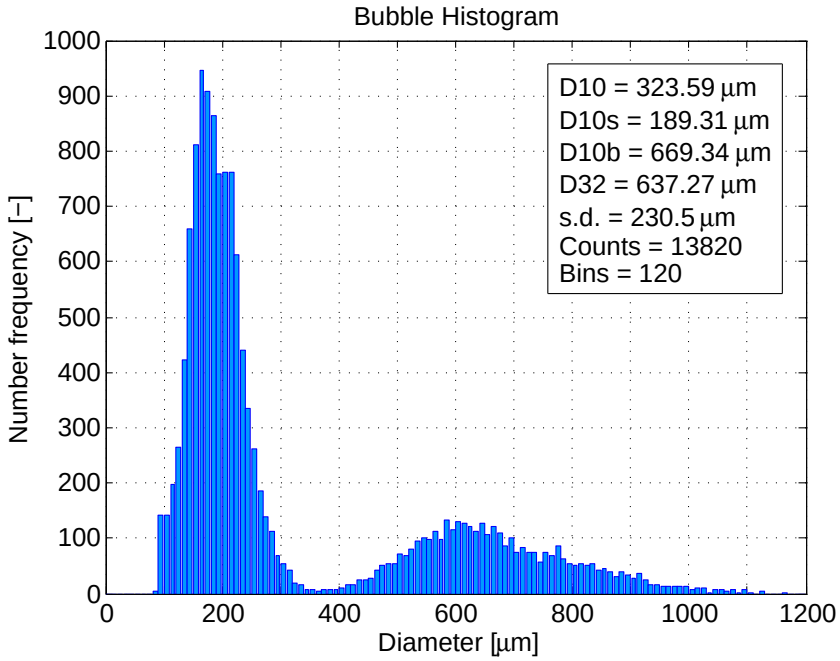

Figure 3.9: Bubble size distribution with the parameters given in Table C.1.

In Figure 3.9 there appear to be a bimodal distribution of the present bubble diameters. In this case, the calculated $D10$ will not represent the true mean of the distribution. Instead, $D10$ is calculated for both the category of small bubbles below ($D10s$) and above ($D10b$) a size of 365 μm in diameter. This value is chosen since it represents the diameter of the lowest bar between the two size categories.

3.5.3 Volume Size

From the extracted diameters shown in Figure 3.9 the volume frequency can be calculated. The volume is calculated based on the assumption that the diameters represent spherical bubbles. The result is shown in Figure 3.10 along with the total volume of the bubbles extracted from the 2000 images.

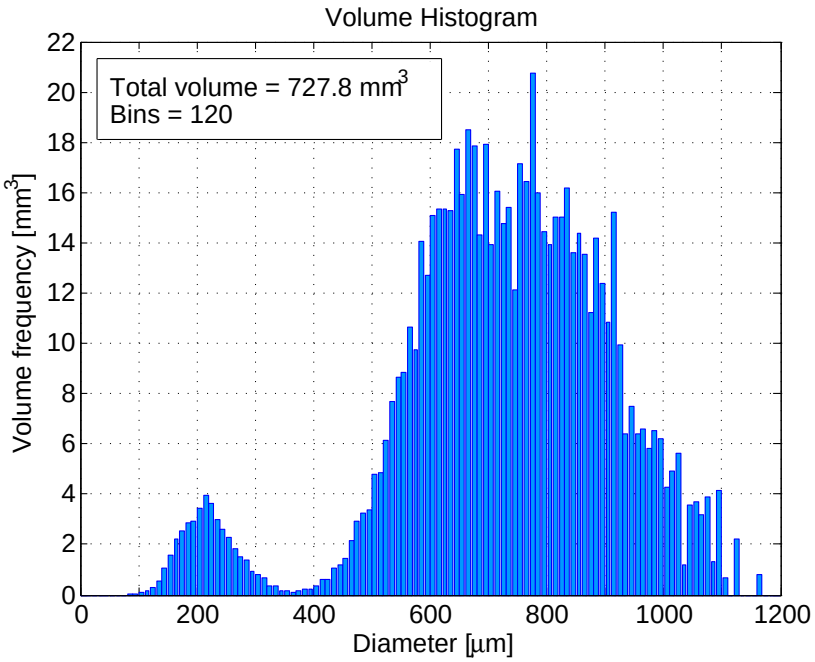

Figure 3.10: Volume size distribution as a function of the diameter.

It clearly shows that the category of big bubbles for $D10b$ contribute much more to the total volume in relation to the small bubbles for $D10s$. It is even though the number frequency is sincerely higher for $D10s$ than $D10b$ as shown in Figure 3.9.

Telecentric Direct Image Method for Bubble Measurement 4

The following describes the setup for performing the Telecentric Direct Image Method (TDIM). The procedure of the image processing for bubble contour extraction is outlined. The image processing is customised to extract only bubbles which are considered to be in focus. Finally, the results of the size distribution are presented.

4.1 Settings of Optical Setup

The bubble column described in Design & Test of Experimental Setup for Rising Bubbles - Appendix B, has been equipped with a monochrome CCD camera with a pixel resolution of 1296×996 and as optic a telecentric lens. See TDIM Principles & Equipment - Appendix G for specifications. The camera and lens are located on a traverse which can move the camera and lens along with and closer to the bubble column, but not up and down. The FOV is located above the cannula in the bottom of the water column. A steady white LED lamp is used as background light, which is located in order to align with the telecentric lens (E). The location of the camera, bubble column and light setting is shown in Figure 4.1 along with specified dimensions given in Table 4.1. See Design & Test of Experimental Setup for Rising Bubbles - Appendix B for additional dimensions of the plexiglass column and for the horisontal location (F) of FOV above the cannula.

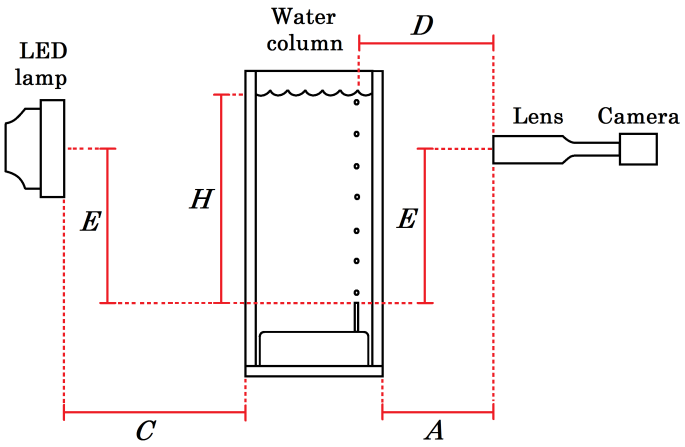

Figure 4.1: Sketch of the experimental setup of the TDIM including relevant dimensions.

	Description	Distance [mm]
A	Lens to the front of the water column	79
C	Back side of water column to front of LED lamp	148
D	Working Distance	109
E	Position of FOV and LED lamp	180
H	Water column above cannula	280

Table 4.1: Dimensional specification from Figure 4.1.

4.2 Image Acquisition and Settings

For subsequent comparison between the results of IPI in Section 3.5 and TDIM, 2000 images are acquired with the telecentric setup shown in Figure 4.1. Table 4.2 shows the settings during data acquisition regarding pressure, number of samples etc. As for the IPI settings, the initial and end pressure are specified to indicate that the pressure air is not completely stable. Two TDIM measurements are conducted, one before (TDIM 1) and one after (TDIM 2) the IPI measurements, shown in Interferometric Particle Imaging for Bubble Measurement - Chapter 3. It is done to be able to see if the unstable pressure air has influenced the number or shape of the bubbles.

	TDIM 1	**TDIM 2**
$p_{t=0s}$	0.123 bar	0.127 bar
$p_{t=500s}$	0.122 bar	0.128 bar
T	23.3 °C	23.8 °C
fps	4	4
Exposure time	16 μs	16 μs
# images	2000	2000
Sample time	8:20 min	8:20 min

Table 4.2: Settings during the data acquisition for the two TDIM experiments.

The exposure time is chosen based on the three images shown in Figure 4.2. A short exposure time is desirable to make the bubble move the shortest distance when acquiring the images. The fastest exposure time of the camera is 16 μs with its effect shown in Figure 4.2a. It creates a spotlight effect in the centre of the image, which increases the number of necessary steps in the image processing phase to extract the bubbles. By increasing the exposure time the spotlight effect covers a larger area of the image and consequently reduces the number of necessary steps for image processing.

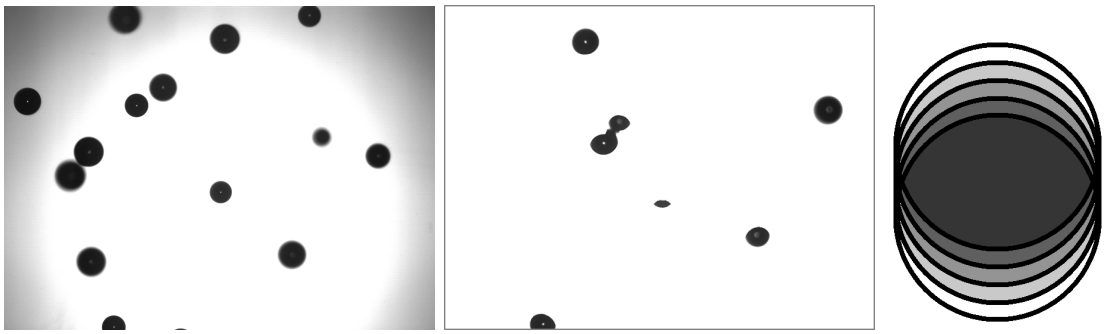

(a) Exposure time of 16 μs. (b) Exposure time of 50 μs. (c) Downside of high exposure time.

Figure 4.2: The effect of increasing exposure time from 16 to 50 μs.

But as seen in Figure 4.2b the consequence is a loss of the bubble area. The bubbles manage to move a certain distance during the exposure time where only the area constantly covered by the bubble will be present in the image. An illustration of this is shown in Figure 4.2c. To avoid this loss of significant bubble area, the exposure time is set at 16 μs.

4.3 Digital Image Processing

A solid digital image processing of the acquired images is necessary to exploit the full potential of TDIM. It must be representative and usable for all images acquired in the setup. The following will lead to the result of TDIM by going through the applied steps for the digital image processing. First image components are specified which are used in the pre-processing phase for removing the spotlight effect and noise present in the images. This part takes place in MATLAB along with contrast enhancement and adjustments of the GS range. The main image processing is done in NI Vision where steps such as edge detection, threshold and calibration are applied. A reference image is used to visually illustrate the effects throughout the digital image processing and to justify choice of processes.

4.3.1 Image Components

Each image can be divided into three parts of information, background, foreground and noise. The background represents the contour of the light source and the foreground the shadow contour of the rising bubbles. Both parts are infected by noise. To separate the shadow contour of the bubbles in the image, an image of the background and an image of

the noise are taken. The background image, I_B, is with the light switched on, but without any rising bubbles in the column. An average of 100 images is used. The background image is shown in Figure 4.3a.

The cells of a camera sensor produces some dark noise due to a phenomena called dark current [Hornberg, 2006,p. 421]. This dark noise together with noise from the surroundings of the experimental setup, such as light from other light sources in the laboratory, are represented in the noise image, I_N. The noise image is an average of 100 images taken with the back light switched off and no air bubbles in the water column. The noise level is very low for each image, so the average GS value for each pixel in the image varies only between 0 and 1. To display the noise pattern, the noise image is shown as binary in Figure 4.3b.

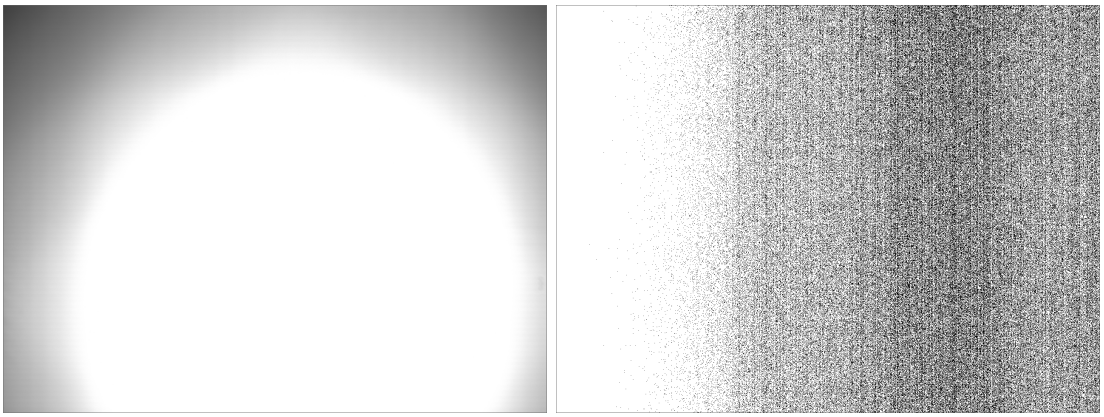

(a) Average background image.

(b) Average noise image. GS values: white = 1, black = 0.

Figure 4.3: Image components: average background image, I_B, and average noise image, I_N.

It is seen in Figure 4.3a that the LED light does not cover FOV entirely and thereby creates a spot light effect. The corners of the image are darker than the centre, which will make a global edge detection of the bubbles difficult. Figure 4.3b indicates an uneven distribution of the noise in the horisontal direction across the image. The left side of the image shows more noise compared to the rest. This could be caused by another light source in the laboratory. However the noise level is very low compared to real pixel values in the image and thereby it is considered to have no significant influence on the image processing and final result.

To display the foreground image component which contains the bubbles, the noise and background components have to be removed from the image. This process is described in the following section, which explains each step in the pre-processing of the images.

4.3.2 Image Pre-processing

To visualise the steps in the different parts of the image processing a reference image has been chosen. The reference image is shown in Figure 4.4 at which three bubbles have been marked. The three bubbles are assumed to be approximately the same size. The reference image is further on referred to as the original image, I_O.

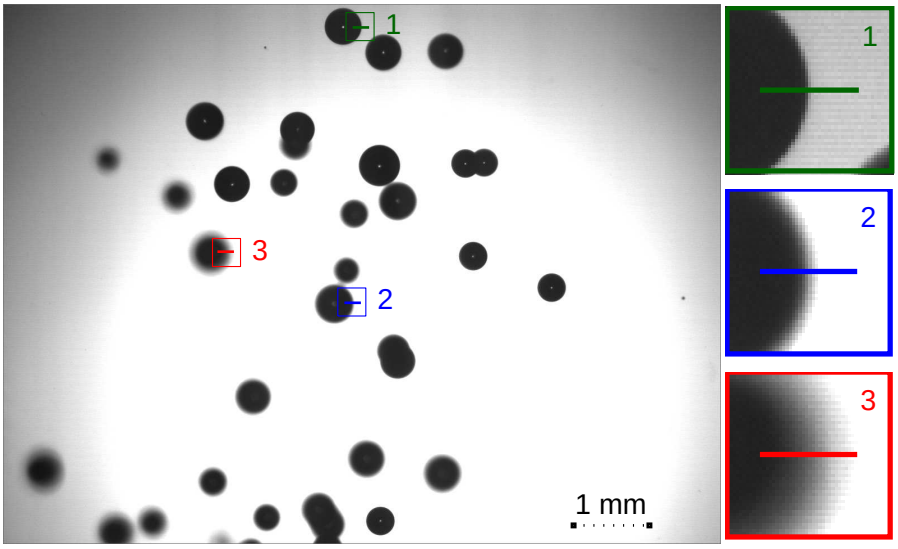

Figure 4.4: Reference image, I_O, with three reference bubbles marked.

The bubbles represent three levels of focus, which is seen on the sharpness of the bubble edge. Bubble 1 is completely in focus, bubble 2 is almost in focus and bubble 3 is out of focus. Line profiles along the marked lines are displaying the GS values and show the effect of the steps in the image processing as they are presented onwards in this section.

First step is to remove the noise and the background. This is done by use of Equation 4.1, where the noise image, I_N, is subtracted from both the original image, I_O, and background image, I_B. This is followed by a normalisation of the original in relation to the background. [Mischler, 2010]

$$I_F(x,y) = \frac{I_O(x,y) - I_N(x,y)}{I_B(x,y) - I_N(x,y)} \cdot 255 \quad [-] \tag{4.1}$$

Where:
$I_O(x,y)$ is the original image.
$I_B(x,y)$ is the background image, see Figure 4.3a.
$I_N(x,y)$ is the noise image, see Figure 4.3b.
$I_F(x,y)$ is the foreground image, see Figure 4.5.

Some of the pixels get a GS value above 255, since the I_O some places has a higher GS value than I_B. This happens in the darker area around the edge in the image. It has no influence on the bubble edge, since the bubble shadow always has a smaller GS value than the background. Pixel values above 255 are assigned a GS value of 255.

In Figure 4.5 the foreground image, I_F, is shown.

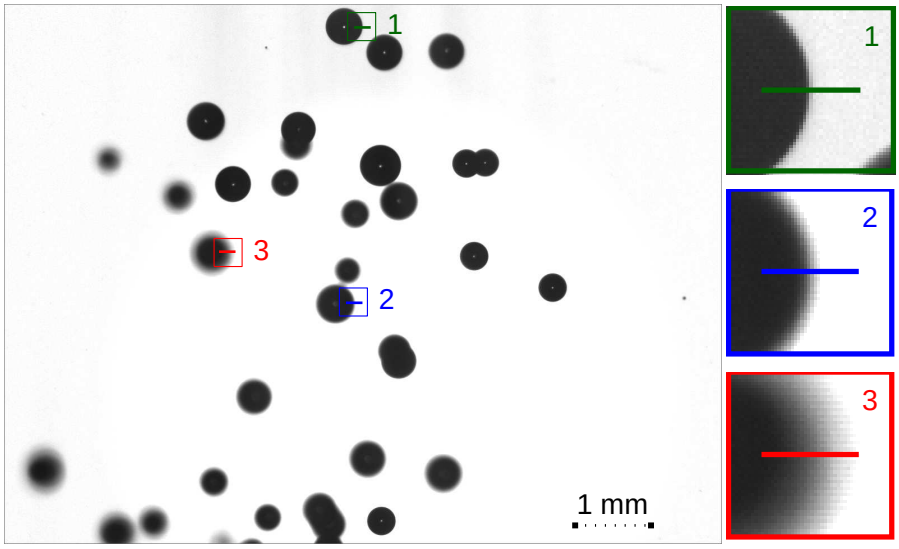

Figure 4.5: Foreground image, I_F, without background and noise.

The dark area around the edge of the original image has been eliminated, see Figure 4.4. Only a change in the background for bubble 1 is displayed in the sub images at Figure 4.5, whereas bubble 2 and 3 are in the spot of the light source. In the top part of the image some weak shadow casts are seen. The bubbles close to the spot of the light source cause some shadow cast, due to diffraction of the light. The casts do not appear in the background image, I_B, which makes them more visible, when removing the background from the original image, I_O.

To utilise the total GS range, the GS values are stretched to cover the entire GS range. By use of Equation 4.2 the GS values are stretched. Notice the GS values after this step is between 0 and 1.

$$I_S(x,y) = \frac{I_F(x,y) - I_{F,min}}{I_{F,max} - I_{F,min}} \quad [-] \tag{4.2}$$

Where:
$I_{F,min}$ is the minimum GS value in the image.
$I_{F,max}$ is the maximum GS value in the image.
$I_S(x,y)$ is the stretched image.

Furthermore the contrast in the image is enhanced by use of the intensifier operator shown in Equation 4.3 and in Figure 4.6. For GS values above 0.5, a higher value is applied. For GS values below 0.5 a lower GS value is applied. In both scenarios the operator is nonlinear for obtaining a higher contrast between the two ends of the GS range. [Chaira and Ray, 2010,p. 50]

$$
\begin{aligned}
(4.3) \qquad I_C(x,y) &= 2 \cdot [I_S(x,y)]^2 && \text{for } 0 \leq I_S(x,y) \leq 0.5 && [-] \\
&= 1 - 2 \cdot [1 - I_S(x,y)]^2 && \text{for } 0.5 < I_S(x,y) \leq 1 && [-]
\end{aligned}
$$

Where:
$I_C(x,y)$ is the contrast enhanced image.

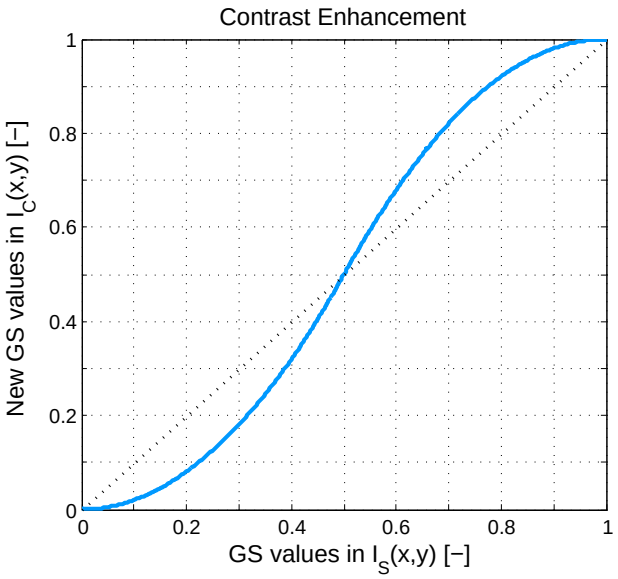

Figure 4.6: The intensifier operator used for contrast enhancement.

After the contrast enhancement the image is converted back to the 8-bit range, from 0 to 255.

The result of the two image processing steps, stretching and contrast enhancement, is shown in Figure 4.7.

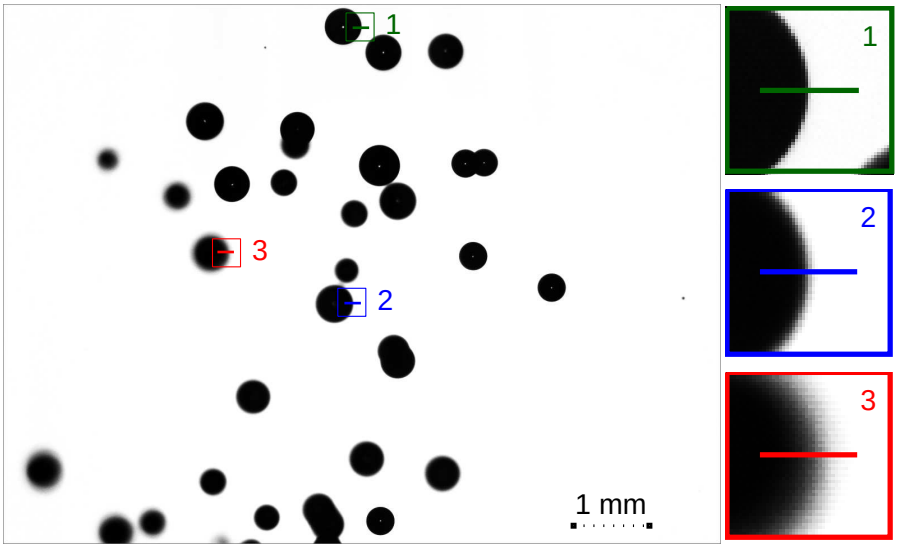

Figure 4.7: Contrast enhancement image, I_C.

The shadowing cast from the bubbles seen in Figure 4.5 are not visible anymore in Figure 4.7. It is visible in the background for bubble 1, if the two sub images are compared.

The change of the line profiles in relation to I_O as the three pre-processing steps are applied, are shown for the three bubbles in Figure 4.8.

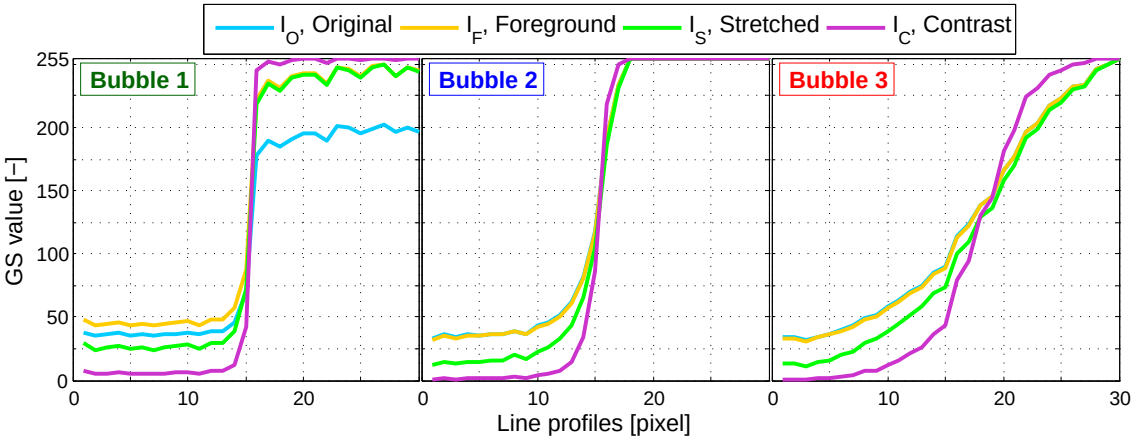

Figure 4.8: The influence on the bubble edges using the three pre-processing steps.

The removal of the background, as going from I_O to I_F, is only visible for bubble 1, since it is located outside the spot from the light source. The background for bubble 2 and 3 are entirely white and thereby no change occurs. When the image is stretched, I_S, a visible change occurs in the lower GS range for all three bubbles. When contrast enhancement is applied, I_C, the line profiles across the bubble edges cover the entire GS range. Furthermore the slope of the line profiles for bubble 2 and 3 are increased. This makes it easier to detect the edge of the bubbles in following processing steps. The influence on the following edge detection process has been tested for each of the pre-processing steps. The location of the bubble edges are not affected by the pre-processing.

4.3.3 Image Processing

The image processing, which is done in NI Vision, consists of the following steps:

- Edge detection
- Thresholding
- Binary morphology
- Calibration
- Particle detection
- Data logging

The edge detection, thresholding and binary morphology are described in this section. The calibration is described in Section D.2 in Calibration for IPI & TDIM - Appendix D. The extracted data for the detected bubbles are presented in section 4.4.

Edge Detection

Clear marking of the edge location is one of the requirements for the edge detection filters. This requires a narrow line along the edge with a high GS intensity compared with the surrounding pixels. The size of the intensity at the edge line should also indicate how sharp the edge of the bubble shadow contour is. This is to sort out the bubbles out of focus, which have a more blurred shadow contour in comparison with the bubbles in focus, and as result a lower intensity. The determination of the location of the bubble edges with a blurred shadow contour is more difficult and thereby the accuracy of the bubble size is reduced. From a visual inspection of the reference image, only bubble 1 and 2 should be found valid as bubbles in focus. Thereby the difference in between the GS intensity of the edges should be significant, when comparing the line profiles for bubble 1 and 2 with bubble 3.

Five different edge filters are available in NI Vision Assistant:

- Laplacian
- Differentiation
- Roberts
- Prewitt
- Sobel

They can be applied as a filter by use of a convolution kernel. The convolution kernel is normally a 3 times 3 structure, which change the GS value of each pixel in the image according to the surroundings pixels. The GS value is changed to a weighted sum of the original GS value and the GS values of the 8 surrounding pixels. The coefficients of the convolution kernel contain the applied weights, which can be negative or positive. The edge detection filters are highpass filters, which highlights significant variation in the GS values.

Laplacian highlights variation in the light intensity in all directions. A linear combination of the surrounding pixels are given as the new GS value.
Differentiation outlines the contour of the image, by finding the maximum intensity variation between the pixel and the three upper left neighbouring pixels. Thereby the kernel size is only 2 times 2.
Roberts highlights the details by looking at the intensity variation along the diagonal axis. It takes the absolute value of the maximum deviation between centre pixel value and the three upper left neighbouring pixels. Thereby the kernel size is only 2 times 2.
Prewitt extracts the outer contour of objects. It has 16 different kernels, which finds the gradient across the central pixel in different directions. The maximum gradient is set as the new GS pixel value.
Sobel is similar to Prewitt, but gives higher weights to the neighbouring pixels in the horisontal and vertical positions. Sobel is thereby good at extracting square contours in comparison to Prewitt, which works better with curved contours.

The five edge filters are tested on the reference image after it is pre-processed as described in Section 4.3.2, see Figure 4.7 and the I_C contrast line profiles in Figure 4.8. The line

profiles for the three reference bubbles are shown in Figure 4.9, where the influence of the five edge filters are displayed. Note the x-axes have been cropped 5 pixels in both ends, to enhance the difference between the edge filters.

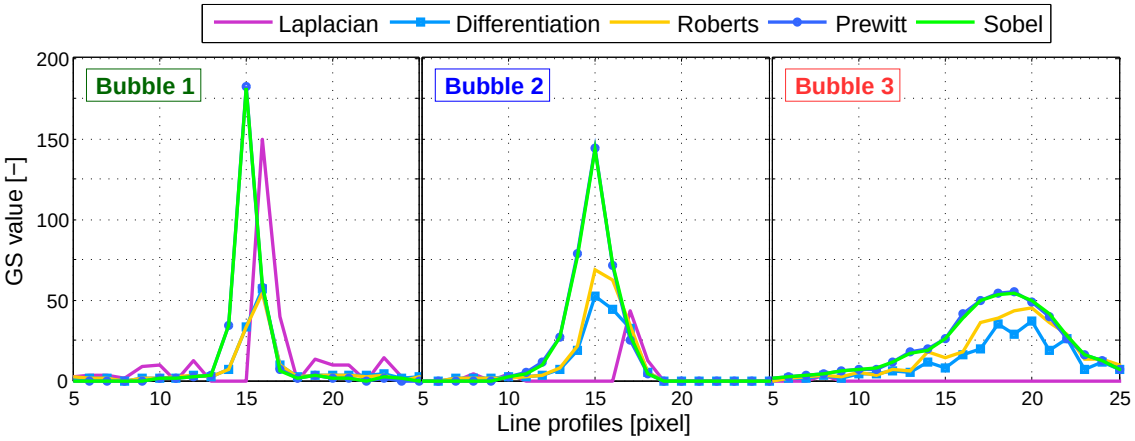

Figure 4.9: Line profiles showing the influence of the five edge filters on the three reference bubbles.

For bubble 1 Differentiation and Roberts follow each other and the same goes for Prewitt and Sobel. The peak is highest for Prewitt and Sobel, but Laplacian also marks the sharp bubble edge very well. However the location of the Laplacian peak is slightly shifted away from the bubble centre. It will cause the bubble to appear larger in size. All five edge filters marks the location of the edge precise with a narrow peak in the line profile.

For bubble 2 Prewitt and Sobel again mark the edge with a higher peak in comparison with the other edge filters. The peaks of Differentiation and Roberts are at the same height as for bubble 1.

When comparing all three bubbles the height of the peaks for Differentiation and Roberts does not change significant and thereby these are eliminated. The Laplacian filter is obvious best at a sharp edge, since the edge of bubble 3 is not detected. The Laplacian also seems to locate the edge further away from the bubble centre compared with the other edge filters in bubble 1 and 2. Thereby Laplacian is also eliminated. The difference between Prewitt and Sobel is not visible at any of the three bubbles. If the line profiles are made across the edges with an angle of e.g. 45° in relation to the horisontal direction, a difference will probably have been visible. Consequently, Prewitt is chosen, due to the advantages when applied to curved edges.

Thresholding

Thresholding is used to divide the image into two parts, a background component and particle component. By use of the GS histogram of the image a threshold value is set. The pixels with a GS value above are set as particles with a value of 1, while the others are set as background with a value of 0. By use of the threshold the edges detected in the previous step can be marked. The threshold value can also be used to sort out the bubbles which are out of focus, since the edge peaks of these are not that high. Different kinds of threshold tools are available, but due to low variation of the light intensity in

the background after pre-processing, a global manual threshold can be used. Threshold values of 140 and 80 have been tested.

Bubble 2 is thereby used as the lowest acceptable standard for bubbles in focus for the threshold value of 140, see Figure 4.9. For the threshold value at 80 the in focus criteria is further decreased, but bubble 3 is however still not found valid. Both threshold values have been used for the image processing of an image sample of 2000 images to see the impact on the final result.

For the threshold of 140, 3240 bubbles are detected, while for a threshold of 80 five times more bubbles are detected, hereof 16,297 bubbles. The mean bubble diameter is lowered with 1 μm, when going from 140 to 80. However the standard deviation is increased with a lower threshold value applied. But since the number of bubbles detected is higher for a threshold of 80, the confidence interval for the true mean diameter is halved compared with a threshold of 140. Based on the states above a Threshold of 80 is chosen.

Binary Morphology

The last part of the image processing is a number of Binary Morphology operations. These are used to improve the information on the binary image of the detected edges. Only the valid bubbles should be left and ready for particle analysis. The first operator applied files out holes of closed objects. The second operator removes the objects in contact with the border of the image. A Heywood circularity criteria is used for removing leftovers of none closed object, since these are far from circular. Heywood, H, is given as the Perimeter, P, of the bubble divided by the circumference of a circle with the same area, A, see Equation 4.4.

$$H = \frac{P}{2\sqrt{\pi A}} \quad [-] \tag{4.4}$$

The Heywood filter is also used to remove overlapping bubbles. The concentration of bubbles in the image causes a low amount of bubbles to overlap. It is chosen not to take the overlapping bubbles into consideration and thereby avoiding an implementation of a process to separate them. The last binary morphology removes smaller particles, which are either very small bubbles or other small particles in the water. The small particles can also be leftovers of bubble edges which are not entirely included by the thresholding.

Figure 4.10a shows the reference image including the three bubbles after thresholding, while Figure 4.10b shows the reference image after binary morphology. The pixels in both figures have been inversed to improve the presentation of the edges. The holes of the closed edge contours are filled from Figure 4.10a to 4.10b and the rest has been removed.

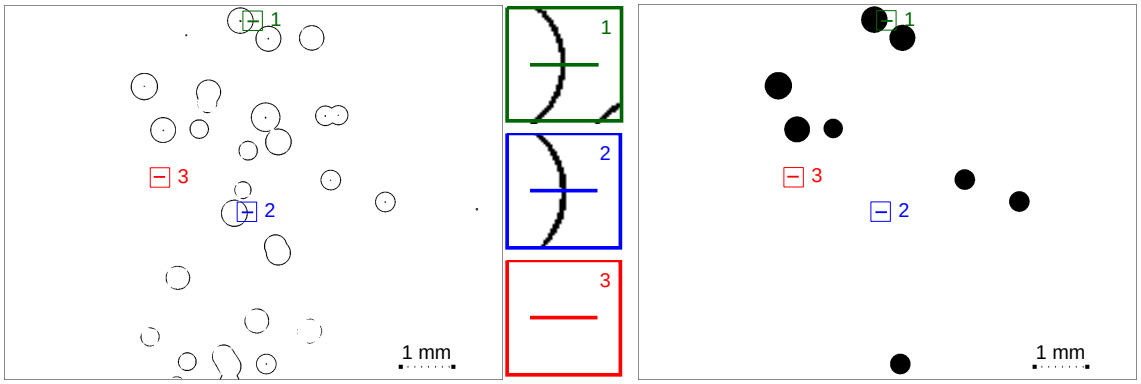

(a) Threshold image and the three reference bubbles.

(b) Threshold image after binary morphology operations.

Figure 4.10: Presentation of the effect of the binary morphology operations by a before and after image.

The overlapping bubble pairs and the particles in contact with the border of the image have been neglected as expected. Also the small particles and none closed edge contours have been removed.

In Figure 4.10a the edge of bubble 1 and 2 are clearly captured by the threshold, while bubble 3 is not detected as expected. However bubble 2 has been neglected in Figure 4.10b due to the binary operations. The bubble north-east of bubble 2 impacts the edge contour as it can be seen in Figure 4.7. Thereby the edge gradient at this location is not big enough, which causes a hole in edge contour after thresholding.

Calibration

The calibration performed in NI Vision and equipped in Figure 4.10 is further outlined in Calibration for IPI & TDIM - Appendix D. The resolution becomes 7.46×7.40 μm resulting in a FOV of 9.570×7.121 mm. An indication of a 1 mm scale is added to Figure 4.10 and to the prior figures for guidance.

4.4 Results

The detected bubbles from NI Vision and corresponding extracted data are presented.

4.4.1 Data Selection and Processing

All bubbles are utilised in the processing since no bubbles deviates severely from the bubble size distribution. The distribution will consist of 85 bins where each represents a diameter range of 10 μm. Each bar representing a bin is based on it centre value.

The diameter extracted from the detected bubbles is the horisontal width. This is because IPI results in the same horisontal diameter. Simultaneously the influence of potential present bubbles tracks in the vertical direction is avoided.

4.4.2 Bubble Size

Figure 4.11 and 4.12 show two bubble size distributions for the two samples, TDIM 1 and TDIM 2, at the conditions given in Table 4.2. The characteristic diameters are calculated based on Equation 3.14 from Interferometric Particle Imaging for Bubble Measurement - Chapter 3.

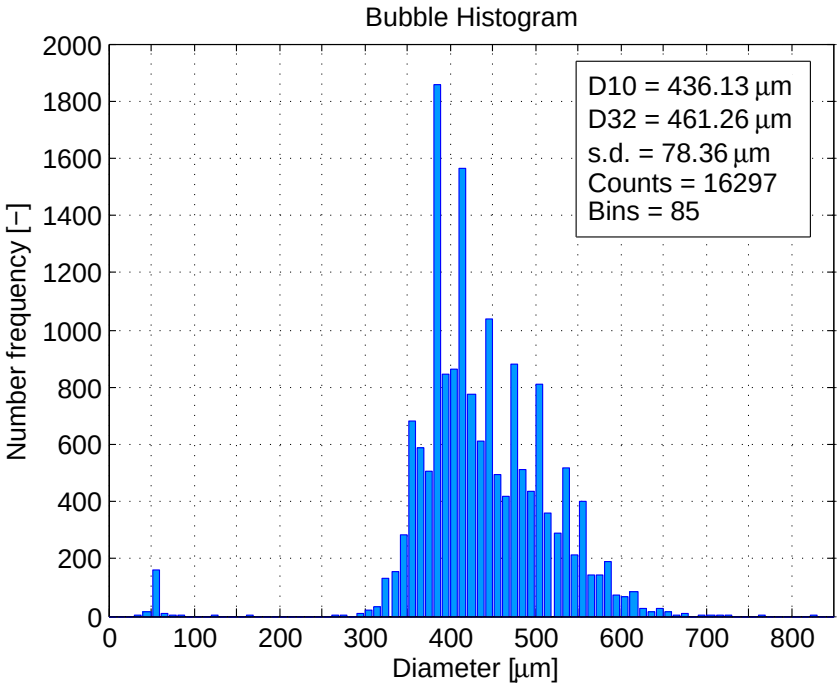

Figure 4.11: Bubble size distribution with the parameters given for TDIM 1 in Table 4.2.

Though both TDIM 1 and TDIM 2 have both analysed 2000 images, there appear to be a disagreement between the numbers of detected bubbles in the bubble sample size. TDIM 1 has detected 26 % more bubbles in comparison with TDIM 2. Consequently, TDIM2 shows a higher standard deviation. The cause can be related to the higher pressure specified in Table 4.2 for TDIM2. A higher number of bubbles may have been generated causing a higher number of bubble overlaps in the 2000 images and thereof a lower number of extracted bubbles for the bubble size distribution. A higher pressure may also have caused a different flow pattern of the rising bubbles either out of the FOV or away from the focal plane. Another reason may be related to that the setup has not been placed in the exact position for TDIM in relation to TDIM 1, since the IPI measurements are conducted in between. Thereby the FOV may not have been the same for both TDIM 1 and TDIM 2.

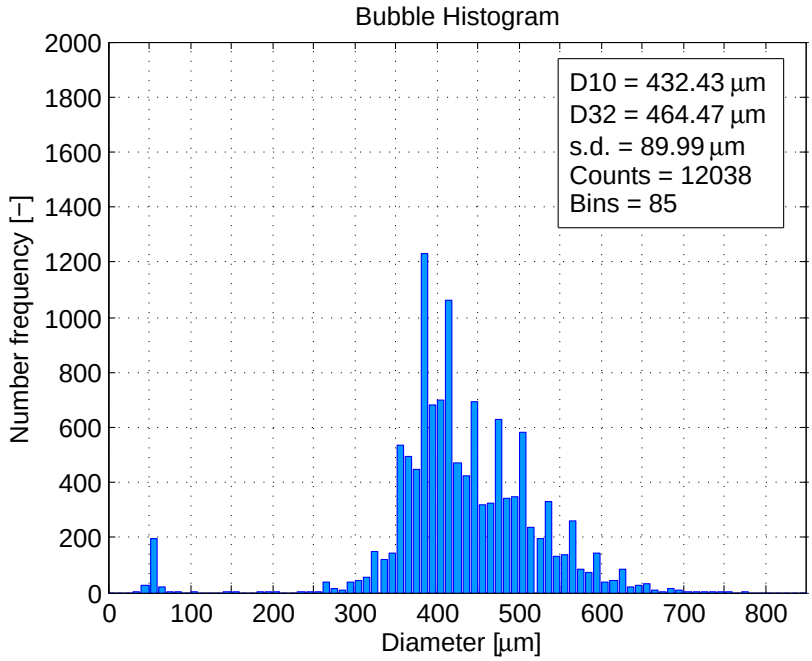

Figure 4.12: Bubble size distribution with the parameters given for TDIM 2 in Table 4.2.

For both TDIM 1 and TDIM 2, there appear to be an irregularity in the size distribution represented by high peaks in the number frequency with approximately 20 μm in between. This trend can be related to some of the steps in the performed digital image processing. A group of small bubbles is present in the size distribution for both TDIM 1 and TDIM 2 at 60 μm. They are assumed to be either undesirable particles in the water or leftovers of from the digital image processing, which has not been removed.

4.4.3 Volume Size

Figure 4.13 shows the volume size distribution based on the extracted diameters for TDIM 1 in Figure 4.11.

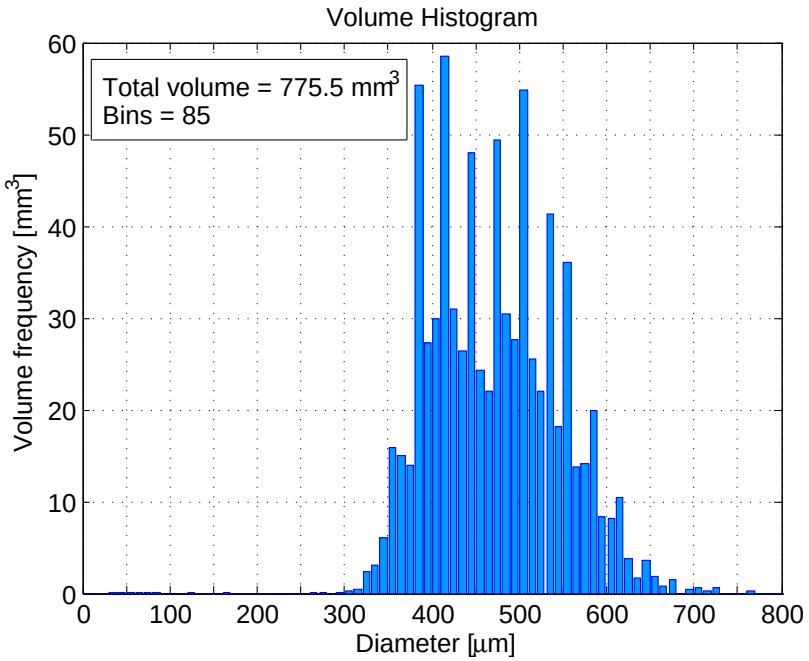

Figure 4.13: Volume size distribution as a function of the diameters in Figure 4.11.

TDIM 1 is shown due to the higher number of present bubbles and lower standard deviation. Hence again the volume is calculated by considering the bubbles to be spherical. The total volume of the bubbles is also specified in Figure 4.13.

Comparison & Validation 5

The results from the two measurements methods, Interferometric Particle Imaging (IPI) and Telecentric Direct Image Method (TDIM) presented in the two previous chapters are to be compared in this chapter. The two experiments utilising TDIM and IPI are carried out sequential, and thereby the conditions of the bubble flow are assumed to be equal for both experiments. A second TDIM experiment is carried out after the IPI experiment to check for inconsistency in the experimental conditions. The results of the two TDIM experiments are found similar, for which only the results for the first TDIM experiment are included in the comparison.

5.1 Comparison of IPI and TDIM results

The measured diameters from IPI, presented in Section 3.5, and from TDIM, presented in Section 4.4, are compared in Figure 5.1. The results are shown with a normalised number frequency of the bubble diameter distribution. The cumulative frequency distribution is also marked with red lines for both frequency distributions.

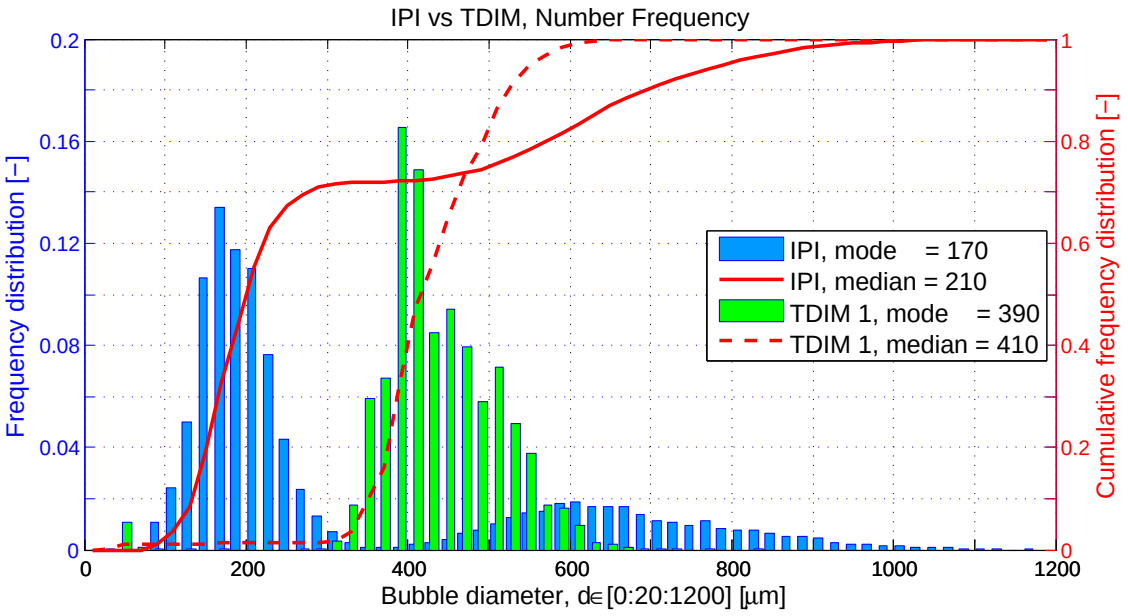

Figure 5.1: Comparison of the number frequency for the diameters from the IPI and TDIM sample.

The distributions of the diameters are far from similar for the two methods. The IPI is distributed over a larger range of bubble diameters with a mode value of 170 μm. IPI can be divided into two bubble diameter ranges. The first range has a high frequency of bubbles around 180 μm and by surpassing this range the cumulative frequency covers 72 %. The rest of the cumulative frequency is distributed from 360 μm up to 1200 μm with the highest frequency at 610 μm. Hence the graph representing the cumulative frequency distribution appears very irregular. By comparing to the results of the pre-test of the experimental setup in Design & Test of Experimental Setup for Rising Bubbles - Appendix B, the bubble distribution is found collected around a single peak using a normal DIM with a microscope camera. Thereby the IPI results are considered not to be probable.

The diameters from TDIM are concentrated close around the mode value of 390 μm. As a result the cumulative frequency distribution appear much more regular when comparing with IPI and increases from 0 to 1 over a much shorter diameter range. The TDIM distribution have a small diameter frequency presented at 50 μm, which is considered to be leftovers from the digital image processing in Section 4.3.

During the conduction of the two experiments no visible change of the bubble size is observed. It leads to the suspicion that one of the measurement methods must have failed, since there is no agreement between the two diameter distributions in Figure 5.1. Whereof the suspicion is mainly related to the results of IPI.

A reason for the difference between the bubble distributions could be due to a misalignment of the measurement regions in the rising bubble column. This possible scenario is investigated in the following section.

5.2 Investigation of ROI and FOV

As the bubble size is assumed not to differ from one measurement method to the other, the reason to the various results might be related to the Region of Interest (ROI) for IPI and Field of View (FOV) for TDIM. If ROI and FOV do not cover the entire column width of the rising bubbles, some bubbles might be detected when using one method and not the other. For this reason an inspection of the ROI and FOV is conducted.

Since the bubbles are rising upward in the y-direction those bubbles passing through the ROI will also pass through the FOV. Hence the position and width in the x-direction become more important when the same bubbles are to be detected in both ROI and FOV.

The situation is sketched and visualised in Figure 5.2. In Figure 5.2a is shown how the ROI and FOV interfere with each other through the plexiglass column and meet at the focal plane. In order to compare them their dimensions will have to be transformed from pixels to mm as shown in Calibration for IPI & TDIM - Appendix D. After dewarping the calibration image for IPI, the FOV for TDIM can be placed in the same image as ROI. The locations of ROI and FOV are shown in Figure 5.2b.

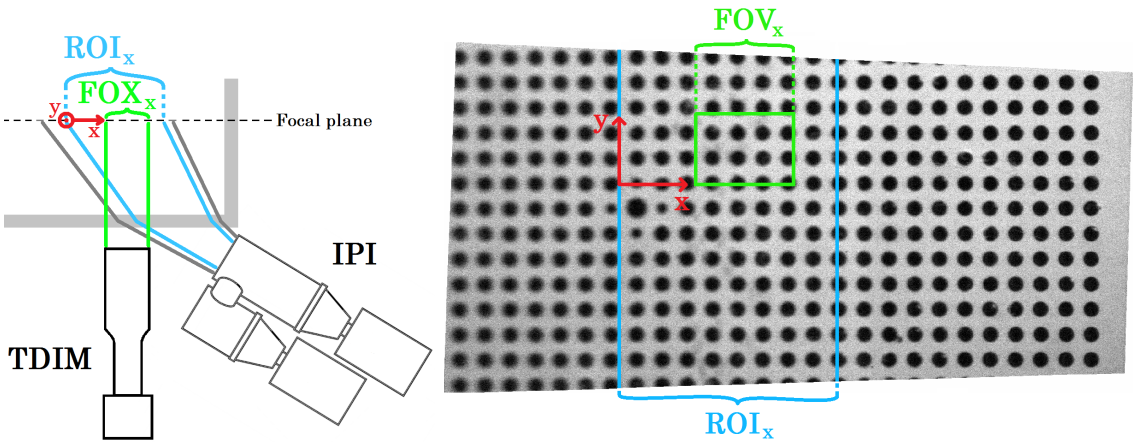

(a) Location of FOV and ROI.

(b) Location at focal plane after dewarping.

Figure 5.2: A sketch showing the two applied methods IPI and TDIM and how ROI and FOV are located relative to each other.

Both the camera for IPI and TDIM are located where the centre of the rising bubble column is believed to be located. Since the water within the column are considered steady the FOV is located straight above the cannula, while the ROI is located to be in the centre of the acquired image before dewarping.

As shown in Figure 5.2b the widths in the x-direction, ROI$_x$ and FOV$_x$, are not the same. The number of bubbles passing through these widths will be investigated to see whether the wider ROI$_x$ sees bubbles which are not detected by the narrower FOV$_x$. Figure 5.3 shows the frequency distribution of bubbles along the joined axes of FOV$_x$ for TDIM according to ROI$_x$ for IPI. The coordinate origin is display in Figure 5.2.

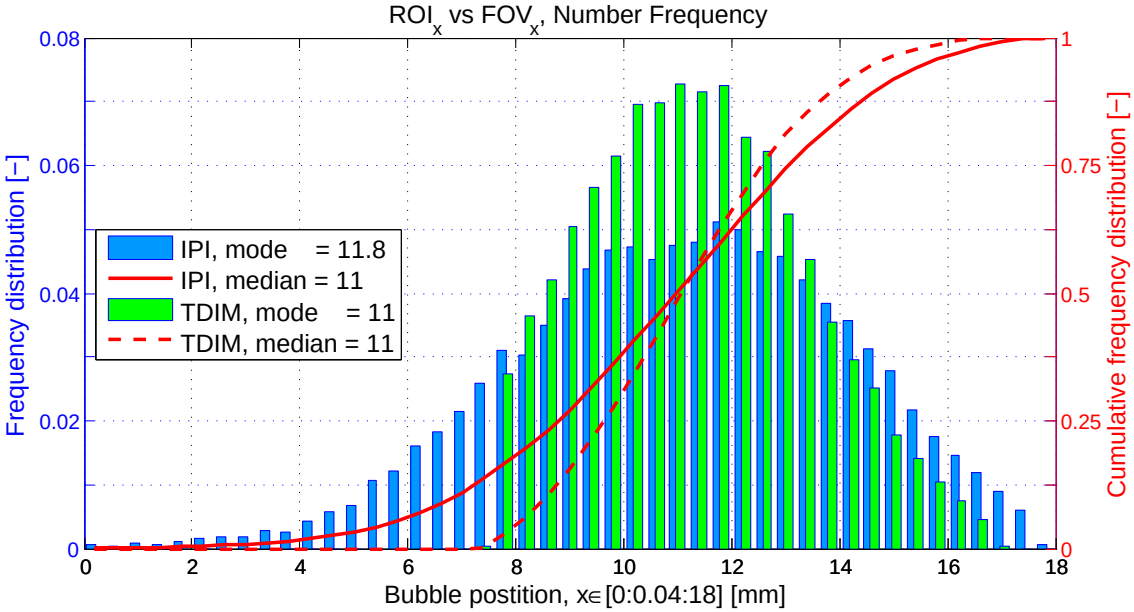

Figure 5.3: Comparison of the number frequency for the horisontal position from the IPI and TDIM sample.

The mode is approximately the same for IPI and TDIM indicating that the location of the highest frequency range of generated bubbles has been in the same position when conducting the two measurements. In addition there tends to be a skewness of the number of bubbles toward right, visible for IPI. The median is the same for the cumulative frequency but not comparable since ROI_x is bigger than FOV_x. The comparison is possible when setting ROI_x equal to FOV_x where only detected bubbles for both methods are shown, see Figure 5.4.

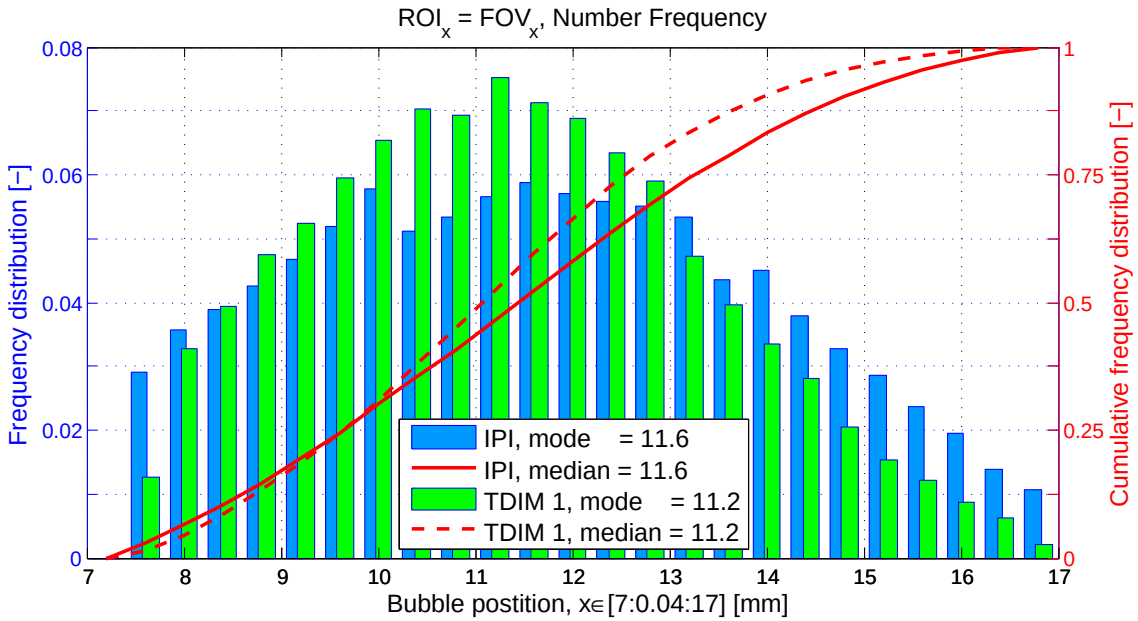

Figure 5.4: Comparison of the number frequency for the corresponding horisontal location for the IPI and TDIM sample.

The same trend appears for IPI and TDIM in Figure 5.4. The cumulative frequency distributions are comparable and follow each other until reaching the right side of the figure, where a higher number of bubbles have been detected by IPI. But looking to the left where the cumulative frequency is very similar it is likely that the frequency distribution for FOV_x will continue beyond the x-axis in the same manner as for ROI_x shown in Figure 5.3. In principle these bubbles can be of any size and might have had a significant impact on the bubble size distribution. Nevertheless both methods appear to be looking at the same area of the rising bubble column but are showing inconsistent results as shown in Figure 5.1. Consequently both TDIM and IPI are further validated in the following two sections, to clarify which has failed.

5.3 Validation of TDIM

For the validation of TDIM polyamid particles are added to the water column without any rising bubbles. These particles work as size reference and can be used to estimate how reliable TDIM is. The same setup and settings as in Figure 4.1 and Table 4.1 are utilised. The only addition to the setup is a green 532 nm colour filter in front of lens to decrease the intensity of the light. A green filter is chosen based on the spectral response

of the CCD sensor shown in Figure G.5 in TDIM Principles & Equipment - Appendix G. The polyamid particles has a mean diameter of 50 μm with a standard deviation of 20 μm and a shape which is not spherical but round [Dantec Dynamics, 2014a].

The execution of the measurements are conducted with the same conditions and settings as given in Table 4.2 with regards to 4 fps, 16 μs for exposure time and 2000 images. The digital image processing is quite similar to the one applied in Section 4.3. Average background and noise images are made and subtracted from the images with the polyamid particles. The GS values are stretched followed by contrast enhancement. Prewitt edge detection is utilised for edge detection with a threshold of 100. Since the polyamid particles are not moving in a vertical direction, the diameters are estimated based on the extracted area by assuming a circular shape of the particles.

The measurement counts 12,286 of the polyamid particles. It results in a mean diameter, D10, of 58.5 μm with a standard deviation of 11.5 μm. The Sauter mean diameter, D32, is 62.8 μm. Figure 5.5 shows the normalised size distribution of the polyamid particles.

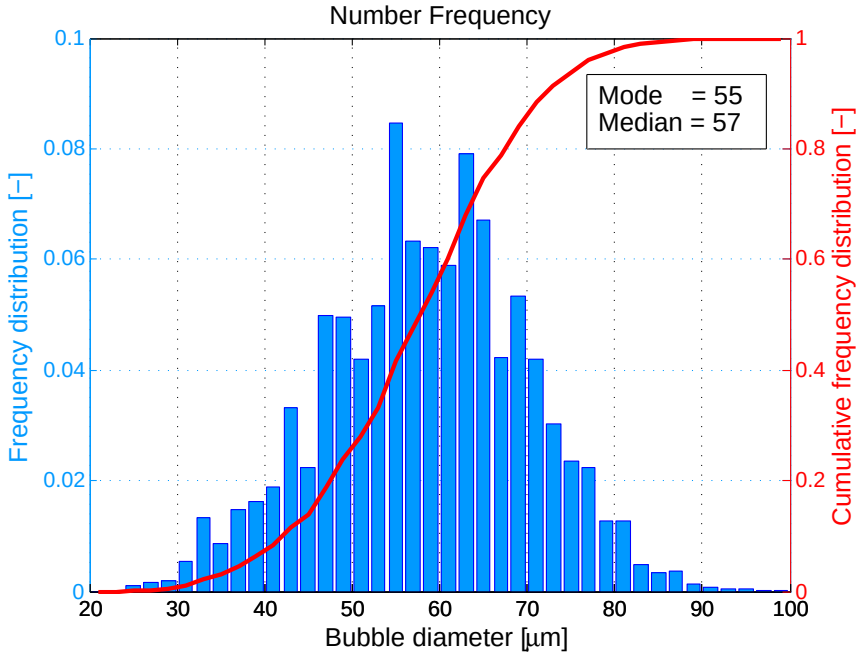

Figure 5.5: Normalised size distribution of polyamid particles by TDIM.

The result in Figure 5.5 is very consistent with the specified dimensions of the polyamid particles. The variation of 7 μm between the median and specified diameter of 50 μm could be removed by further improvement of the digital image processing. It must be noticed that the polyamid particles are considerably smaller in comparison with the rising bubbles increasing the importance of the digital image processing. According to the calibration in Calibration for IPI & TDIM - Appendix D, each pixel represents approximately 7.50×7.50 μm. Due the small size of the polyamid particles the spatial resolution has a significant impact on the size measurement. This gives a relative high uncertainty of the size distribution.

Considering the reliability based on the size distribution of the polyamid particles, TDIM

is applied to indicate the size distribution of the bubbles along FOV_x together with the number frequency. Together with the bubble diameter the concentration for the bubble sizes is displayed in Figure 5.6.

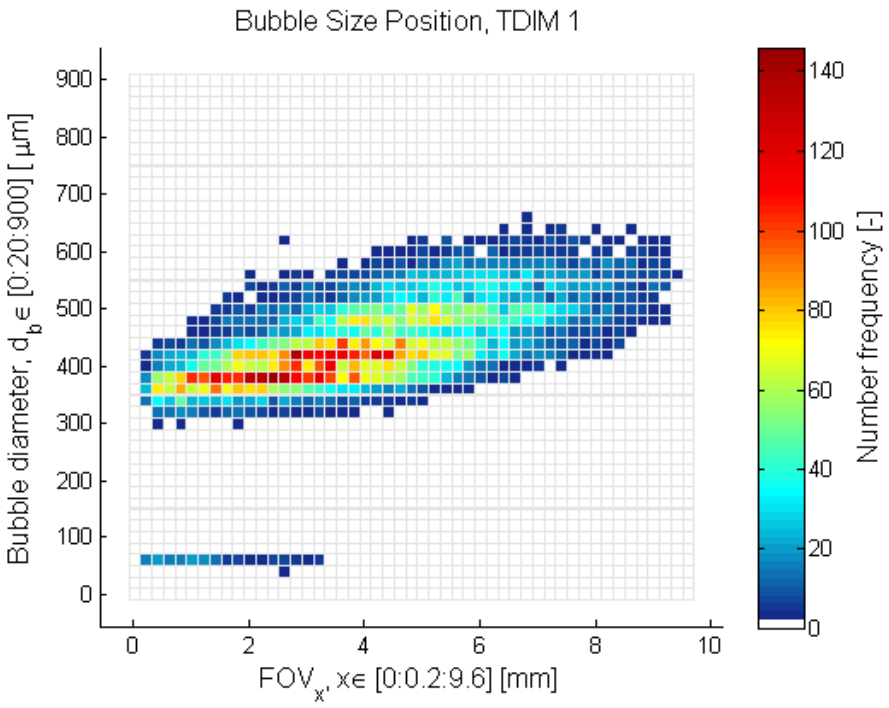

Figure 5.6: Bubble size position in FOV_x for TDIM.

There tends to be a skewness of the number of detected bubbles but also of the size along FOV_x. Smaller bubbles are high in numbers to the left in FOV_x, while fewer but bigger bubbles appear to the right of FOV_x. The cause can be due to the unsymmetrical shape of the cannula shown in Figure B.2a in Design & Test of Experimental Setup for Rising Bubbles - Appendix B.

5.4 Validation of IPI

The validation of the IPI result is made based on the associated feature of Particle Tracking Velocimetry (PTV). The velocity will be set in relation to the location of the two bubble diameter groups within the ROI_x. This will also verify if IPI agrees with the validation of TDIM that fewer but bigger bubbles are located further to the right of the image, while more bubbles but smaller in size are located to the left. Additionally, considerations are made whether there are spherical bubbles in the flow.

5.4.1 Location of Bubble Groups

The bubble diameters for IPI are divided into two groups by use of the IPI frequency distribution in Figure 5.1. The threshold is set as the minimum value between the two peaks, $d_{threshold} = 360$. Big bubbles, n_b, above and small bubbles below, n_s. Figure 5.7 shows the histogram of the two bubble groups regarding the position within the ROI_x.

To show the relation between the number of big bubbles, n_b, and small bubbles, n_s, the percentage relation $r = n_b/(n_b + n_s) \times 100$ is marked for each interval at the figure. If r is higher than 50 %, there is a higher number of big bubbles compared to the number of small bubbles.

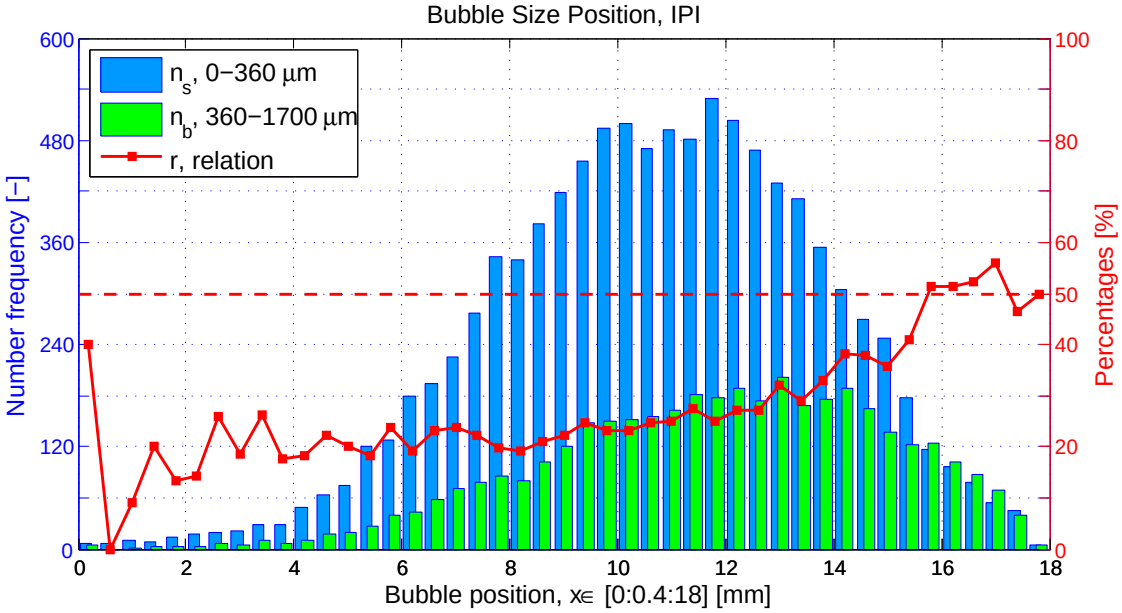

Figure 5.7: Horisontal position for the small and big bubbles for IPI.

Like for TDIM in Figure 5.6 there tends to be a tendency of a high number of bigger bubbles located to the right. The percentage relation visualises it by increasing toward the right and surpassing 50 %.

5.4.2 Velocity Distribution

If the two diameter groups are spread as shown in Figure 5.7 and with a change of the percentage relation along the x-direction, then this tendency should be visible when looking at the velocity results of PTV. Both the velocity V in the y-direction (vertical) and the velocity U in the x-direction (horisontal) are investigated to see if there is any indications of two distinguished bubble sizes. The frequency distributions for the two velocities, V and U, are shown in Figure 5.8 and 5.9, respectively.

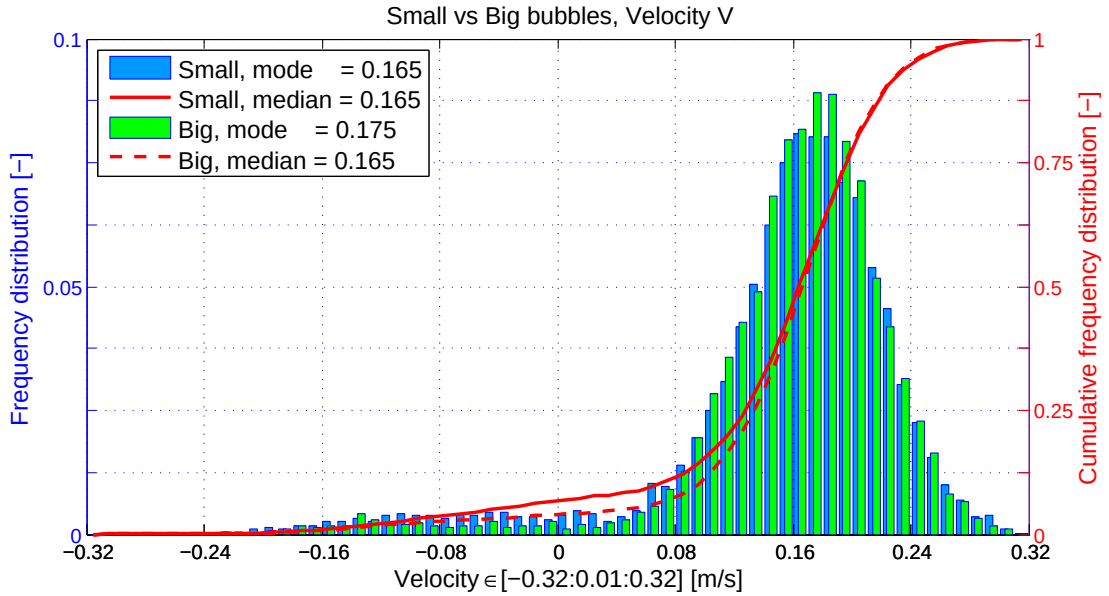

Figure 5.8: Frequency distribution for velocity V (y-direction).

The cumulative frequency distributions of the velocity for the two bubble groups are closely related. Additionally, the cumulative frequency distributions specify both the same median, meaning that no displacement of the velocity occurs due to the size difference in D10. According to Figure A.4 in Vertical Bubble Flow - Appendix A, a single rising bubble in steady water with D10s = 189 μm may have a velocity of 0.023 m/s and D10b = 669 μm a velocity of 0.111 m/s. These velocities are only valid for single rising bubbles while here the bubbles are rising in a swarm which will increase the velocity V of the rising bubbles. This state that the two distinguish bubble diameter groups should have displayed a difference in the velocity frequency distribution in Figure 5.8.

Regarding the velocity U in Figure 5.9 then it is slightly moved toward the left.

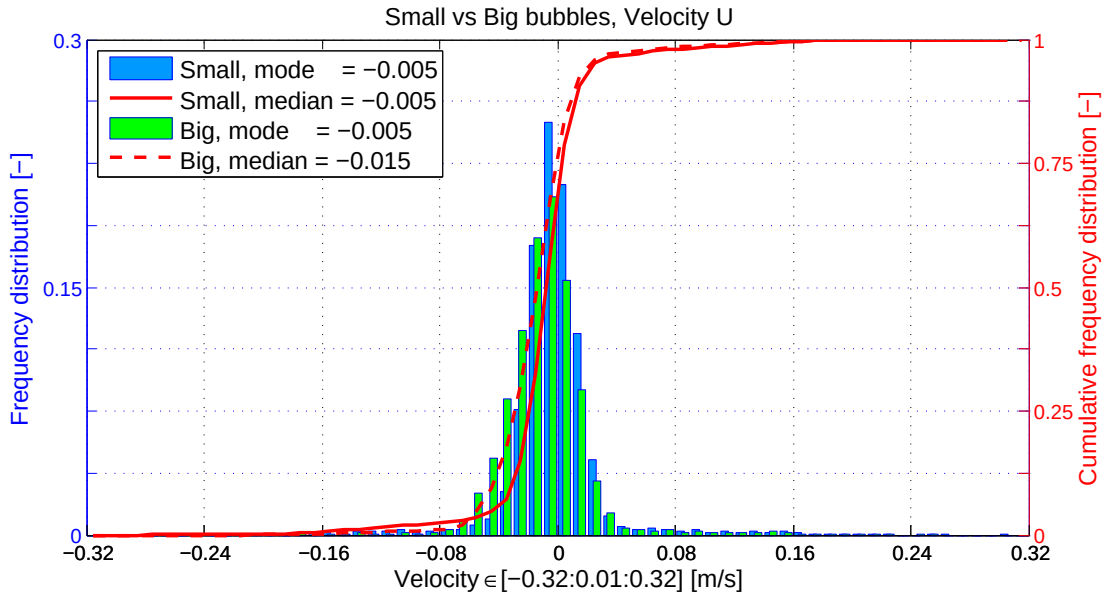

Figure 5.9: Frequency distribution for velocity U (x-direction).

A difference in the U velocity for the two bubble groups may also be a possibility, since smaller bubbles tend to be more affected by the sideways movement of the surrounding water generated by the rising bubble column. This scenario is not detected by the U velocity measurement.

None of the two velocity distributions shows an indication of existence of two distinguish bubble sizes. For that reason, the IPI bubble size measurements are not found valid.

5.4.3 Circularity of Bubbles

It is assumed when using IPI, that the bubbles are spherical. In this connection the TDIM results are considered, which are found reliable in Section 5.3. The sphericity cannot truly be tested, since only 2D dimensions are available from the TDIM results and consequently the circularity can be found instead.

Heywood Circularity method is utilised for finding the circularity. The Heywood factor is found by NI Vision for every detected bubble. If it is equal to 1, the bubble shadow is perfectly circular. The Heywood factor is defined in Equation 4.4 in Telecentric Direct Image Method for Bubble Measurement - Chapter 4.

From a bubble sample of 2000 images for TDIM, the necessary data is extracted in NI Vision. For Heywood is obtained a mean value of 1.0052 with a standard deviation of 0.0051. This is considered to be a reliable result, which can support the assumption of spherical bubbles. The circularity depends on the extracted bubble contour from the image processing. The bubble contour can be affected by the exposure time, as described in Section 4.2 in Telecentric Direct Image Method for Bubble Measurement - Chapter 4.

The assumption of spherical bubbles is further enhanced by calculating the Reynolds number and Eötvös number, see Section A.1 in Vertical Bubble Flow - Appendix A. By utilising the mean bubble diameter for TDIM in Figure 5.1 and the mean vertical rising velocity, V, from IPI in Figure 5.8 the Reynolds number and Eötvös number are calculated to be 0.0674 and 55.96. Looking at the shape map of deformed bubbles in Figure A.1b in Vertical Bubble Flow - Appendix A, then the representative bubble is located in the spherical region. Still this must be considered with caution since the velocity is likely to be a result of a swarm of bubbles and the shape map represents single rising bubble conditions.

5.5 Trouble Shooting with Dantec Dynamics

Based on the questionable results from the IPI measurements contact has been made to the support department at Dantec Dynamics for questioning. The communication leads to that the applied IPI manual *FlowMap Particle Sizer - Installation & User's guide* supplied by Dantec Dynamics contains misleading information [Dantec Dynamics, 2003]. It mainly regards settings of the optical setup. [Andersen, 2014]

Figure 5.10 shows a clipping from the manual, which misleads the configuration of the IPI setup.

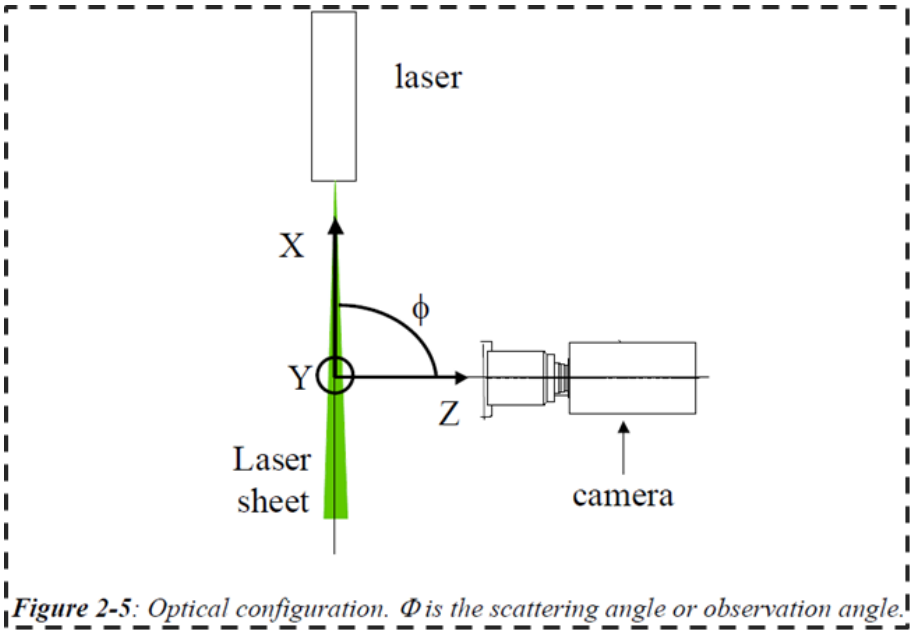

Figure 5.10: Clipping from the applied manual for the IPI setup. [Dantec Dynamics, 2003]

In the manual the scattering angle and the observation angle are considered as the same angle and represented by the same nomenclature, see the caption in the clipping in Figure 5.10. The clipping informs that the observation angle is applied for the camera position relative to the position of the laser. Furthermore, the manual suggests a scattering angle of 45° for a relative refractive index of 0.75. When the scattering angle and observation angle are defined as equal, it leads to the assumption that the cameras may be placed at 45° relative to laser position. However, the scattering angle starts at 0° opposite to the position of the laser. This results in an observation angle of 135° relative to the laser sheet, for a scattering angle of 45°. Thereby the position of the cameras should be change in order to capture the usable fringe pattern for IPI processing by FMPS.

This information is granted six days before the submission date of this report. Consequently, there is no time to perform new IPI measurements with a new observation angle and subsequent data analysis. These measurements are necessary in order to perform a reasoned comparison between IPI and TDIM.

5.6 Pros and Cons of IPI and TDIM

On the basis of the comparison and validation for IPI and TDIM in the prior sections and the experience obtained working with the two methods, a number of pros and cons can be stated for each of the two methods. IPI has the advantage of being applicable for various particle sizes over a large area. In addition, there is no major limitations regarding distances since the waist of the laser sheet can be adjusted without moving the laser, so can the focal plane without moving the cameras. A downside of IPI is the complexity of the setup. It includes many types of parameters which require a deep knowledge of the system, along with the additional adjustments of the setup to obtain reliable results.

This is unlike TDIM which is a much simpler system and requires no additional adjustments. It is however limited by the fixed focal length of the telecentric lens and its dependency of aligned background light. Moreover, a prior knowledge of the particle size is necessary to design the system according to its area of application. It regards camera resolution, magnification, size of FOV and working distance.

Regarding the measurement accuracy, then it looks promising for TDIM when considering the performed validation measurements of polyamid particles. Still there is room for improvements in terms of light setting and image processing to enhance the precision. For IPI, it is necessary to conduct new measurements before any indication of its precision can be specified. Overall, TDIM is estimated as a both reliable and straightforward approach which minimises the number of potential faults in the setup.

Conclusion 6

The increased application of Computational Fluid Dynamics for two-phase flow analysis has led to an increasing demand for more accurate measurement techniques. It especially concerns detailed information of particle characteristics inside the flow, which is not entirely available when performing computational analysis. The limitations become particularly evident when dealing with highly dense and unsteady flows, whereof many computational problems remain unsolved. By utilising in-line measurements an instantaneous knowledge of such flows can be given.

An estimation is desired of the size distribution of vertically rising bubbles in stagnant water. Various kinds of measurement methods are feasible for estimating the size distribution, all of various prices and performances. Among them, Interferometric Particle Imaging (IPI) is considered to be a highly accurate, slow and costly method. As an inexpensive and simpler alternative Telecentric Direct Image Method (TDIM) is utilised, which is based on the principle of shadow imaging.

A system from Dantec Dynamics is applied for the IPI. A Nd:YAG laser is making a parallel polarised laser sheet through a water column containing rising bubbles. A double camera mount is located 35° relative to the location of the laser to capture the light scattered from the bubbles. The interference of the scattered light is used to determine the individual bubble diameter. The associated FlowMap Particle Sizer software is customised for analysis of the acquired fringe pattern images. The bubble size distribution turns out unexpectedly as bimodal consisting of two distinct categories, one of small bubbles with a mean diameter of 189.31 μm and one of big bubbles with 669.34 μm. The total mean is 323.59 μm for the entire size distribution with a standard deviation of 230.5 μm. The failed result of IPI is due to misleading information from the applied *FlowMap Particle Sizer - Installation & User's guide* manual.

The setup for TDIM makes use of a white LED for background light and the advantage of a telecentric lens as optic. The exposure time is set to 16 μs to make the bubble move the shortest distance during acquisition. The images are treated for spotlight effect and noise followed by contrast enhancement and adjusting grey scale range. Digital image processing is performed with NI Vision, where Prewitt edge detection is found most feasible. A global threshold is chosen to sort out defocused bubbles. The size distribution is gathered around a mean diameter of 436.13 μm with a standard deviation of 78.36 μm. A small group of 60 μm bubbles are detected, but assumed to be leftovers for the digital image processing.

By comparing the frequency distribution of the bubble diameter for both methods it is clear that the results are far from similar. IPI is covering over a larger range of bubble diameters whereas TDIM is concentrated around its mean. The wider Region of Interest (ROI) for IPI and the narrower Field of View (FOV) for TDIM are investigated whether some bubbles are present in one and not the other. The mode of the number frequency for IPI and TDIM indicates that the highest frequency range of generated bubbles has been covered by both ROI and FOV. Still the wider ROI for IPI detects bubbles not covered by the narrower FOV for TDIM.

Round polyamid particles with a mean diameter of 50 μm and a standard deviation of 20 μm are added to the water to verify the reliability of TDIM. The measured mean diameter becomes 58.5 μm with a standard deviation of 11.5 μm. It is consistent with the specified dimensions of the polyamid particles and thus verifies the reliability of TDIM.

The associated feature of Particle Tracking Velocimetry (PTV) is applied to verify the reliability of IPI. In the first place the two distinct categories of bubble sizes are located within ROI. It turns out that the percentage relation between them increases as going from left to right in ROI, indicating that more bigger bubbles are present to the right. Considering this, a tendency should be visible when looking at the PTV velocity measurements. The cumulative frequency of the vertical velocity for both bubble categories are closely related and shows no indication of two distinct categories of bubbles which are not equally distributed in ROI. This leads to doubts regarding the reliability of IPI.

The measurement for TDIM is found reliable based on the verification and the consistency with the expected results. The IPI measurement is far from similar to TDIM and the verification of IPI measurements does not verify the presence of two distinct groups of bubble sizes. The IPI measurements are found unreliable, which indicates a fallible configuration.

A correspondence with the support department from Dantec Dynamics has been established to clarify a possible error in the configuration of the IPI setup. Dantec Dynamics informs that there seems to be an indication of that the observation and scattering angle are similar in the *FlowMap Particle Sizer - Installation & User's guide* manual. In the setup the observation angle applied for the camera position is relative to the laser position, whereas it should have been the complementary angle.

It can be concluded that there is an unreliability relating to the IPI measurements. Further measurements are necessary to be conducted which are performed with a new observation angle. Consequently, it should be possible to state the reliability of IPI in relation to TDIM. Despite this, TDIM is rated as a more reliable and more straightforward approach which minimises the number of potential faults in the setup.

Vertical Bubble Flow A

The appendix covers conditions regarding single rising bubbles in stagnant water. Dimensionless numbers are used to characterise how the bubble shape will change. The hydrodynamic forces are outlined at the terminal velocity for a rising bubble. Based on these forces and the effect of the Reynolds number the terminal velocity is calculated from drag coefficient correlations.

A.1 Characteristics of Bubbles

The interaction by the surface tension and shear stress caused by the carrier fluid, determines the shape of the bubbles. Additionally, the shape is affected by the dimensions and shapes of the domain, for example a vertical pipe. Placing bubbles in a narrow pipe will cause the shape to be more elongated in comparison to bubbles in larger pipes. When the shear stress is weak compared to the surface tension, the result will be bubbles of spherical shapes. [Michaelides, 2006,p. 43-44]

In Figure A.1a is shown schematics of bubble shapes in motion along with a small description of their general appearance. This only applies to single rising bubbles and not multiple bubbles rising in a swarm. Along follows three notes regarding some of the eight bubble shapes.

Spherical (s): Completely spherical bubble can be obtained if the carrier fluid is inviscid. When the carrier fluid is viscid, shear distorts the shape of the bubble which becomes ellipsoidal. The bubble can be considered spherical, when the values of the two principal axes are within 5 %.

Oblate ellipsoidal disk (oed): The shape of these bubbles tends to be of high elongations and wobble visibly while in motion.

Oblate ellipsoidal cap (oec): The radius of the curvature tends to be higher compared to the ellipsoid.

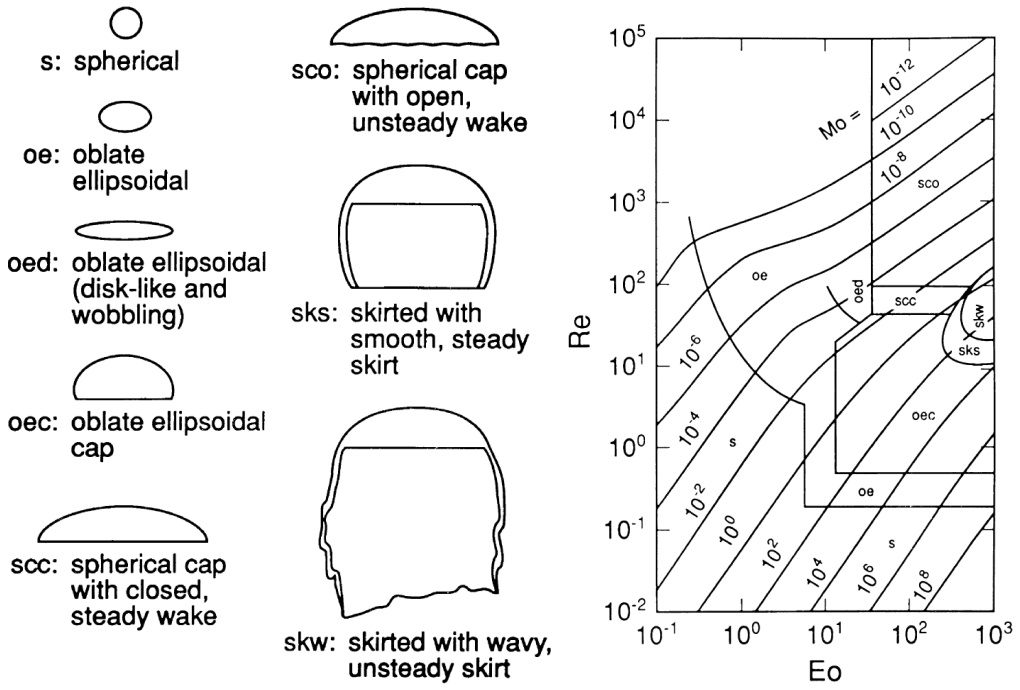

(a) Schematic diagrams of shapes of bubbles in motion.

(b) Shape map of deformed bubbles.

Figure A.1: Different shapes of bubbles and shape map, while freely rising in a column of water. [Michaelides, 2006,p. 50-51]

The shapes have been determined experimentally. The following main variables and parameters affect the shapes of bubbles while freely rising in water, see Table A.1. [Michaelides, 2006,p. 49]

Symbol	Description	Unit
v_t	Terminal velocity	m/s
d_b	The diameter of a spherical bubble	m
ρ	Density	$\mathrm{kg/m^3}$
μ	Dynamic viscosity	$\mathrm{kg/m^2 \cdot s}$
σ	Surface tension of the viscous sphere	N/m
g	Gravitational acceleration	$\mathrm{m/s^2}$

Table A.1: Variables and parameters affecting the shape of bubbles when rising in water. [Michaelides, 2006,p. 49]

These six variables and parameters are a part of the three dimensionless numbers, see Equation A.1:

- Terminal Reynolds number (ratio of the inertial to the viscous force)
- Eötvös number (ratio of gravity to the surface tension force)
- Morton number (ratio of viscous and surface tension force considering the properties for the liquid and the gas phase)

By choosing two of these dimensionless numbers a two dimensional diagram can be constructed, useful to determine different shape of bubbles. See Figure A.1b where Re and Eo constructs a shape map diagram. It must be kept in mind, that Figure A.1b has been obtained under steady flow conditions in a vertical pipe.

$$
\begin{aligned}
Re &= \frac{\rho_c d_b v_t}{\mu_c} && [-] \\
Eo &= \frac{g\left(\rho_c - \rho_d\right) d_b^2}{\sigma} && [-] \\
Mo &= \frac{g\mu_c^4\left(\rho_c - \rho_d\right)}{\rho_c^2 \sigma^3} && [-]
\end{aligned} \tag{A.1}
$$

A.2 Regions and Hydrodynamic Forces of Rising Bubbles

According to Celata et al. [2006] the terminal velocity can be distinguished into three different regimes for an isolated bubble. Each of these regions is considered in the following. Additionally, the different hydrodynamic forces are considered affecting a single steady rising bubble in stagnant water.

A.2.1 Dominated Regions

In the *Viscosity Dominated Region* the bubble will appear as spherical or nearly spherical, the motion will mainly be dominated by viscosity and buoyancy forces and the terminal velocity will increase in conjunction with the bubble diameter. [Celata et al., 2006]

In the *Surface Tension Dominated Region* the terminal velocity will be determined by surface tension and inertia forces. Depending on the bubble diameter its shape can change resulting in a constant or changing terminal velocity. This can be contributed by surface contamination, evolution of the wake structure and bubble shape oscillation as a result of the injection method. [Celata et al., 2006]

This *Inertia Dominated Region* is mainly for bubbles of high Eo with a spherical-cap shape, where the motion is dominated by inertial and buoyancy forces. The terminal velocity will increase with the bubble diameter. [Celata et al., 2006]

A.2.2 Hydrodynamic Forces

Simplifying assumptions are made for estimating the hydrodynamic forces. The trajectory of the bubble is considered not to vary significantly from its vertical rising direction, from where the bubble acceleration is given by Newton's second law. It is given in Equation A.2, stating that the net force acting on the particle is equal to its mass multiplied by its acceleration. At terminal velocity the acceleration of the bubble will be equal to zero, $a_y = 0$, and only the buoyancy, gravity and drag force are left in the equation. [Massoud, 2005,p. 365]

$$\sum F = m_b a_y = F_B - F_W - F_D \qquad [\mathrm{N}] \tag{A.2}$$

Equation A.3, A.4 and A.5 state the buoyancy, gravity and drag force. [Kolev, 2011,p. 122]

$$F_B = V_b g \Delta\rho \quad [\mathrm{N}] \tag{A.3}$$

$$F_W = V_b g \rho_b \quad [\mathrm{N}] \tag{A.4}$$

$$F_D = C_D \frac{1}{2} A_b \rho_c \Delta v^2 \quad [\mathrm{N}] \tag{A.5}$$

Where:
V_b is the volume of a spherical bubble [m^3]
g is the gravity acceleration [$\mathrm{m/s}^2$]
$\Delta\rho$ represents the difference between ρ_c and ρ_b [$\mathrm{kg/m}^3$]
C_D is the drag coefficient [$-$]
A_b is the cross sectional area of a spherical bubble $\left[\mathrm{m}^2\right]$
Δv represents the difference between v_c and v_b, known as the terminal velocity [m/s]

In the case of rising bubbles the gravity force, F_W, can be neglected, leaving only F_B and F_D in Equation A.2.

A.3 Reynolds Number Effects and Terminal Velocity

The Reynolds number, Re, stated in Equation A.1 is used to imply the ratio of the inertia force to the viscous force acting on an element. In case of a rising bubble through a stagnant fluid, these forces become important and hence Re. In general it holds that for $Re << 1$ the viscous forces will be dominant and the inertia forces can be neglected. For large Re the viscous force will appear small relative to the inertia force, where the effect of viscosity can be neglected by considering an inviscid fluid of which no shearing stresses are present. However, for rising bubbles both internal and external properties are effected by increasing Re. [Munson et al., 2012,p. 348]

A.3.1 Drag Coefficient of Viscous Spheres

Equation A.5 shows the drag force of a single rising bubble. In case of an inviscid bubble the drag coefficient will be $C_D = 16/Re$, but due to impurities in the water, bubbles will behave as solid spheres, $C_D = 24/Re$, known as Stokes solution which applies for $Re \leq 16$. [Kolev, 2011,pp. 32-33]

Based on Equation A.2 an expression is derived for the terminal velocity, v_t, by using Equation A.3 and A.5, considering C_D to follow Stokes law. See Equation A.6.

$$v_t = \frac{\rho_c g d_b^2}{18\mu_c} \quad \left[\frac{\mathrm{m}}{\mathrm{s}}\right] \tag{A.6}$$

One very important factor when calculating the drag coefficient of bubbles is whether or not they can retain their spherical shape and not become elongated at high Re. Which is why spheroids should be more expected than spheres, when dealing with high Re. As shown in Figure A.1b, a bubble can still be considered spherical at high Re as long the Eötvös number remains low, meaning the bubbles have a high surface tension. The high vorticity gradients around the viscous sphere have also a high impact on the drag coefficient, since its value is reduced in comparison to a rigid sphere. The viscosity ratio, $\lambda = \mu_b/\mu_c$, is also important when considering the drag coefficient, where $\lambda = 0$ corresponds to inviscid bubbles while $\lambda \to \infty$ corresponds to solid spheres. [Michaelides, 2006,pp. 124-126]

The expression in Equation A.7 can be used to calculate the drag coefficient for viscous spheres at steady state. The correlation is reported by Michaelides through a direct numerical simulation based on a hybrid grid. As a result, the correlation takes into account the formed boundary layer at the exterior of the sphere. [Michaelides, 2003]

(A.7)
$$C_D\left(Re,\lambda\right) = \frac{2-\lambda}{2} C_D\left(Re,0\right) + \frac{4\lambda}{6+\lambda} C_D\left(Re,2\right),\ 0 \leq \lambda \leq 2\texttt{, and } 5 < Re \leq 1,000 \quad [-]$$

The function $C_D\left(Re,0\right)$ and $C_D\left(Re,2\right)$ represents drag coefficients for inviscid bubbles and viscous drops. The expression for those is given in Equation A.8 and A.9. [Michaelides, 2006,p. 127]

(A.8)
$$C_D\left(Re,0\right) = \frac{48}{Re}\left(1 + \frac{2.21}{\sqrt{Re}} - \frac{2.14}{Re}\right) \quad [-]$$

(A.9)
$$C_D\left(Re,2\right) = 17Re^{-\frac{2}{3}} \quad [-]$$

However, Equation A.7 does not cover the range of $0 < Re < 5$. For that purpose the following correlation in Equation A.10 is recommended. A $\lambda \longrightarrow \infty$ (solid sphere) will result in Stokes Law, $C_D = 24/Re$, and for $\lambda \longrightarrow 0$ (inviscid bubble) it would be $C_D = 16/Re$. The intention for Equation A.10 is to have an upper limit of $Re = 5$, but has been concluded to hold for the numerical results up to $Re = 20$. [Michaelides, 2003]

(A.10)
$$C_D = \frac{8}{Re}\frac{3\lambda+2}{\lambda+1}\left(1 + 0.05\frac{3\lambda+2}{\lambda+1}Re\right) - 0.01\frac{3\lambda+2}{\lambda+1}Re\texttt{ln}\left(Re\right)\texttt{ ,}\ 0 < Re \leq 5 \quad [-]$$

For the correlations given in Equation A.7, A.8, A.9 and A.10 the standard deviation comparing to the numerical results is 2.1 % with a maximum error of 4.6 %. [Michaelides, 2003] Additionally, these expressions can be applied only to viscous spheres with clean surfaces. Impurities will increase the surface tension and cause behaviour similar to a rigid sphere. [Michaelides, 2006,p. 128]

In the same manner as for Equation A.6, the terminal velocity v_t can be calculated based on a spherical bubble diameter and the correlations given in Equation A.7 and A.10. Simultaneously Re can be found based on the calculated v_t. Figure A.2 shows how Re increases for bubbles with a diameter ranging from 0 to 1 mm.

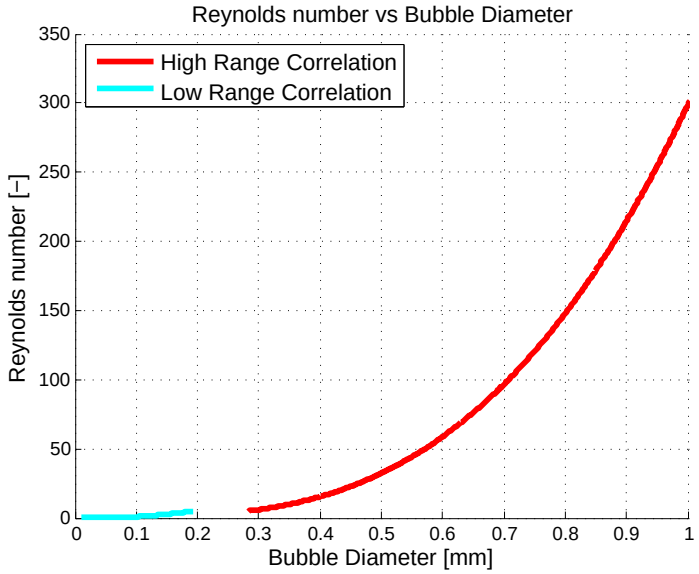

Figure A.2: Reynolds number for spherical bubbles at different diameters by Michaelides correlations.

The Low and High Range Correlation do not coincide at $Re = 5$, not even by adding the reliability of Equation A.10 up to a range of $Re = 20$. The diameter is approximately 0.19 and 0.28 mm at $Re \approx 5$ for the Low and High Range Correlation. In Figure A.3 is shown how Re is related to C_D for the Low and High Range correlation.

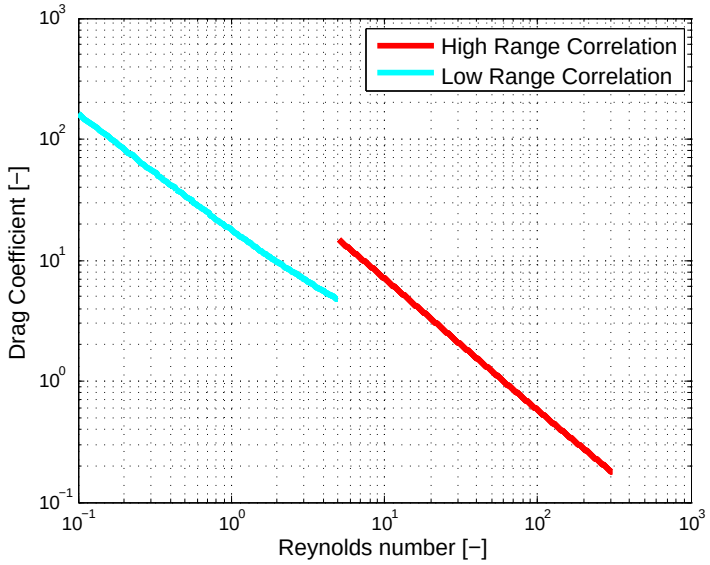

Figure A.3: Drag coefficient for changing Reynolds number by Michaelides correlations.

A.3.2 Terminal Velocity

The terminal velocity can be difficult to approximate, since it changes from the injection of the bubble and as it travels up through the water column. Additional impacts come from the degree of contamination of the fluid, which will affect the dynamics of the interface, and effects of the trajectory of the bubbles which might be rectilinear, planar zigzagging or spiraling and change according to the distance of the injection. In case of closely packed bubbles the wake produced from the previous bubbles can influence the terminal velocity, as well can the change in bubble volume as the liquid static head is reduced. [Celata et al., 2006]

Figure A.4 shows the dependency of the terminal velocity of a single rising bubble with regards to it diameter. The inconsistencies between the Low and High Range Correlation is also seen here for v_t for which v_t is 22.3 and 15.9 mm/s for the corresponding diameters.

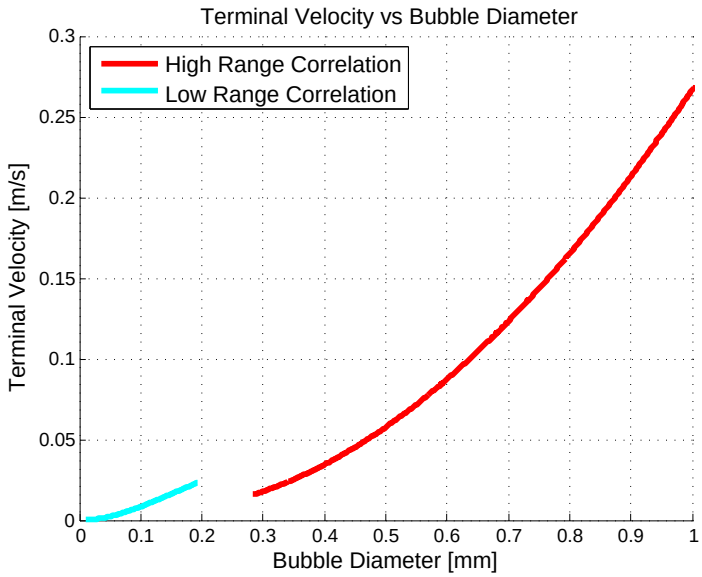

Figure A.4: Terminal velocity as function of increasing bubble diameter.

Design & Test of Experimental Setup for Rising Bubbles

B

Throughout the appendix a review is given of the rising bubble column regarding its design and how the bubbles are generated. Additionally, tests prior to Telecentric Direct Image Method and Interferometric Particle Imaging are performed with a microscope camera. It is done to give an indication of the necessary pressure for bubble generation and how the bubbles changes regarding to size, shape and their distribution in the Field of View (FOV).

The experimental setup is designed to achieve rising bubbles which will not be affected by the influence from the surrounding walls. Additionally, rising bubbles of less than 1 mm in diameter are desired to represent the two phase flow, since these are assumed to remain their spherical shape.

Hansen [2009] designed an experimental setup for Interferometric Particle Imaging (IPI) measurements on rising bubbles in a water column with the same equipment from Dantec Dynamics. It consisted of a plexiglass column with a square cross section with dimensions of 15×15 m^2 and a height of 1 m. The air was introduced through holes of 1 mm in diameter drilled into a plate in the bottom in a pitch. A similar setup design is considered to be useful for performing IPI and Telecentric Direct Image Method (TDIM).

B.1 Plexiglass Column

A rectangular transparent plexiglass column is utilised for the stagnant liquid with rising bubbles. The dimensions of the plexiglass column are indicated in Figure B.1 both from a side and a top view. Table B.1 shows the values for the different dimensions from Figure B.1. The column is filled with demineralised water until the height of H.

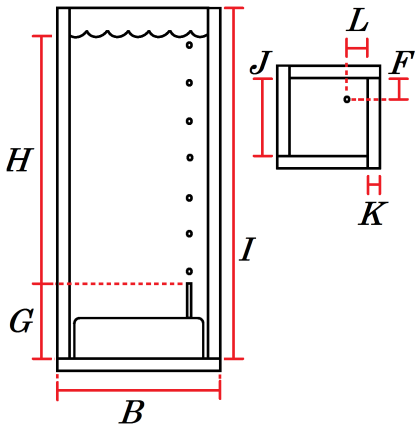

Figure B.1: Sketch of the plexiglass column, side and top view.

	Description	Distance [mm]
B	Front to back side of the column	166
F	Cannula from internal wall	72
G	Inner bottom to cannula opening	115
H	Water column above cannula	280
I	Internal height of column	480
J	Internal width of column	150
K	Thickness of wall	8
L	Cannula from internal wall	22

Table B.1: Dimensional specification for the plexiglass column.

B.2 Bubble Generation

The generation of bubbles occurs from the bottom of the plexiglass column as shown in Figure B.1. Compressed air is supplied through rubber tubes to an upwardly directed cannula located at a distance of G above the bottom of the plexiglass column. The cannula is mounted on a plastic cube which is movable on a stainless steel platform, see Figure B.2a. The applied cannula has an external diameter of 0.6 mm. In order to obtain small bubbles within a range of a desired diameter, the cannula is modified. It is done by compressing the tip of the cannula parallel relative to the acquired FOV, see zoom in Figure B.2a. In Figure B.2b is shown an image of bubbles generated just above the cannula, notice the difference in size.

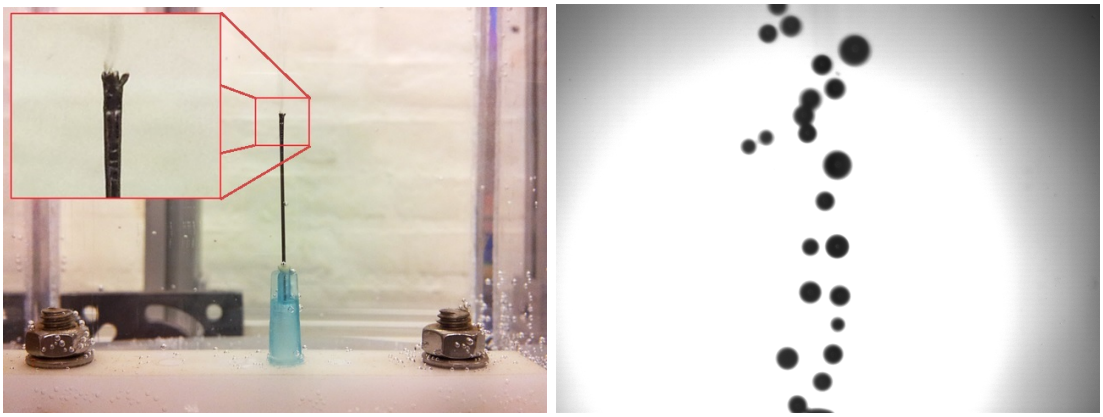

(a) Compressed cannula on a plastic cube.

(b) Generated bubbles above the cannula.

Figure B.2: Bubble generator to produce multiple bubbles varying in size but below 1 mm in diameter.

B.3 Pressure Measurement

For measuring the pressure of the air delivered to the cannula a compact type 8314 pressure transmitter from Bürkert is utilised along with a NI USB-6215 DAQ module for data sampling. The pressure transmitter is installed as required in the data sheet with the pressure connection in downward position. The pressure measured is relative to the surrounding pressure. Technical data is given in Table B.2.

Bürkert type 8314		
Power supply	8-33	V DC
Output signal	4-20	mA
Pressure range	0-1	bar
Response time	< 2	ms
NI USB-6215		
Measurement type	Voltage	V
Resolution	16	bits
Maximum voltage range	-10, 10	V

Table B.2: Technical data for the compact type 8314 pressure transmitter and the NI USB-6215 DAQ module. [Bürkert - Fluid Control Systems, 2003], [National Instruments, 2012]

The circuit with the pressure transmitter is shown in Figure B.3. The NI USB-6215 DAQ module measures the voltage over a 464 Ω resistance generated by the output signal of the pressure transmitter which varies from 4 to 20 mA. From Ohm's law it results in a voltage range from 1.856 to 9.28 V, which serves as the analogue voltage input to the DAQ module.

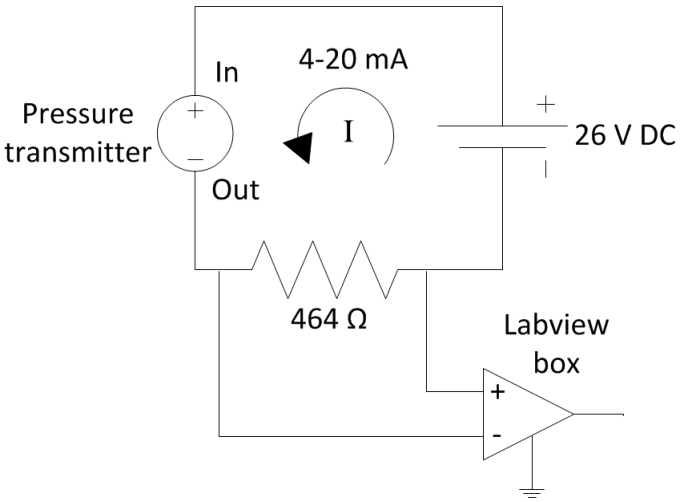

Figure B.3: Pressure transmitter circuit.

In Figure B.4 is shown the linear relationship between the range of the output signal from the pressure transmitter and the measured pressure.

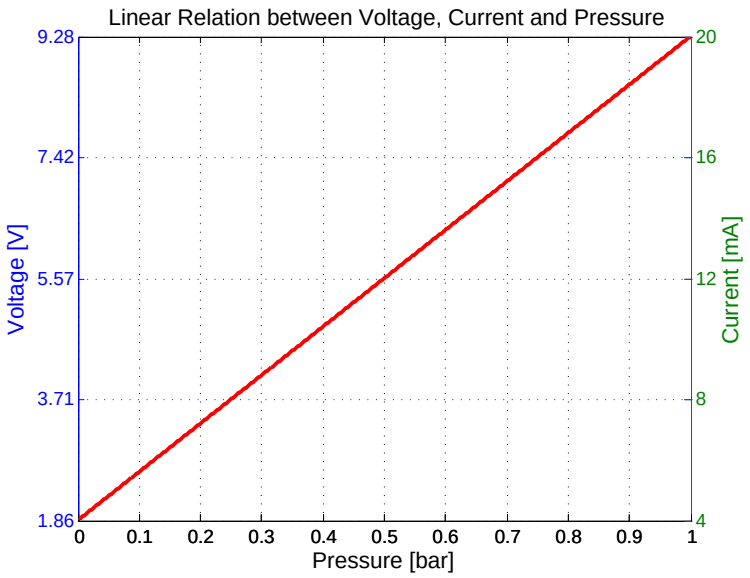

Figure B.4: Linear relation between the pressure and the output current of the pressure transmitter.

Equation B.1 is the linear relation between the pressure and current. Additionally, it shows how the resistance is used to calculate the voltage range given as analogue input to the DAQ module.

$$p = \frac{1}{16 \cdot 10^{-3}} I - \frac{1}{4} = \frac{1}{16 \cdot 10^{-3}} \frac{U}{464} - \frac{1}{4} \quad \text{[bar]} \tag{B.1}$$

Where:
p is the pressure delivered to the cannula [bar]
I is the current delivered by the Bürkert type 8314 pressure transmitter [mA]
U is the voltage over the resistance measured by the NI USB-6215 DAQ module [V]

B.4 Test of Experimental Setup

Tests of the experimental setup are performed to investigate the range of bubble sizes generated at different pressures. This is done by use of the experimental equipment and experience from a previous study described in the paper *Bubble Detection using Digital Image Processing* [Christensen and Thomassen, 2013].

The bubble column described in Section B.1, has been equipped with a micro scope camera. It is located on a traverse which can move the camera along with and closer to the bubble column, but not up and down. The camera data is specified in Table B.3.

Pixel Resolution	2592×1944
Magnification Rate	20-90×
Sensor Type	Color CMOS
Frame Rate	Up to 30 fps
Focal length	15.6 mm
f-stop number	f/7.8
Exposure time	Automatically adjust to the luminance

Table B.3: Specification for Dino-Lite Premier AD7013MTL. [AnMo Electronics, 2014]

A 500 W halogen lamp is used as white background light. The halogen lamp is chosen above a 10 W LED lamp since the halogen lamp will saturate the image faster, which is beneficial when dealing with moving objects. The diffuse light condition is made by locating two diffuse plexiglass plates in between the lamp and the bubble column, whereof one is more diffuse than the other.

The location of the camera, bubble column and light setting is shown in Figure B.5 along with specified dimensions.

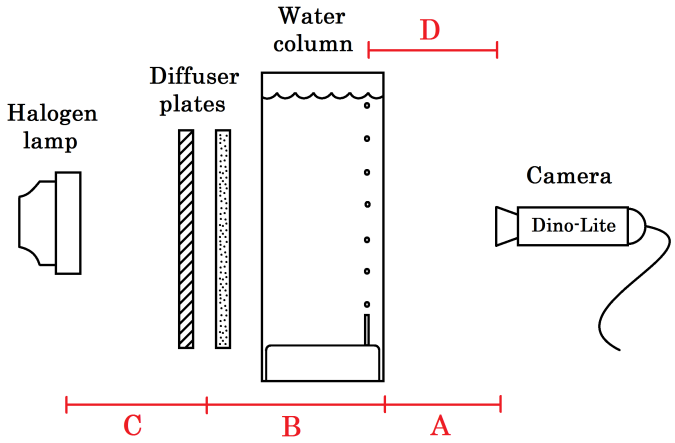

Figure B.5: Sketch of the direct image setup with indicated dimensions.

A represents the distance from the camera to the front of the bubble column, B is the front of the bubble column to the diffuser plates, C is the diffuser plates to the halogen lamp and D represents the Working Distance (WD). The pixel resolution of the camera is set to 640×480 since a higher value will decrease the number of frames per second, making the bubbles appear blurred. The centre of the FOV is located 137 mm above the cannula opening, where the bubbles appear to have reached a steady velocity and occur to no longer disperse away from the centre in the FOV. A great majority of the bubbles must be represented in FOV for estimating d_b. The size, number and dispersion of bubbles depend on the input pressure p, while the size of FOV depends on the magnification rate (MR) of the camera. An inspection is performed of the bubble behaviour at different input pressures p. MR is fixed at 10× which results in the largest FOV the camera can be manually adjusted to, with an adjusting WD according to have the rising bubbles in focus. Figure B.6 shows six images of rising bubbles within FOV at different pressures.

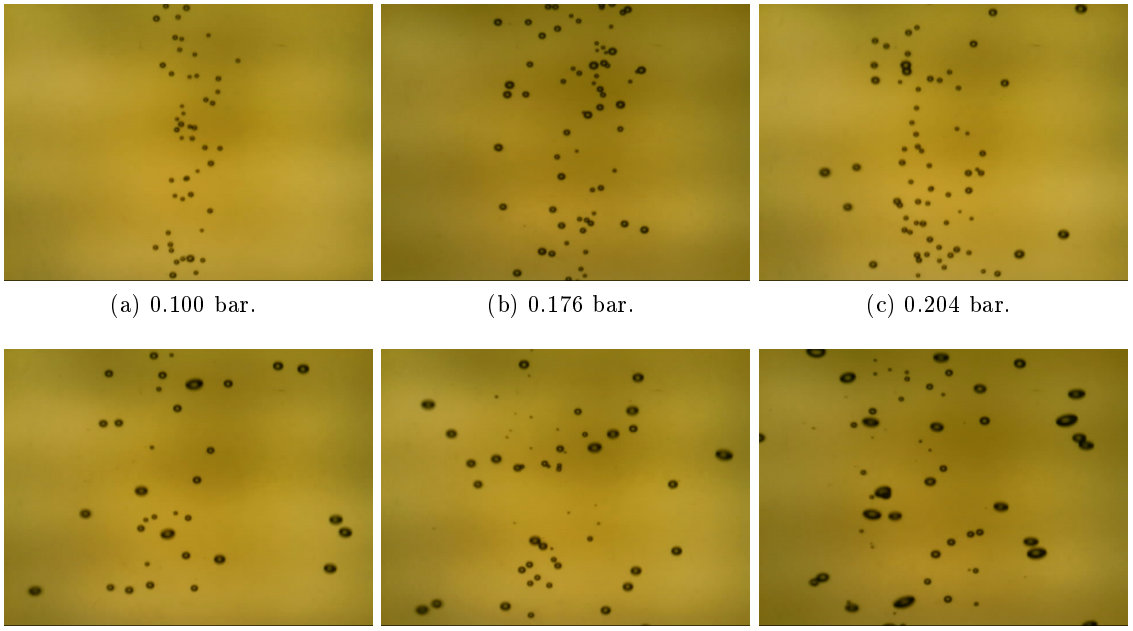

(a) 0.100 bar. (b) 0.176 bar. (c) 0.204 bar.

(d) 0.300 bar. (e) 0.400 bar. (f) 0.997 bar.

Figure B.6: Bubble images acquired with different input pressures and a MR fixed at 10×.

Figure B.6a shows a narrow column of rising bubbles at a gauge pressure of 0.100 bar, which is the pressure necessary for bubble generation. As the pressure increases to 0.400 bar in Figure B.6e, the column becomes wider and fills out the entire FOV. In addition, the bubbles increase in size. Figure B.6f shows bubbles at 0.997 bar, which is the highest value the pressure transducer can measure. The column is wider than FOV and the bubbles appear less spherical and seem to have a high size distribution.

From Figure B.6 the bubbles appear smaller and more spherical with a low size distribution when the pressure is low. For IPI the bubbles must be spherical, consequently the input pressure p will be kept at approximately 0.100 bar. In addition, the corresponding FOV is not fully utilised at MR10×, meaning less pixels are used to highlight the bubbles. Thereof, bubble images will be taken with an MR of 30× to utilised most of the available pixels. Table B.4 shows the setup settings indicated in Figure B.5 at MR30×.

A [mm]	B [mm]	C [mm]	D [mm]	p [bar]	T_{water} [°C]
68	185	150	A+L+K	0.101	26

Table B.4: Experimental settings for image acquirement.

Based on the settings for Table B.4, 100 images are taken, which are to be used to estimate the bubble diameter.

B.4.1 Calibration

To estimate the bubble size from the images, a calibration is necessary to get from pixel dimensions to real-world dimensions. The calibration process is described in Section D.2 in Calibration for IPI & TDIM - Appendix D. Table B.5 contains data for the calibration

carried out in NI Vision Builder. Bubbles extracted through digital image processing can now be estimated in real-world units.

# calibration points	108	-
Pixel resolution	642×483	pixel
Resolution	18.59	μm
FOV_x	11.93	mm
FOV_y	8.98	mm
Mean error, $\bar{\epsilon}$	15.93	μm
Error range, ϵ	15.76-16.83	μm
Std. deviation, *s.d.*	0.17	μm
Distortion %, D	0.51	%

Table B.5: Calibration data extracted from NI Vision Builder.

B.4.2 Image Processing

The images are converted into grayscale by extraction of the luminance plane. No filters are applied for smoothing or so. A global threshold is applied for dark objects to mark the haloes of the bubbles. Two binary morphology functions, *Remove border objects* and *Fill holes*, are utilised before the Heywood circularity factor is applied as a particle filter for the overlapping bubbles. Only a few couples of overlapping bubbles exist at each image and thereby it is chosen not to take them into account. The images are calibrated, before the particles are detected and particle data extracted for further processing.

B.4.3 Size Distribution

Two parameters are extracted for the detected bubbles, the area and width. From the area a bubble diameter can be found by assuming a spherical shape of the bubbles. This can be compared with the width of the bubble, which also should be equal to the diameter if the bubbles are spherical. The results are displayed in the histograms in Figure B.7a and B.7b. The bin range is set to 20 μm.

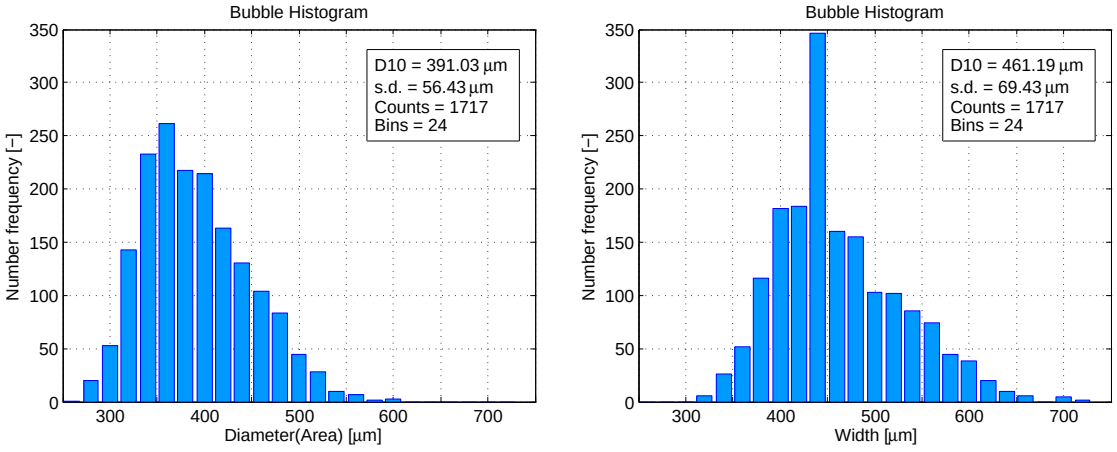

(a) Bubble diameter as a function of the area.

(b) Bubble width.

Figure B.7: Size distributions of the bubble diameters.

Both figures indicate a mean bubble diameter below 0.5 mm, which is within the desired range below 1 mm. However, there is a difference of 70 μm between the two mean diameters, which clearly indicates that the extracted bubble contours are not perfectly circular. A mean Heywood circularity of the bubbles is calculated to 1.038 indicating that the bubble contours are not perfectly circular. Either, the bubbles are not spherical or else the camera is not suitable for the purpose of image capturing of moving objects. A combination of the two cases is also a possibility. The exposure time of the camera is automatically adjusted in relation to the luminance of the scene. Thereby it is not possible to control exposure time and thereof how far the bubbles move during the acquisition. This can lead to errors in the exact bubble contour. Another camera has to be applied for a more precise size detection of the rising bubbles.

With regards to the not perfectly spherical bubbles, it is however presumed that IPI measurements can be conducted without any difficulties.

IPI Software Settings C

The settings for the FlowMap Particle Sizer (FMPS) software are explained and justified based on their ability to detect and validate bubbles and if they provide a realistic estimate of the bubble diameters. Table C.1 is divided into eight tabs which all contains important parameters for data processing. Each tab is reviewed and justified for its setting.

C.1 General

The General tab contains parameters for image selection and processing in the defocused image. The minimum and maximum pixel size of the circle mask are estimated as shown in Figure C.1b, which are related to the circles in the defocused image. The circle size must fit to the defocused image since it decides the diameter of the bubble in conjunction with the fringe frequency.

For estimation of the circle size an average is taken of the horisontal diameter of 10 bubbles in the defocused image. The average becomes 76.8 pixels for which a range of ± 5 pixels is set. The reason for choosing the horisontal diameter is the oblate appearance of both the focused and defocused glare point images caused by the angle of the camera, and the fact that the fringes are orientated vertically.

The Step size indicates the step between the minimum and maximum mask, which is set at a minimum. The Size of FFT is used for processing fringe data and must be larger than the maximum circle mask, which is set at maximum. [Dantec Dynamics, 2003]

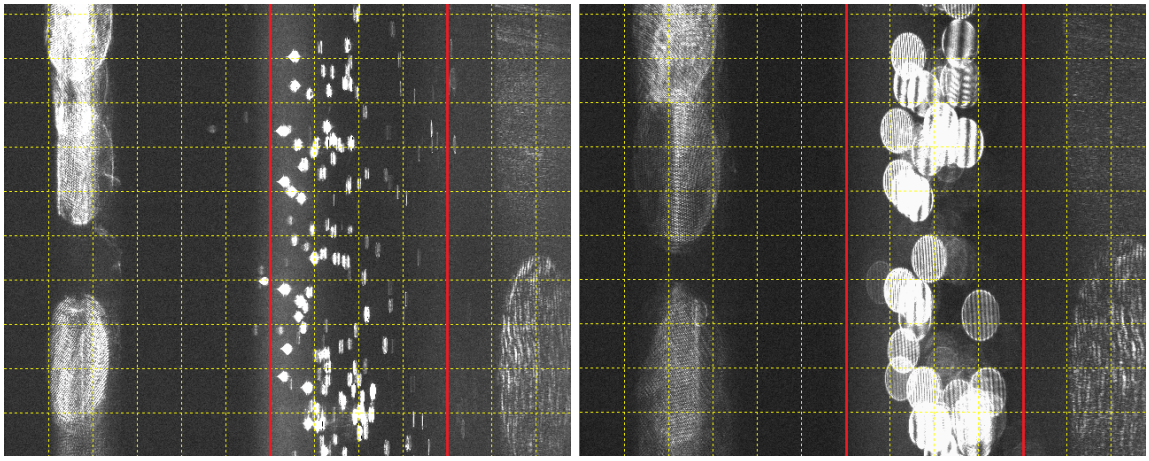

(a) Glare points in the focused image of camera A. (b) Estimation of circle mask in the defocused image of camera B.

Figure C.1: Images of camera A for a focused image and camera B for a defocused image both with grid intervals of 100 pixels. The elongation of the glare points and defocused fringes is caused by perspective error in the setup. The bright spots to the left and right in FOV are caused by reflection from the plexiglass column.

C.2 Optical Setup

The angle which is to be set in the FMPS software is considered to be the scattering angle between the bubbles and the laser sheet. In Section 3.3 the observation angle is experimentally estimated to be 35°. By taking into account the index of refraction as given in Section C.2.1 and Figure C.3, the scattering angle is calculated to be 52.07°. It is assumed that the FMPS software does not take into account the index of refraction and hence the scattering angle is set to 52.07°.

Additionally the tab relates to the physical properties of medium and particle and the light sheet. The refractive index of air is 1.001 while it is 1.334 for water at 1 bar and a temperature of 20 °C [Albrecht et al., 2003,p. 29]. The aperture diameter is based on the f-stop number, see Equation C.1 [Hornberg, 2006,p. 137]. The Diameter range is based on Equation 3.11, 3.12 and 3.13. [Dantec Dynamics, 2003]

$$f = \frac{FL}{d_a} \qquad [-] \tag{C.1}$$

Where:
f is the dimensionless f-stop number [−]
FL is the focal length, distance between the sensor and the lens [m]
d_a is the diameter of the aperture in the iris [m]

C.2.1 Influence of Refraction

For estimation of the bubble diameter by using Equation 3.10 and 3.11, two constants for κ need to be measured on the experimental setup. The distance from the aperture of the

camera to the laser sheet, Z, and the observation angle in water, ϕ_w. The two parameters are indicated in Figure C.2, which shows the optical path from the camera optic to the laser sheet inside the water column seen from above.

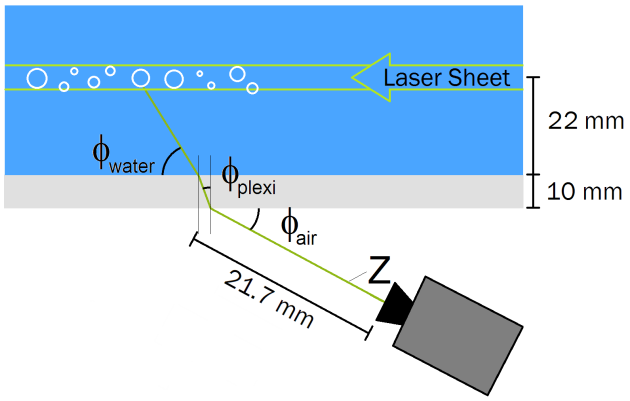

Figure C.2: Bubble column wall seen from above. Distance Z follows the optic path line from the center of the lens to the laser sheet.

C.2.1.1 Angle Calculation

The camera is placed outside the bubble column and thereby the light is refracted by the transition from water to air. The observation angle in water can be found by Snell's law given by Equation C.2. Normally Snell's law uses angles relative to the normal of the surface, but in this case it is given for the angle relative to the surface.

$$\phi_w = cos^{-1}\left(\frac{n_a}{n_w} cos(\phi_a)\right) \quad [°] \tag{C.2}$$

Where:
n_w and n_a are the refractive indexes of water and air respectively [−]
ϕ_w and ϕ_a are observation angles in water and air respectively, see Figure C.2 [°]

Figure C.3 shows Equation C.2 as a function of the observation angle in air.

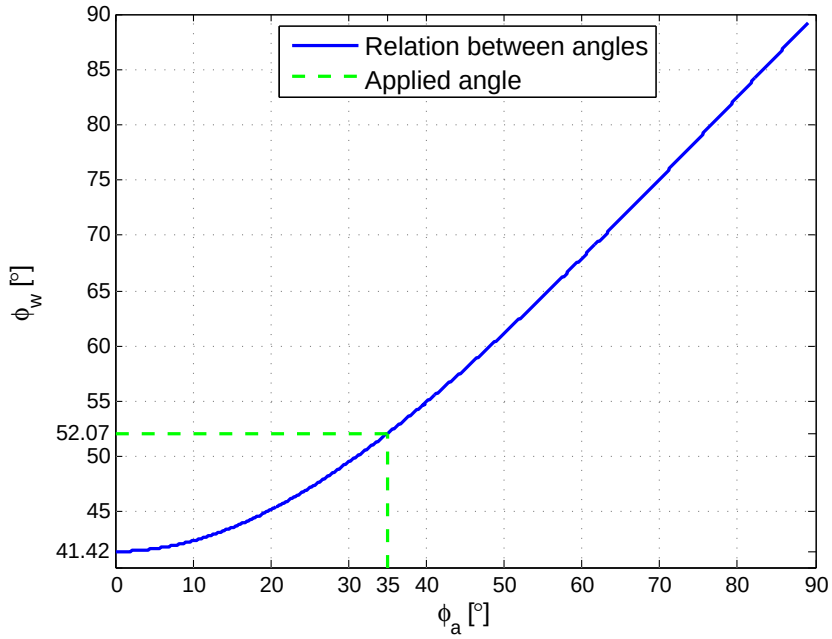

Figure C.3: Observation angle in water as a function of the observation angle in air.

The minimum possible observation angle of the bubbles in the water column is 41.42°. This is the critical angle, where total internal reflection of the light rays occurs, given by Equation C.3 [Jewett and Serway, 2008,p. 993]. To obtain the optimum scattering angle of 45° according to the theoretical approach using Lorenz-Mie diagram given in Section 3.2.2 in Chapter 3 the observation angle of the camera has to be 19.4° according to Figure C.3. However the best observation angle according to tests in Section 3.3 is 35°, which results in ϕ_w being equal to 52.07°.

$$\phi_c = cos^{-1}\left(\frac{n_a}{n_w}\right) \quad [°] \tag{C.3}$$

C.2.1.2 Distance Calculation

The distance from the camera lens to laser sheet, Z, is shown in Figure C.2 as the dark green path. The observation angle makes the measurement area and FOV distorted due to perspective also known as warping. This means that Z varies in the horisontal direction across FOV. The distance Z is calculated from the center of the lens to the center of the FOV located in the laser sheet.

In Figure C.4 the distance Z is shown as a function of the observation angle in air, ϕ_a, where the distance in air to the plexiglass is kept constant at 21.7 mm. The thickness of the plexiglass is 10 mm and the perpendicularly distance from the plexiglass wall to the lasersheet is 22 mm. The preceding distances are measured in the experimental setup given in Section 3.3. The calculation of Z is based on Snell's law, see Equation C.2, and trigonometry.

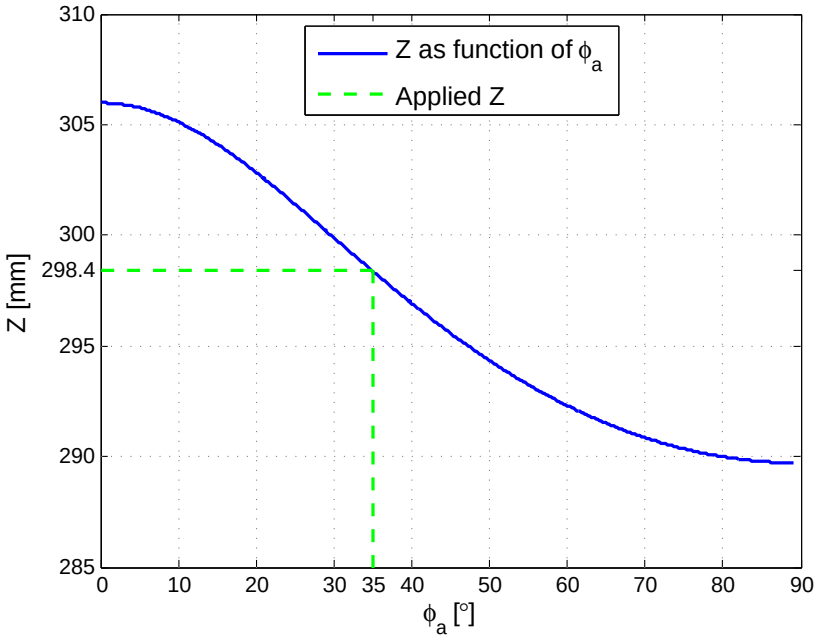

Figure C.4: Distance Z as a function of the observation angle in air.

The distance Z varies with ∼5% for an observation angle in air, ϕ_a, between 0 and 90°. At an observation angle in air, ϕ_a, at 35° the distance, Z, is calculated to 298.4 mm as shown in Figure C.4.

C.3 Calibration

The Calibration tab acquires calibration images from camera A and B to carry out an Imaging Model Fit (IMF), see Section D.1 in Appendix D. The calibration can then be added to the images taken with camera A and B. An example of the IMF is shown in Figure D.2. The corrective offset which can be applied in the x- and y-direction can be used to line up particles in camera A and B in case that the calibration has been affected. [Dantec Dynamics, 2003]

C.4 Laser Setup

The settings under the Laser setup tab indicate position of the incident Laser source origin relative to the front of the lens. Its position is used to indicate how the fringes are rotated, which is dependent on the particle position in the image. The X, Y and Z are indicated in Figure 3.6a in Chapter 3. The thickness of the light sheet at its beam waist must also be set, which is stated in Section 3.3. [Dantec Dynamics, 2003]

C.5 Filter

The Filter tab is useful in the event of images with high particle concentration in this case many present glare points. A minimum distance in between the particles can be selected which will reduce the detection of particles closely assembled. The number of pixels is

chosen to obtain a reasonable number of detected bubbles in each image where not too much overlap is present. The Filter tab is not enabled since it is estimated that the image is not overloaded with bubbles, due to the thin light sheet. [Dantec Dynamics, 2003]

C.6 Window Setup

The Window setup tab chooses a window to smooth the peaks in the 2D FFT for the dominant frequency peaks, which is the input data in form of the fringe frequency. This smoothing can be done prior to the data processing by a Hanning window. The orientation of the window can be applied in the x- and y-direction or both, whereof the x-direction is chosen since it would be most advantageous as the fringes appear vertically in the image.

100 images are used to test the strength of the Hanning window at 0, 25, 50, 75 and 100 %. The Hanning window has no influence on the circle size, but as its strength is increased the frequency in the x- and y-direction increases as well, while the dominant frequency peak decreases. As a result, the number of calculated fringes from the circle size and frequency in the x-direction tend to surpass the number of visible fringes in the images. Additionally, bubbles are sorted out which appear to have been validated due to the reduced dominant frequency peak and the peak frequency threshold. Consequently, the strength factor of the window is set at 0 %. [Dantec Dynamics, 2003]

C.7 ROI/Validation

Not all of the FOV is required for processing, for this the ROI/Validation tab is used. The dimensions of the Region Of Interest (ROI) is set as the width and height of the images which are covered by the rising bubbles, respectively the range in the x- and y-direction. This is chosen based on the focused image in Figure C.1a and the defocused image in Figure C.1b, where the ROI is marked by the red lines. The glare points and fringes are not located at the same position due to perspective error which only occurs in the x-direction. For this reason, the ROI in the y-direction is set to cover the entire image, while in the x-direction it is set based on the location of the glare points furthest to the left and the fringes furthest to the right.

Validation settings are also included under this tab. By increasing the peak level threshold percentage less particles should be validated since they are rejected if above the percentage value of the dominant frequency peak height. 100 images are used to test the effects of a peak level threshold of 1, 2 and 3 %. By increasing the percentage it turns out that fewer bubbles are validated, for which good candidates are not validated when the percentage surpass 1 %.

The Allowable overlap rejects particles which are considered to have a too small useable area. The allowed overlap of the size for the defocused particles is set to 70 %, meaning that the following 2D FFT is applied to the remaining area of the circle size.

The frequency ratio in the x- and y-direction are used to verify if the particles have sufficient fringe information. If fringes are present in the x-direction then small frequency peaks will exhibit in the y-direction, resulting in a high fringe ratio. For 100 acquired

images, the Fx/Fy ratio varies from 2 to infinity. All the validated defocused images seem reliable and due to this the Fx/Fy ratio is set to 1. [Dantec Dynamics, 2003]

C.8 Velocity Setup

The last tab is the Velocity setup which is used for Particle Tracking Velocimetry (PTV) analysis. It utilises cross-correlation on the focused image pair to estimate the flow direction. The interrogation size is set at its maximum to obtain reliable results from the PTV analysis, since few particles are present when performing IPI in comparison to PIV.

The noise removal is also tested for 100 images at 35, 50, 65, 80 and 95 %. At 35 % too many bubbles are detected in the images, which are clearly not bubbles or bubbles with very poorly defined fringes. When reaching 95 % only bubbles which seems reliable are registered in the image. Luminance Increment Threshold (LUT) is used to enhance all visible details in the image to exclude any possible present bubbles. From sample images without applying the laser and instead diffused backlight it is estimated that no more than 100 bubbles will be present in each image. [Dantec Dynamics, 2003]

C.9 Chosen Settings for FMPS

General		
Minimum size of defocused image	72	pixel
Maximum size of defocused image	82	pixel
Step size	1	-
Size of FFT	512	-
Optical setup		
Scattering angle, ϕ_{sca}	52.07	°
Refractive index medium, n_m	1.334	-
Refractive index particle, n_p	1.001	-
Aperture diameter, d_a	21.4	mm
Distance, Z	298.4	mm
Diameter range	59.30 to 1215.58	μm
Calibration		
Camera A	IMF: XYZ - cam.1	-
Camera B	IMF: XYZ - cam.2	-
X offset	none	pixel
Y offset	none	pixel
Laser setup		
Laser source origin	X:145, Y:0, Z:193	mm
Laser sheet thickness	0.6	mm
Filter		
Minimum distance between particles	Not enabled	pixel
Window setup		
Window type	Hanning	-
Window direction	X	-
Window strength	0	%
ROI/Validation		
X min	600	pixel
X max	1000	pixel
Y min	0	pixel
Y max	1024	pixel
Peak level	1	%
Allowable overlap	70	%
Fx/Fy frequency ratio	1	-
Velocity setup		
Interrogation size	256	pixel
Overlap	50	%
Background noise removal	95	%
Maximum number of particles to validate per image	100	-

Table C.1: Settings for FlowMap Particle Sizer.

Calibration for IPI & TDIM D

The calibrations applied to Interferometric Particle Imaging (IPI) and Telecentric Direct Image Method (TDIM) are performed in FlowMap Particle Sizer (FMPS) and NI Vision Builder, respectively. The setup used for the calibrations is quite similar but the approach of generating the calibrations differs. The two approaches are outlined in the following.

D.1 Calibration in FlowMap Particle Sizer

In order to transform one position in image A to another position in image B a calibration between the two images is required. It is done using a calibration target, where markings of known dimensions are compared between the focused image and the defocused image. In the centre of the calibration target is a larger dot encircled by four smaller dots. The larger dot represents the origin of the coordinate system $(0, 0, Z)$ whereas the smaller dots indicate the x- and y-axis. The calibration target is aligned with the laser sheet and traversed normally through the laser sheet to its centre. The calibration will compensate for the difference in scale between the two images as the presence of perspective error. [Dantec Dynamics, 2003,pp. 2.11-2.12]

D.1.1 Contrast of Calibration Images

The calibration target is illuminated uniformly to achieve high contrast between the black dots and the white background. The quality of the contrast is evaluated based on a histogram of pixel values, see Figure D.1. The histogram must have two distinct peaks if a high contrast of the calibration images is desired. The best distinct peaks are obtained by changing the f-stop number of camera A and B. Figure D.1a shows the histogram of pixel values for camera A at f/5.6 with two peaks located far apart at gray scale values of 976 and 2992. It is more difficult to obtain distinct peaks and consequently a high contrast for camera B, see Figure D.1b. The f-stop number is set to f/22, with peaks located close together at grey scale values of 832 and 976.

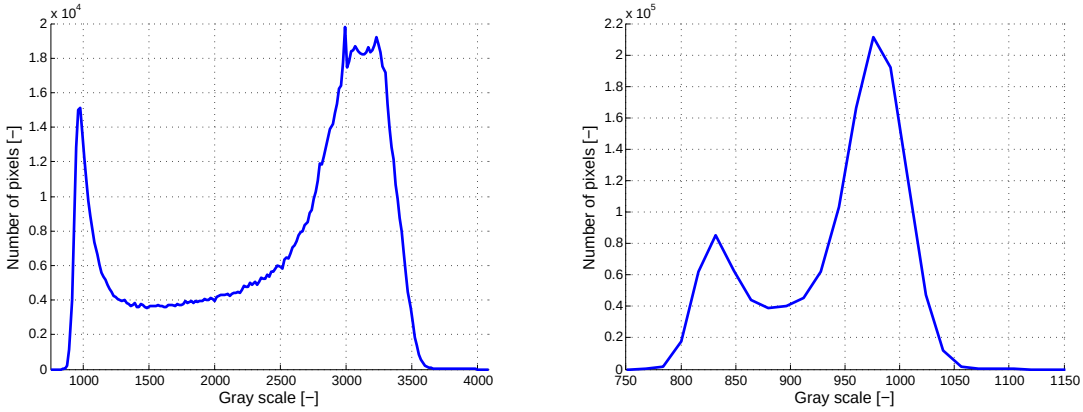

(a) Camera A with f/5.6.

(b) Camera B with f/22.

Figure D.1: Histogram of pixel values for 12 bit images acquired from camera A and B, mind the scale on both axes.

D.1.2 Imaging Model Fit

Two different imaging models may be selected; the Direct Linear Transform (DLT) or the XYZ-Polynomial. DLT is not capable of describing nonlinear phenomena like distortion due to poor camera lenses or complex refractions, such as measuring through plexiglass from air into water. In cases of significant nonlinearities the XYZ polynomial imaging model tends to be superior to the DLT. [Dantec Dynamics, 2000a,p. 9.23]

In the FMPS software three selections must be made before carrying out the Imaging Model Fit (IMF). The target is chosen as a *Dots, 100×100mm* (dot spacing of 2.5 mm) plate while the imaging model is set to *3rd order XYZ-Polynomial*. The orientation of the coordinate system is set to $x \leftarrow$ (x is positive to the left) and $y \downarrow$ (y is positive downwards). It is due to the flip of 180° of the double camera mount. [Dantec Dynamics, 2000a,pp. 9.21-9.23]

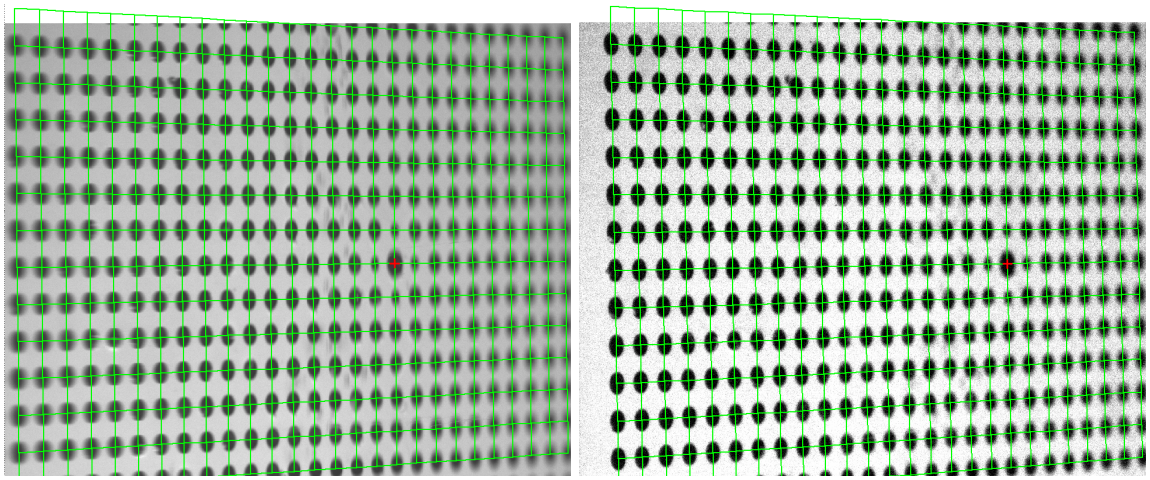

(a) Camera A with f/5.6.

(b) Camera B with f/22.

Figure D.2: IMF result based on five images for each camera, mind that the LUT has been modified for visual improvement.

In Figure D.2 is shown the result of the IMF based on five images for each camera having the same contrast as given in Figure D.1. The light green mesh shows the predicted markers on the image target with the origin of the coordinate system as the red cross.

D.1.3 Dewarping Image

As seen in Figure D.2 the cameras are not orientated normal to the calibration target and consequently the light sheet. The off-axis makes the images suffer from perspective distortion, also known as warping. Meaning that there will be a varying scale factor across the FOV. This is also visible in Figure D.2 giving the impression that an off-axis image will cover a larger area in comparison to an on-axis camera. Instead of covering a square each pixel will cover an elongated trapezoidal section resulting in loss of information. The image can be dewarped by changing trapezoidal sections into squares, but the lost information will not be recovered, see Figure D.3. [Dantec Dynamics, 2000a,p. 9.20]

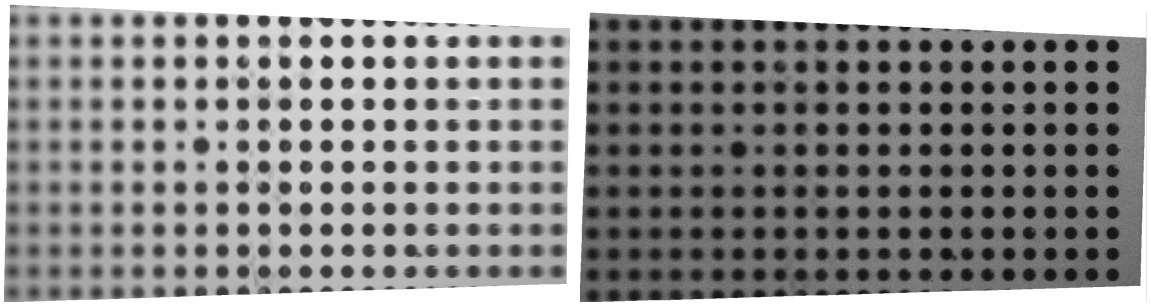

(a) Camera A with f/5.6. (b) Camera B with f/22.

Figure D.3: Calibration after dewarping the images.

D.2 Calibration in NI Vision Builder

To get from pixel dimensions to real-world dimensions calibration is necessary. As light passes through the water column from the light source to the camera, it will be diverted. It results in a FOV of different dimensions and a changed Working Distance (WD). To compensate, the setting for A and D are set according to Table 4.1 in Chapter 3. The calibration is carried out by a transparent calibration mesh placed on top of the *Dots, 100×100mm* target used for the IPI calibration and located above the cannula opening which is equivalent to distance D.

An image is taken of the calibration mesh. The calibration procedure is carried out in NI Vision Builder, where 70 calibration points are marked in the image for TDIM 1, see Figure D.4a. Each point is given real-world coordinates and spatial calibration is applied. In Vision Builder the applied method is called *Point Coordinates Calibration*. A pixel to real-world mapping is performed while correcting for perspective and distortion errors, for which the *Polynomial (K1) Distortion Model* is applied. Figure D.4b shows the combined error map of the calibration. The highest error between the calibration mesh representing the real world and the pixels occurs near the edges of Figure D.4a.

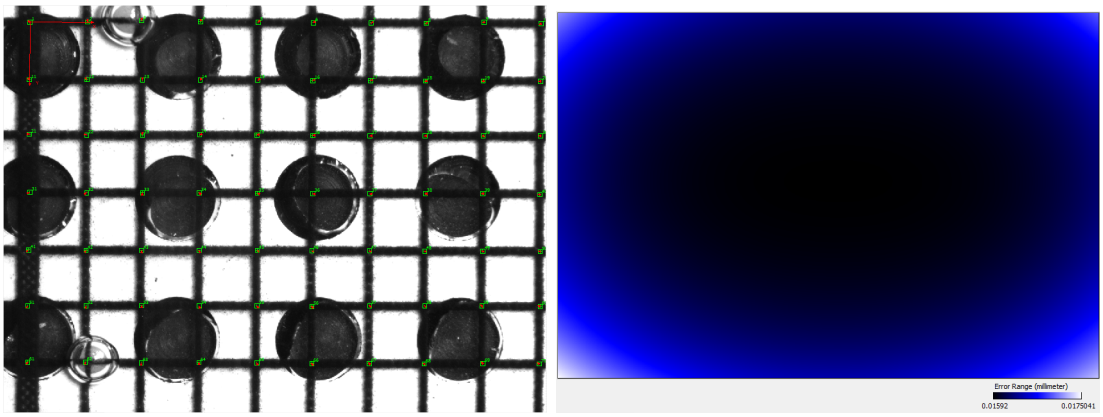

(a) Calibration mesh with calibration points. (b) Combined error map.

Figure D.4: Transparent calibration mesh with calibration points and error map for TDIM 1.

Table D.1 contains data for the calibration carried out in NI Vision Builder and the combined error map in Figure D.4b. Bubbles extracted through digital image processing can now be estimated in real-world units.

	TDIM 1	TDIM 2
# calibration points	70	63
Pixel resolution	1283×961	1280×964
Resolution	7.46×7.40 μm	7.48×7.44 μm
FOV_x	9.570 mm	9.583 mm
FOV_y	7.121 mm	7.177 mm
Mean error, $\bar{\epsilon}$	16.19 μm	16.88 μm
Error range, ϵ	15.92-17.50 μm	16.51-18.66 μm
Std. deviation, *s.d.*	0.25 μm	0.34 μm
Distortion %, D	0.68 %	0.84 %

Table D.1: Calibration data extracted from NI Vision Builder based on Figure D.4 for TDIM 1. The data obtained for TDIM 2 is also specified.

Working Principles of Laser used for IPI

E

The illumination source for IPI has three requirements it must fulfil.

- The intensity of the scattered light must be high enough to make sure the images of the particles can be recorded on the camera sensor, while still being above the optical noise level.
- The light pulse must have a duration which makes sure that the particles will not move considerably during the exposure of the light pulse.
- The measurement plan must be well defined in both location and dimensions.

The light sheet is formed through optics and produced by two pulsating beams from a double cavity Q-switched Nd:YAG laser, which is a solid state laser. It is applicable for air flows and high speed flows where high energy is needed (e.g. 400 mJ), and in water flows where lower energy is needed (e.g. 15 mJ). The Q-switched pulses include the advantage of short duration which is preferred when a freeze of moving particles is desired. The two cavities bring an advantage by being able to select the widest possible range of time between the pulses. The cavities also results in that the illumination energy budget will not change no matter the time between the pulses. [Dantec Dynamics, 2000a,pp. 4.31-4.33]

The illumination is only required when the camera is recording the image, which is why pulsed lasers are preferable since they use the available energy in short pulses of constant high light intensity. [Dantec Dynamics, 2000a,p. 4.34]

E.1 Cavity

Inside a mirrored elliptical cavity is a flash lamp and a YAG (yttrium-aluminum-garnet) crystal. The internal mirror maximises the energy transfer from the flash lamp to the crystal, whereof the heat generated for each pulse of the flash lamp is removed by cooling water. Figure E.1 shows an example of a flash lamp exiting the cavity for 250 μs at a frequency of 10 Hz. [Dantec Dynamics, 2000a,p. 4.34]

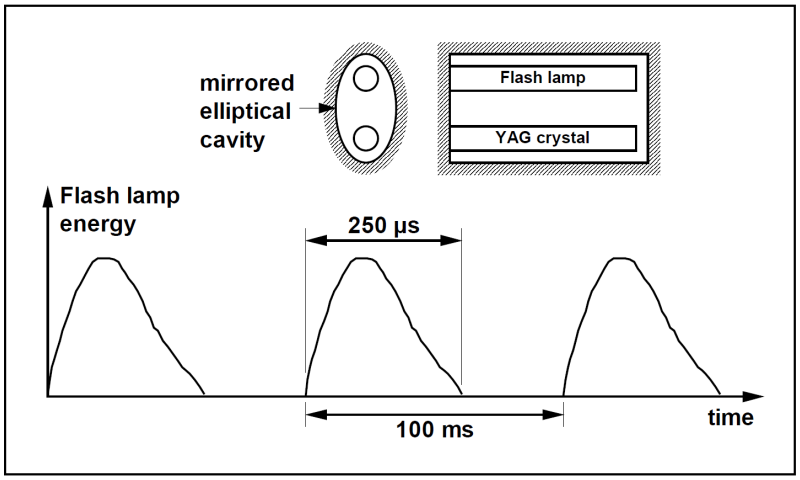

Figure E.1: Cavity and flash principle for a Nd:YAG laser. [Dantec Dynamics, 2000a,p. 4.34]

E.2 Q-switch

The laser energy is not emitted for the entire duration of the exciting flash lamp, since the cavity is kept close for most of that time period and only allowed open for a brief time of that period. This way a high energy pulse is released. The open and close mechanism is called a Q-switch (Quality). The energy is between 10-400 mJ per pulse while the duration per pulse is approximately 5-10 ns. A Q-switch is opened 150-200 μs after the flash lamp has been turned on, this is due to the natural dissipation rate of the cavity, see Figure E.2. [Dantec Dynamics, 2000a,pp. 4.34-4.35]

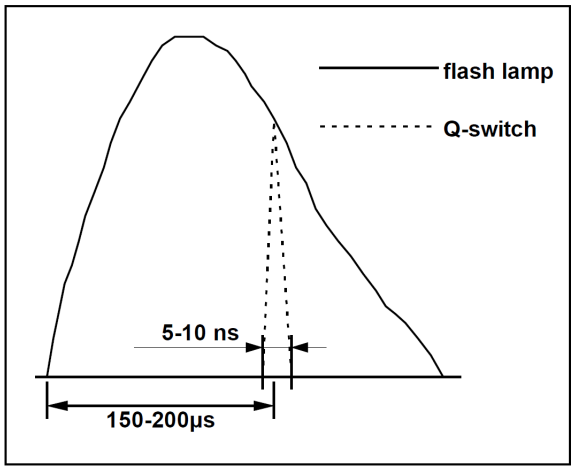

Figure E.2: Delayed Q-switch relative to the flash lamp. [Dantec Dynamics, 2000a,p. 4.35]

E.3 Double-cavity Laser

With two lasing cavities the time interval between pulses can be selected more freely while the beam energy will remain the same. Figure E.3 shows the structure of a double cavity-laser. The extra optics combines the beam path from the two cavities which both have a wavelength of 1064 nm. The beams are combined and led into a Harmonic generator which divides the wavelength into 532 nm of vertical polarised laser pulses [New Wave

Research, 1998]. For that reason the Q-switched YAG laser is also frequency doubled since the light's frequency is doubled. A Harmonic separator is applied to dump the remaining infrared beam from the Harmonic generator. [Dantec Dynamics, 2000a,pp. 4.36-4.37] It consists of dichroic mirrors [New Wave Research, 1998].

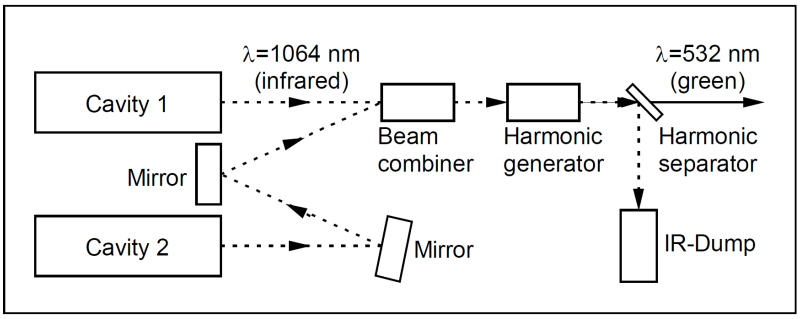

Figure E.3: Structure of a double-cavity laser. [Dantec Dynamics, 2000a,p. 4.36]

E.4 Synchronisation

Control signals for the Nd:YAG laser are generated from the FlowManager software. The synchronisation unit in the FlowMap Processor has four control signals implemented as shown in Figure E.4. One for each flash lamp and one for each Q-switch.

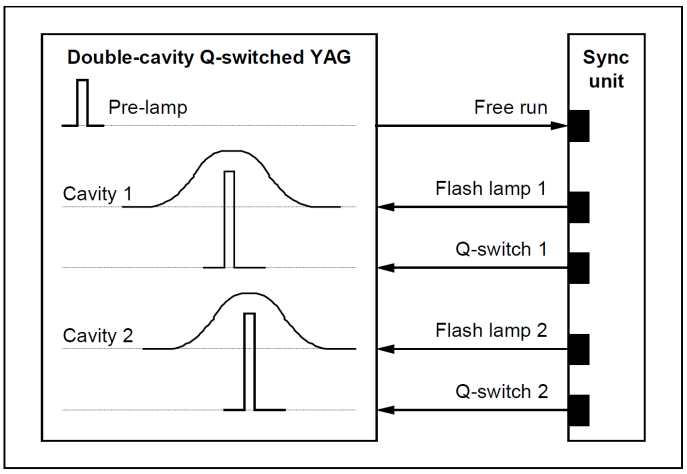

Figure E.4: Control signals for synchronisation of the Nd:YAG laser. [Dantec Dynamics, 2000a,p. 4.38]

E.5 Data for Nd:YAG Laser

Table E.1 shows the defaults and possible settings for the used Gemini PIV Nd:YAG laser system given from the FlowMap Particle Sizer software.

Warm-up Flashlamp periods		
Warm-up Flashlamp periods	10	F-periods
Warm-up Flashlamp and Q-switch periods	5	FQ-periods
Pulsed Laser		
Wavelength	532	nm
Pulse energy	120	mJ
Pulse width	10.0	ns
Max. number of pulses	2	-
Timing		
Repetition rate	8.0 to 21.0	Hz
Pulse interval	1.0 to 100000.0	μs
Max. trigger window	5000.0	μs
Flashlamp 1 - Q-switch delay	190.0	μs
Flashlamp 2 - Q-switch delay	190.0	μs
Q-switch 1 activation delay	0.180	μs
Q-switch 2 activation delay	0.180	μs
Duration of Flashlamp and Q-switch signals	10.0	μs

Table E.1: Nd:YAG laser settings given from the FlowMap Particle Sizer software.

According to Dantec Dynamics [Andersen, 2014]: "*The Gemini PIV Nd:YAG laser is polarised vertically according to the orientation of the laser. The laser sheet can be rotated but will not affect the polarisation, meaning that the polarisation according to the laser sheet can be customised.*" Based on this quote, the polarisation of the laser sheet in Figure 3.6 can be considered as being parallel to the laser sheet.

Some of the settings in Table E.1 are illustrated in Figure E.5. The Warm-up Flashlamp period is not indicated along with the Q-switch activation delay or the duration of Flash lamp and Q-switch signals.

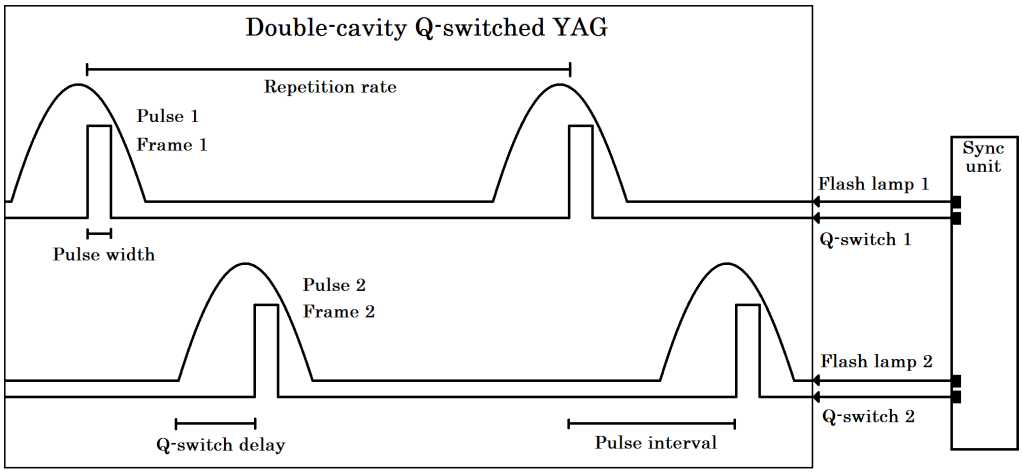

Figure E.5: Illustration of Nd:YAG laser data from Table E.1.

E.6 Light Sheet Thickness Adjustment

The 80×63 light sheet thickness adjuster can vary the thickness of the laser beam between 0.6-2.6 mm, but it depends on the location of the illuminated area as seen in Figure E.6. The location of the waist is changed in the same manner as a camera lens is focused. [Dantec Dynamics, 2000b]

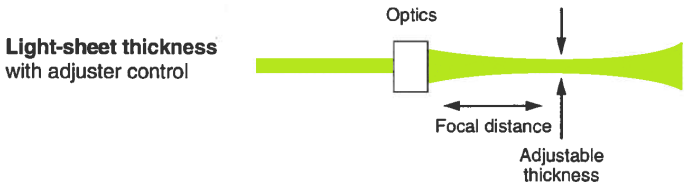

Figure E.6: Light sheet with adjuster control. [Dantec Dynamics, 2000b] - modified

In order to obtain the waist of the laser beam the Nd:YAG laser must be located at its focal distance away from the illuminated area. Figure E.7 shows the relation between the distance from the laser and the resulting light sheet thickness for the 80×63 adjuster. It should be noticed that the laser used in Figure E.7 for the applied adjuster does not correspond to the laser used in the experimental setup. Nevertheless the figure can be used as a starting point.

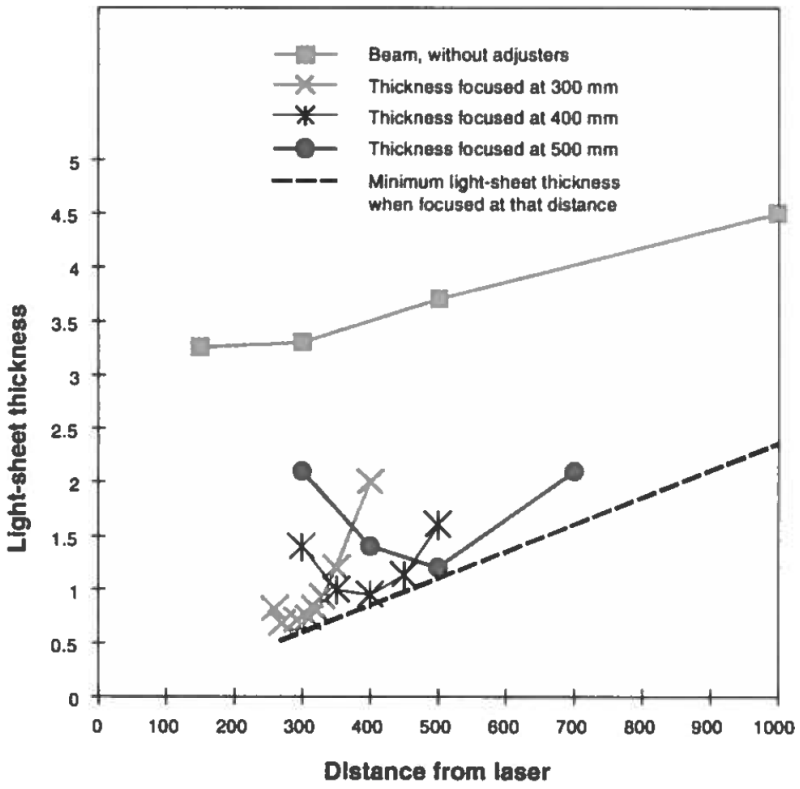

Figure E.7: Light sheet thickness by changing the focus range with the 80×63 adjuster on a 50 mJ laser 38A5266 New Wave MiniLase III PIV at 15 Hz. [Dantec Dynamics, 2000b]

Required Sample Size for IPI & TDIM

F

The number of images to give an accurate result of the bubble size distribution is to be determined. The estimation of the required sample size for both Interferometric Particle Imaging (IPI) and Telecentric Direct Image Method (TDIM) is based on the 2000 images utilised for each method for their results in Chapter 3 in Section 3.5 and Chapter 4 in Section 4.4. In addition, the continuous sampling of the diameters for each method is investigated to evaluate if any irregularities have been present during the sampling period.

F.1 Sample Size Processing

To estimate a minimum of validated bubbles to give a statistic good estimate of the bubble distribution, the mean value and variation of the distribution should approach a certain steady level as the sample size increases. The standard deviation, which is the square root of the variance, is used instead since the unit is identical to the mean diameter.

The mean bubble diameter, $\bar{d}$, of the sample is found by Equation F.1 and the standard deviation, $s.d.$, is found by Equation F.2.

$$\bar{d} = \frac{1}{n}\sum_{i=1}^{n}(d_i) \quad [\mu\text{m}] \tag{F.1}$$

$$s.d. = \left(\frac{1}{n-1}\sum_{i=1}^{n}(d_i - \bar{d})^2\right)^{0.5} \quad [\mu\text{m}] \tag{F.2}$$

Where:
n is the sample number of bubble diameters $[-]$
d_i is the individual bubble diameter $[\mu\text{m}]$

To make sure the mean value of the sample is close to the true mean, μ, the confidence interval, δ, is also considered. For large samples, $n \geq 30$, the confidence interval in Equation F.3 and Equation F.4 can be used even when normality of the data is not applicable. [Walpole et al., 2007,p. 280]

$$\bar{d} - \delta \leq \mu \leq \bar{d} + \delta \quad [\mu\text{m}] \tag{F.3}$$

(F.4) $$\delta = z_{\alpha/2}\frac{s.d.}{\sqrt{n}} \quad [\mu m]$$

Where:
μ is the true mean value [μm]
δ is the confidence interval [μm]
$z_{\alpha/2} = 1.96$ for $\alpha = 0.95$ [−]

F.2 Required Sample Size for IPI

One sample consists of an image pair of two frames, B1 and B2. A bubble is only added to the sample if it is found valid in both frames. Thereby the sample size depends on the amount of valid bubbles detected in each performed sample.

Figure F.1 shows the trends of $\bar{d}$, $s.d.$ and δ as function of the sample size. The final mean diameter and standard deviation are also marked with a line at the y-axes. The confidence interval goes towards 3.843 as the sample size increases.

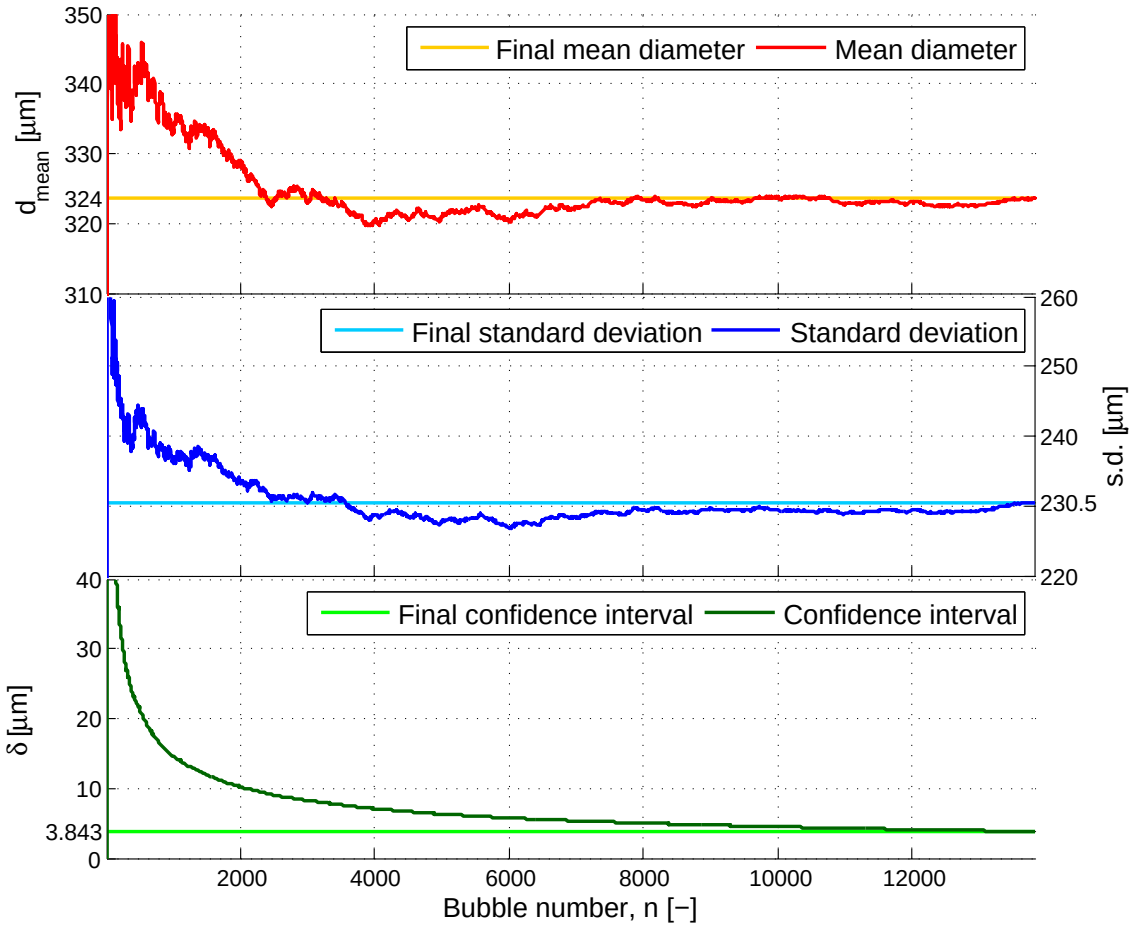

Figure F.1: IPI measurement. Top: mean diameter as function of the sample size. Center: standard deviation as function of the sample size. Bottom: Confidence interval.

Both $\bar{d}$ and $s.d.$ reach a steady value after approximately 3000 bubbles close to each of

their final value. 323 μm for the mean bubble diameter and 230.5 μm for the standard deviation. At a sample size of 3000 bubbles, the confidence interval has reached 8.25 μm, which is found acceptable small. The image sample consists of 2000 images for which 13,820 bubbles are detected. This gives an average of 6.91 bubbles per image. Hereof it can be estimated that for valid bubble detection 434 image samples are required for IPI sampling.

F.2.1 Measurement Stability for IPI

Since the sampling of the 2000 images takes 33m:19s the conditions affecting the bubble diameter can change. It can be the temperature, the pressure applied by the compressed air supplier, a leakage in the air hoses or something blocking a part of the cannula.

Figure F.4 shows the valid bubbles in the order they are sampled, where each measured diameter is marked. The continuous mean for every 100 bubble is marked together with the total mean. The pattern tendency of the measurements in the figure does not seem to change over the sampling time. Thereby the conditions during the experiments are assumed to be steady and not considered to affect the bubble distribution and the reliability of Figure F.1.

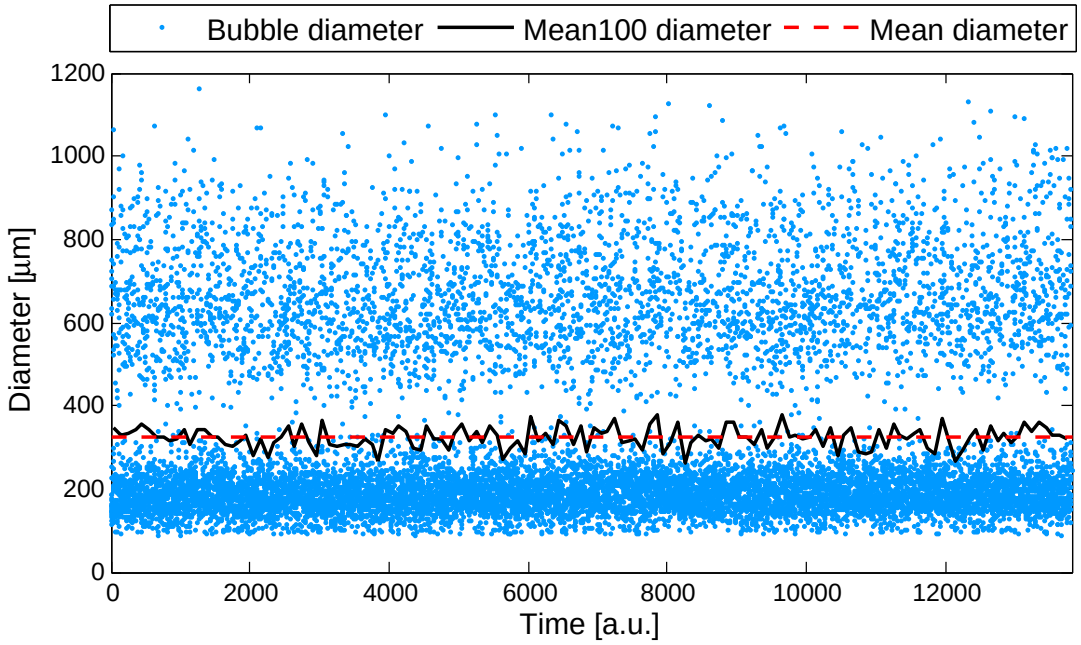

Figure F.2: IPI measurements. Continuous diameter sampling for IPI, showing each single sample diameter, a mean for every 100 sample and a total mean diameter.

F.3 Required Sample Size for TDIM

The same analysis is applied to the 2000 images of TDIM 1 with the result shown in Figure F.3. In this case the confidence interval goes towards 1.203 as the sample size increases.

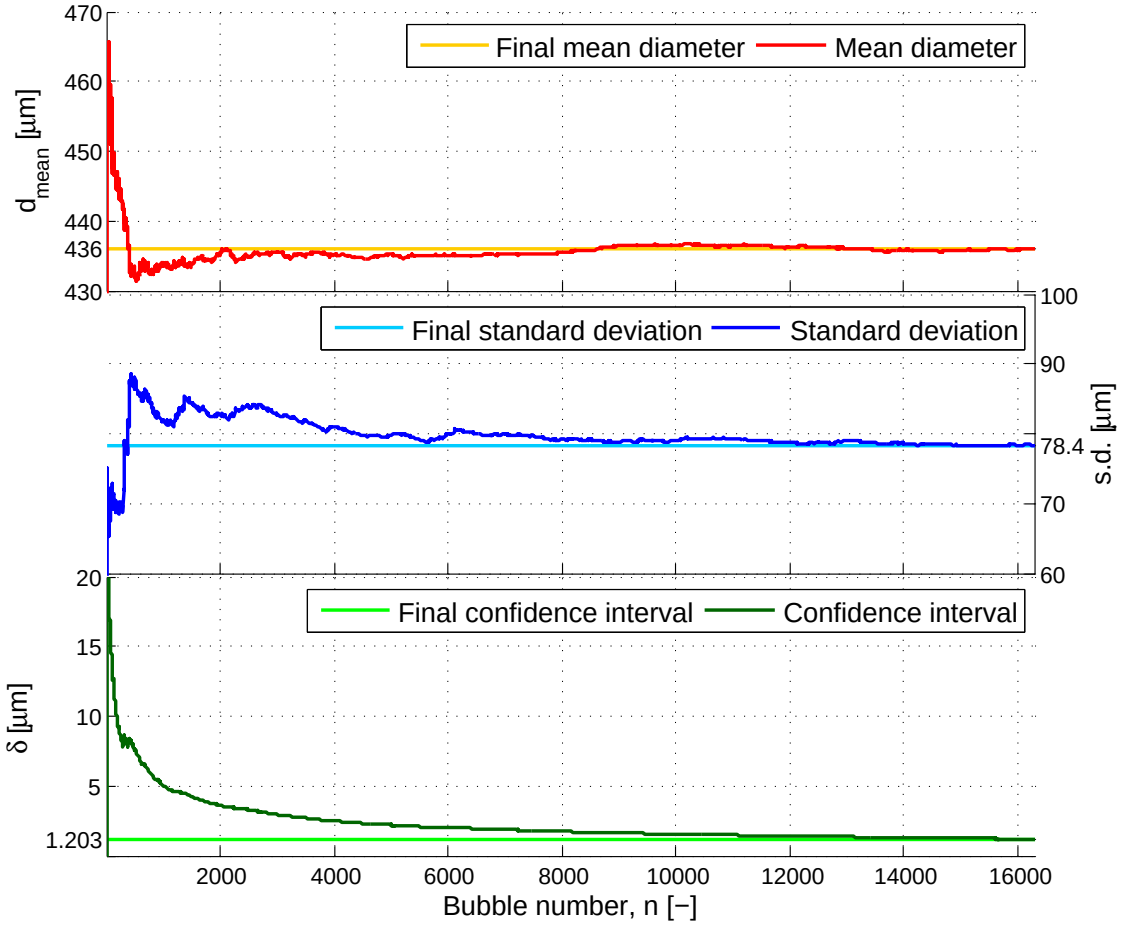

Figure F.3: TDIM measurements. Top: mean diameter as function of the sample size. Center: standard deviation as function of the sample size. Bottom: Confidence interval.

$\bar{d}$ and $s.d.$ reach a steady value after 4000 bubbles, with a confidence interval of 2.51 μm. The mean bubble diameter becomes 436 μm while the standard deviation is 78.4 μm. The image sample consists of 2000 images for which 16,297 detected and validated bubbles, which leads to an average of 8.15 bubbles per image. Meaning that for TDIM 491 image samples are required before reaching a steady value.

F.3.1 Measurement Stability for TDIM

The sampling time for the 2000 images for TDIM takes 8m:20s. The continuous sampling of bubbles is shown in Figure F.4 where every 100 bubbles is marked along with the total mean. There does not seem to appear any irregularities such a sudden deviation for the 100 mean diameters relative to the final mean diameter. Thereof the conditions during the sampling of data is considered as stable and has not effect on the bubble distribution or reliability in Figure F.3.

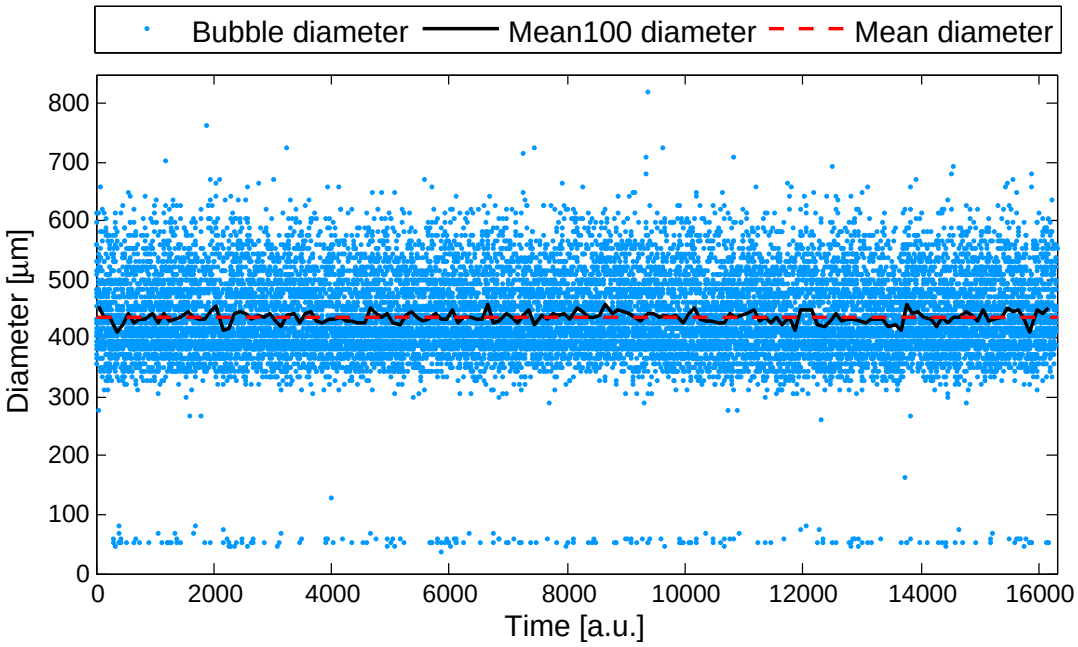

Figure F.4: Continuous diameter sampling for TDIM, showing each single sample diameter, a mean for every 100 sample and a total mean diameter.

TDIM Principles & Equipment G

By combining a telecentric lens and a telecentric bright field transmitted lighting source it is possible to obtain [Hornberg, 2006,p. 180]:

- high homogeneous contrast illumination of 3D objects (transparent to opaque)
- sharp edges from shiny cylindrical or spherical objects
- great accuracy and reliability
- good suppression of extraneous light

These benefits are desired in order to obtain the best possible estimation of the bubble size distribution. The following will review the concepts of telecentric imaging and the technical specifications of the equipment utilised in the setup described in Appendix B.

G.1 Telecentricity

In a conventional imaging system the magnification of an object will change as an object is moved relative to the camera. Perspective will be present by making the object look larger closer to the camera and smaller further away, see Figure G.1a. When using a telecentric imaging system the lens will correct for the perspective making the object being experienced as the same size independent of the location away from the lens within a specific FOV. An illustration of the principle is shown in Figure G.1b. The illustration in Figure G.1b is a result of collimated and parallel principal rays to the optical axis in the image and object space. Figure G.1b also shows a disadvantageous of using a telecentric lens. The front of the lens indicated by the Telecentric Region must be larger than the object placed in front of it. [Edmund Optics, 2014b]

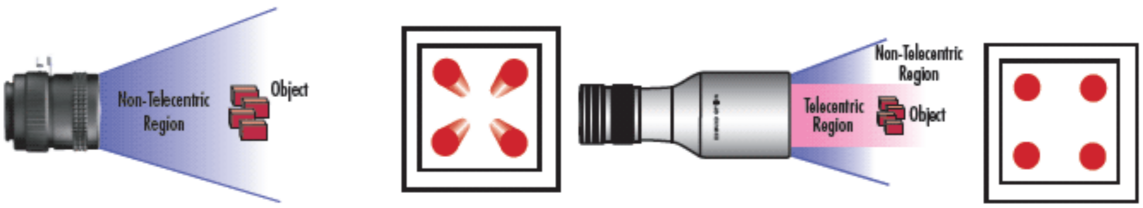

(a) Fixed focal length lens. (b) Telecentric lens.

Figure G.1: Visual comparison of the principle between a fixed focal length lens and a telecentric lens, showing how a telecentric lens virtually eliminates perspective angle error with the object not appearing as tilted. [Edmund Optics, 2014b]

Regarding the depth of field (DOF) then an object will still appear blurring further away from the focal plane (FP) but the object will blur symmetrically, which can be an advantages if wished to determine the location of the object in the Z-direction away from the FP. [Edmund Optics, 2014b]

G.2 Telecentric Lens

A conventional lens is shown in Figure G.2a. The aperture stop limits the amount of light which passes through the lens and changes the overall brightness of the image. Three rays are visible which go from any point on the object through the lens and then to the image. The ray which passes through the centre of the aperture stop is known as the principal ray. The remaining two rays is called marginal rays and coincide with the edges of the aperture and represent the outside bundle of light rays to the optical system. The aperture stop is located within the lens assembly making the images consist of converging light rays.

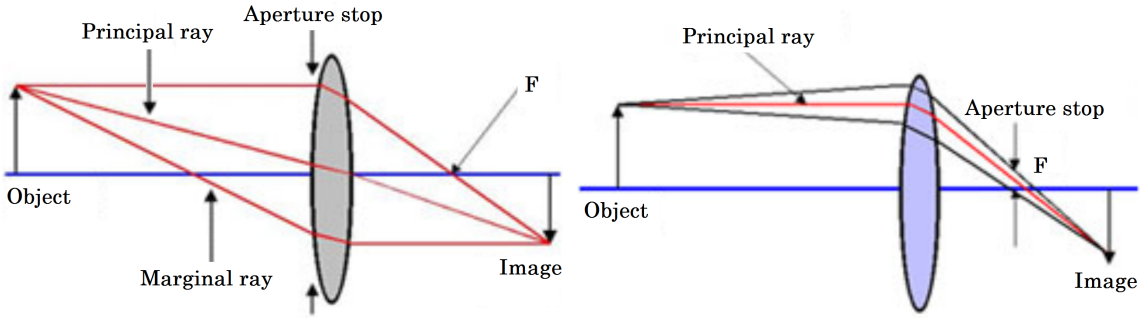

(a) Conventional lens. (b) Object space telecentric lens.

Figure G.2: A comparison between a conventional and telecentric lens. [Petrozzo and Singer, 2001] - modified

It is unlike a telecentric lens where the aperture stop is located at the focal point of the lens, see Figure G.2b. The light rays which travels through the aperture stop will only be those parallel to the optical axis, hence the principal ray. This is only valid for objects within the telecentric depth. [Petrozzo and Singer, 2001,pp. 5-6]

The telecentric effect in Figure G.1b is obtained by utilising the Edmund compact telecentric lens #63-729. The technical specifications are given in Table G.1.

Edmund Techspec - Compact telecentric lens #63-729	
Primary magnification	0.5×
Aperture, fixed f/#	f/9.3
FOV_x at sensor size of 1/3"	9.6 mm
Working distance	110 ±1 mm
Telecentric depth at maximum sensor format of 1/3"	±1.9 mm
Telecentricity	<0.2°
Distortion (pincushion)	<0.2 %

Table G.1: Technical data for the compact telecentric lens #63-729. [Edmund Optics, 2014a]

The *primary magnification* is the ratio between the sizes of the image to the size of the object. By having a primary magnification of 0.5× the lens will reduce the size of the object by a factor of 2 onto the image plan. The *aperture* specifies the size of the bundle of light rays which reaches the image plan. The FOV_x is the maximum size of the object which the lens can image, and for a telecentric lens it cannot exceed the front surface of the lens. The *working distance* is fixed on a telecentric lens and marks the distance from the front of the lens housing to the object. The *telecentric depth* indicates the distance before and after an object which remains in focus and has a constant magnification. The object which is desired to measure must stay entirely within this range. *Telecentricity* is the angular deviation affecting the principal ray in comparison to a ray which is parallel to the optical axis. The lower value the more accurate image is obtained. *Distortion* is the absolute deviation and is a function of the height of the image. [Petrozzo and Singer, 2001,pp. 6-7]

G.3 Light

Telecentric lighting is beneficial to use in conjunction with a telecentric lens in a parallel mounting. Figure G.3 shows the effect of estimating the diameter of a shiny cylinder by using either a conventional diffuse lightning component or telecentric lighting. By applying diffuse lighting the large lighting aperture in case (a) results in undefinable brightness transition. In case (b) the small lighting aperture causes sharp edges. A comparison of case (a) and (b) is shown in Figure G.3 under subimage (c). [Hornberg, 2006,pp. 180-181]

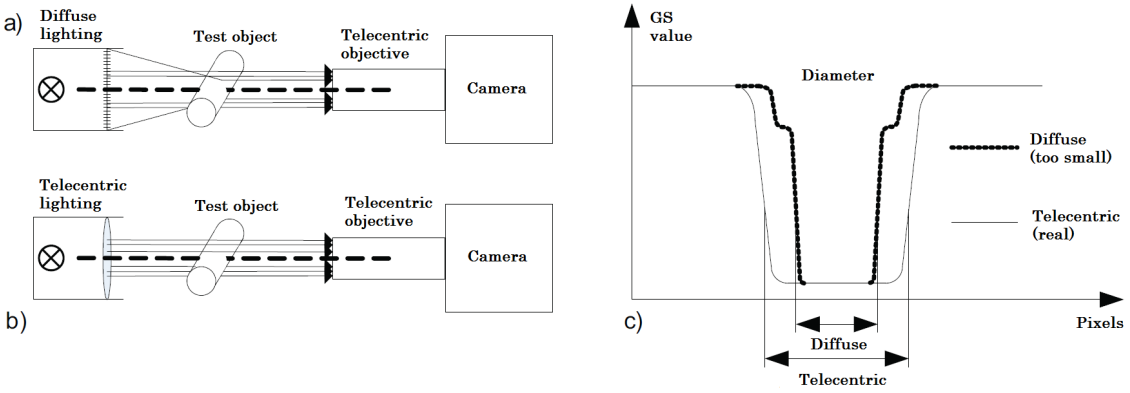

Figure G.3: The effect of using either diffuse or telecentric lighting in conjunction with a telecentric lens. [Hornberg, 2006,p. 181]

A telecentric light source will be the best choice for a light source but has not been available. In its place, a white 10 W LED lamp is applied to the setup, see Figure G.4. It is modified in the front with a plate in which a rectangular hole is made which is slightly larger than the FOV. The lamp has a scattering angle of 120° for which most of the scattered light will be blocked by the plate, and the more directed light will reach through the hole to the telecentric lens.

Figure G.4: 10 W white LED lamp. [SILVAN, 2014]

G.4 Camera

The utilised camera in conjunction with the prior mentioned equipment is a Basler acA1300-30um compact area scan camera. Table G.2 shows the technical data for the camera.

Basler ace acA1300-30um, monochrome	
Resolution	1296 × 996 pixels
Sensor	Sony ICX445
Sensor size	1/3"
Sensor technology	CCD
Pixel size	3.75 × 3.75 (μm)
fps at full resolution	30 Hz
Shutter	Global
Pixel bit depth	12 bits
Interface	3.0 USB

Table G.2: Technical data for the Basler ace acA1300-30um area scan camera. [Basler, 2014a]

The following graph in Figure G.5 shows the spectral response for sensor in the Basler ace acA1300-30um monochrome camera. The spectral response tends to peak in the green colour spectrum around 600 nm and consequently be the ideal colour of the telecentric light in Section G.3.

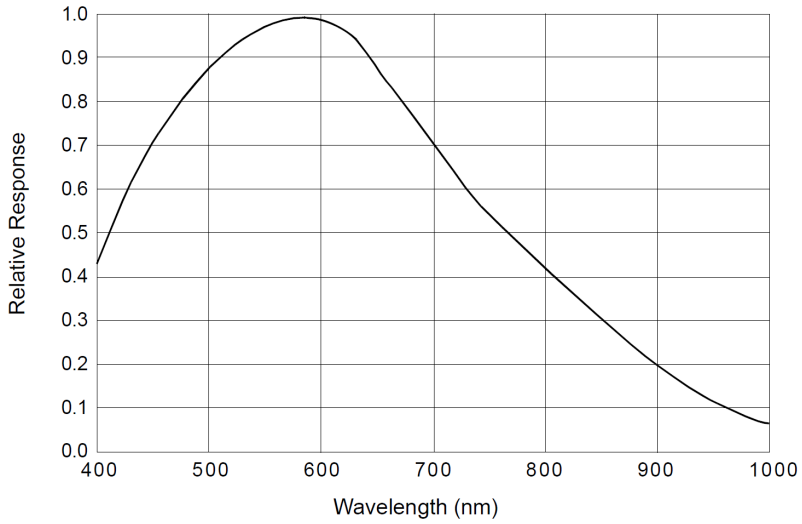

Figure G.5: Spectral reponse of the Sony ICX445 sensor. [Basler, 2014a]

CD Content H

The following are to be found on the attached CD:

- Digital copy of the report
- FlowMap Particle Sizer - Installation and User's Guide
- Digital copy of the paper *Bubble Detection using Digital Image Processing* + Appendix Report.
- TDIM:
  - Pre-processing
    - 12 original images
    - 12 pre-processed images
    - MATLAB script
    - 1 average background image
    - 1 average noise image
  - NI Vision, Image Processing
- Data Sheets
  - 4 PDF files concerning Basler camera
  - 2 PDF files concerning Edmund telecentric lens
  - 1 PDF file concerning Burkert pressure transmitter

Bibliography

Albrecht, H.E., Borys, M., Damaschke, N., Tropea, C., 2003. Laser Doppler and Phase Doppler Measurement Techniques. 1. ed., Springer. ISBN: 3-540-67838-7.

Andersen, M.T., 2014. Communication and provided material through mail correspondence - Sales Engineer at Dantec Dynamics.

AnMo Electronics, 2014. Dino-lite. Website. URL: `http://www.dino-lite.com`. last checked: 12.02.2014.

Basler, 2014a. ace data sheet. PDF. URL: `http://www.baslerweb.com/media/documents/BAS1401_ace_Brochure_Web.pdf`.

Basler, 2014b. Global shutter, rolling shutter - functionality and characteristics of two exposure methods (shutter variants). PDF. URL: `http://www.baslerweb.com/media/documents/BAS1401_White_Paper_Rolling-Shutter_en.pdf`.

Bürkert - Fluid Control Systems, 2003. Pressure Transmitter, Bürkert 8314. PDF - data sheet.

Celata, G.P., D'Annibale, F., Marco, P.D., Memoli, G., Tomiyama, A., 2006. Measurements of rising velocity of a small bubble in a stagnant fluid in one- and two-component systems. Experimental Thermal and Fluid Science 31 .

Chaira, T., Ray, A.K., 2010. Fuzzy Image Processing and Applications with Matlab. 1. ed. ISBN: 978-1-4398-0708-8.

Chen, X., Zhou, W., Cai, X., Su, M., Liu, H., 2013. In-line imaging measurements of particle size, velocity and concentration in a particulate two-pase flow. Particuology, Volume 13, pp. 106-113 .

Christensen, M.S., Thomassen, P.H., 2013. Bubble detection using digital image processing. Paper for CES conference in December 2013 , Student project - not published.

Coghe, A., Cossali, G.E., 2011. Quantitative optical techniques for dense sprays investigation: A survey. Optics and Lasers in Engineering, Volume 50 .

Damaschke, N., Nobach, H., Nonn, T.I., Semidetnov, N., Tropea, C., 2005. Multi-dimensional particle sizing techniques. Experiments in Fluids, Volume 39 .

Dantec Dynamics, 2000a. FlowManager software and Introduction to PIV Instrumentation - Software User's guide. 5. ed.

Dantec Dynamics, 2000b. Product information - 80X60 Mini Nd:YAG Light-sheet series. 1. ed.

Dantec Dynamics, 2003. FlowMap Particle Sizer - Installation & User's guide. 1. ed.

Dantec Dynamics, 2014a. Interferometric particle imaging (ipi). Website. URL: http://www.dantecdynamics.com/interferometic-particle-imaging. last checked: 06.02.2014.

Dantec Dynamics, 2014b. Phase doppler anemometry (pda). Website. URL: http://www.dantecdynamics.com/phase-doppler-anemometry. last checked: 12.05.2014.

Dantec Dynamics, 2014c. Shadow sizing. Website. URL: http://www.dantecdynamics.com/shadow-sizing. last checked: 13.05.2014.

Dehaeck, S., van Beeck, J.P., 2008. Multifrequency interferometric particle imaging for gas bubble sizing. Experimental Fluids 45 .

Edmund Optics, 2014a. Compact telecentric lens data sheet. PDF. URL: http://www.edmundoptics.com/.

Edmund Optics, 2014b. Edmund optics website. URL: http://www.edmundoptics.com/. last checked: 29.04.2014.

fluidimaging.com, 2014. Color versus black & white cameras. PDF.

h2physics, 2014. Young's double slit experiment. Website. URL: http://www.h2physics.org/?cat=48. last checked: 24.04.2014.

Hansen, R., 2009. Computational and Experimental Study of Bubble Size and Bubble Columns. Ph.D. thesis.

Hornberg, A., 2006. Handbook of Machine Vision. 1. ed. ISBN: 3-527-40584-7.

Jewett, J.W., Serway, R.A., 2008. Physics - for Scientists and Engineers with Modern Physics. 7. ed., Cengage Learning. ISBN: 0-495-11240-2.

Kolev, N.I., 2011. Multiphase Flow Dynamics 2 - Mechanical Interactions. 4. ed., Springer. ISBN: 978-3-642-20597-2.

König, G., Anders, K., Frohn, A., 1986. A new light-scattering technique to measure the diameter of periodically generated moving droplets. J. Aerosol Science, Vol. 17, No. 2. .

Maeda, M., Kawaguchi, T., Hishida, K., 2000a. Novel interferometric measurement of size and velocity distributions of spherical particles in fluid flows. Measurement Science Technology 11 .

Maeda, M., Kawaguchi, T., Kamiya, Y., Niwa, Y., 2000b. Bubble sizing by interferometric laser imaging. International symposium on application of laser techniques to fluid mechanics 10 .

Massoud, M., 2005. Engineering Thermofluids - Thermodynamics, Fluid Mechanics, and Heat Transfer. 1. ed., Springer. ISBN: 978-3-540-22292-7.

Michaelides, E.E., 2003. Hydrodynamic force and heat/mass transfer from particles, bubbles, and drops - the freeman scholar lecture. Journal of Fluids Engineering 125 .

Michaelides, E.E., 2006. Particles, Bubbles & Drops - Their Motion, Heat and Mass Transfer. 1. ed., World Scientific Publishing Co. Pte. Ltd. ISBN: 981-256-647-3.

Mischler, W., 2010. Entwicklung eines Experiments Zur Messung von Blasendichten und blaseninduziertem Gasaustausch. Thesis.

Mischler, W., Rocholz, R., Jähne, B., 2010. Experimental setup for the investigation of bubble mediated gas exchange. Gas Transfer at Water Surfaces .

Mortensen, H.H., 2013. Personal communication and provided material from Tetra Pak Scanima.

Munson, B.R., Young, D.F., Okiishi, T.H., Huebsch, W.W., 2012. Fundamental of Fluid Mechanics. 6. ed., Wiley. ISBN: 978-81-265-2392-4.

National Instruments, 2012. NI USB-6215 DAQ module - data sheet. `http:/www.ni.com/`.

New Wave Research, 1998. Gemini PIV and Solo PIV - Nd:YAG Laser Systems. Data Sheet.

Petrozzo, R.A., Singer, S.W., 2001. Telecentric lenses - simplify non contact metrology. PDF. URL: `http://www.schneideroptics.com/`. last checked: 1.05.2014.

Qieni, L., Wenhu, J., Tong, L., Xiang, W., Yimo, Z., 2013. High-accuracy particle sizing by interferometric particle imaging. Optic Communications 312 .

Semidetnov, N., Tropea, C., 2003. Conversion relationships for multidimensional particle sizing techniques. Measurement Science and Technology 15 .

Shiliang, P., 2005. Développement de méthodes interféromeétriques pour la caractérisation des champs de particules. Ph.D. thesis.

SILVAN, 2014. Gripo led vaeglampe - 10w ip65. Website. URL: `http://eshop.silvan.dk/vare/gripo-led-vaeglampe`. last checked: 15.05.2014.

Tayali, N.E., Bates, C.J., 1990. Particle sizing techniques in multiphase flows - a review. Flow Meas. Instrum., Volume 1, pp. 77-105 .

Walpole, R., Myers, R., Myers, S., Ye, K., 2007. Probability & Statistics for Engineers & Scientists. 8. ed., Person Prentice Hall. ISBN: 0-13-204767-5.